

---

**Searching for diboson resonances in the  
all-hadronic final state  
and  
a Lorentz invariance based deep neural network for  
W-tagging**

---

Dissertation  
zur  
Erlangung der naturwissenschaftlichen Doktorwürde  
(Dr. sc. nat.)

vorgelegt der  
Mathematisch-naturwissenschaftlichen Fakultät  
der  
Universität Zürich

von  
Thea Klaeboe Arrestad  
aus  
Norwegen

Promotionskommission:  
Prof. Dr. Benjamin Kilminster  
Prof. Dr. Florencia Canelli  
Prof. Dr. Jesse Thaler  
Dr. Andreas Hinzmann

Zürich 2018



## **Abstract**



## **Zusammenfassung**

Die vorliegende Doktorarbeit stellt blabla.....



---

# Contents

<b>1</b>	<b>The Standard Model and Beyond</b>	<b>2</b>
1.1	The Standard Model Lagrangian . . . . .	3
1.1.1	Particles and fields . . . . .	3
1.1.2	Electroweak theory . . . . .	3
1.1.3	The Higgs Mechanism . . . . .	3
1.1.4	Quantum Chromodynamics . . . . .	3
1.2	Beyond Standard Model Physics . . . . .	3
1.2.1	The hierarchy problem and the gravitational force . . . . .	3
1.2.2	Theories of New Physics . . . . .	3
1.2.3	Heavy Vector Triplet formalism . . . . .	3
1.3	Statistical methods: Confidence Limits . . . . .	3
<b>2</b>	<b>Statistical Methods</b>	<b>4</b>
2.1	Statistical methods: Confidence Limits . . . . .	5
<b>3</b>	<b>Experimental setup</b>	<b>6</b>
3.1	The Large Hadron Collider . . . . .	7
3.2	The CMS detector . . . . .	9
3.2.1	Coordinate system . . . . .	11
3.2.2	Tracking detectors . . . . .	11
3.2.3	Electromagnetic calorimeter . . . . .	12
3.2.4	Hadron calorimeter . . . . .	14
3.2.5	Muon chambers . . . . .	17
3.3	Trigger system: From collision to disk . . . . .	17
<b>4</b>	<b>Event reconstruction</b>	<b>19</b>
4.1	Track and primary vertex reconstruction . . . . .	20
4.2	The Particle Flow Algorithm . . . . .	21
4.2.1	Reconstruction of the Particle Flow inputs . . . . .	22
4.2.2	Particle Flow identification . . . . .	23
4.3	Pile-up removal . . . . .	24
4.3.1	Charged Hadron Subtraction . . . . .	25
4.3.2	Pile up per particle identification (PUPPI) . . . . .	25
4.4	Jet reconstruction . . . . .	26
4.4.1	Jet clustering . . . . .	26
4.4.2	PF jets in CMS . . . . .	29
4.4.3	Jet energy corrections . . . . .	29
4.5	Jet substructure reconstruction . . . . .	29
4.5.1	Grooming . . . . .	30

4.5.2	N-subjettiness . . . . .	32
4.5.3	Vector boson tagging . . . . .	33
4.6	Monte Carlo Event Generators . . . . .	35
<b>5</b>	<b>Diboson resonance searches in CMS</b>	<b>37</b>
5.0.1	A small bump . . . . .	39
5.0.2	Analysis strategy . . . . .	40
5.0.3	Data and simulated samples . . . . .	40
5.0.4	Event selection . . . . .	41
5.0.5	Background modeling . . . . .	54
5.0.6	Signal modeling . . . . .	57
5.0.7	Systematic uncertainties . . . . .	57
5.0.8	Results . . . . .	58
5.0.9	Towards robust boosted jet tagging . . . . .	64
5.0.10	Analysis strategy . . . . .	65
5.0.11	Data and simulated samples . . . . .	66
5.0.12	Event selection . . . . .	66
5.0.13	Developing a new W-tagger . . . . .	69
5.0.14	Dedicated PUPPI+softdrop mass corrections . . . . .	70
5.0.15	W-tagging performance . . . . .	72
5.0.16	Validation in data . . . . .	74
5.1	Search III: A novel framework for multi-dimensional searches . . . . .	76
5.1.1	Small bumps and tribosons . . . . .	77
5.1.2	Analysis strategy . . . . .	77
5.1.3	Event selection . . . . .	77
5.1.4	A mass and $p_T$ decorrelated tagger . . . . .	77
5.1.5	The multidimensional fit . . . . .	77
<b>6</b>	<b>LoLa: A novel Machine Learning W-tagger for future analyses</b>	<b>78</b>
6.1	Machine Learning: The future of high-performance, low-latency taggers . . . . .	79
6.2	LoLa: A Lorentz Invariance Based Deep Neural Network for W-tagging . . . . .	79
6.2.1	Inputs . . . . .	79
6.2.2	The Combination Layer . . . . .	79
6.2.3	The Lorentz Layer . . . . .	79
6.3	Decorrelating from mass and $p_T$ . . . . .	79
6.4	Performance . . . . .	79
<b>7</b>	<b>Summary</b>	<b>80</b>
<b>A</b>	<b>Search I: Limits per mass category</b>	<b>81</b>
<b>Bibliography</b>		<b>86</b>

---

## Introduction

A short explanation of NP decaying to dibosons (Vprime, Gravition), jets in the boosted regime (substructure), the search strategy of 2015+2016 (1D) and 2017 (3D). Touch on triboson signatures to emphasise 3D

---

CHAPTER 1

---

The Standard Model and Beyond

## 1.1 The Standard Model Lagrangian

1.1.1 Particles and fields

1.1.2 Electroweak theory

1.1.3 The Higgs Mechanism

1.1.4 Quantum Chromodynamics

## 1.2 Beyond Standard Model Physics

1.2.1 The hierarchy problem and the gravitational force

1.2.2 Theories of New Physics

Warped extra dimensions

Compositeness

1.2.3 Heavy Vector Triplet formalism

## 1.3 Statistical methods: Confidence Limits

---

CHAPTER 2

---

Statistical Methods

## 2.1 Statistical methods: Confidence Limits

---

CHAPTER 3

---

Experimental setup

### 3.1 The Large Hadron Collider

In March 1984, the European Organization for Nuclear Research (CERN) and the European Committee for Future Accelerators (ECFA) held a workshop in Lausanne entitled "Large Hadron Collider in the LEP Tunnel". This is history's first written mention of the Large Hadron Collider (LHC) and the topic under discussion was exactly how and where to build a new type of high-energy collider, capable of bringing hadrons to collide rather than leptons. The LHC would be housed in a tunnel which, at the time, was under excavation to host the Large Electron-Positron Collider (LEP) designed to collide leptons with center-of-mass energies up to around 200 GeV. LEP was a circular collider with a circumference of 27 km and the tunnel hosting it was located roughly 100 meters underground on the border between France and Switzerland, at the outskirts of Geneva. The justification for building a machine like the LHC, was that once LEP got to maximum reach, a new and more powerful collider would be needed in its place in order to probe higher energies. While collisions of electrons with positrons provided exceptionally clean and precise measurements due to them being point particles, their lightness prevent them from being accelerated to higher energies. Collisions of hadrons, however, would allow for center-of-mass energies two orders of magnitude higher than that of LEP. Therefore, after running a while at two times the W mass (160 GeV) and reaching a maximum center-of-mass energy of 209 GeV, LEP was dismantled in 2000 in order to make room for the LHC.

The Large Hadron Collider started up in September 2008 and, while having the same 27-kilometer radius as the LEP collider, is capable of accelerating protons up to a center-of-mass energy of around 14 TeV, 70 times that of LEP. The accelerator consists of two oppositely going proton beams, isolated from each other and under ultrahigh vacuum, which are accelerated up to speeds close to that of the speed of light through radio frequency (RF) cavities, before being brought to collide at four different interaction points along the ring. These four collision points correspond to the location of the four LHC particle detectors; ATLAS, CMS, LHCb and ALICE. While ATLAS and CMS are general-purpose detectors built in order to study a large range of different physics processes, LHCb and ALICE are built for dedicated purposes; LHCb for b-physics processes and ALICE for heavy ion collision. A proton's journey from gas to one of the LHC collision points is as follows: First, hydrogen nuclei are extracted from a small tank of compressed hydrogen gas and stripped of their electrons. The remaining protons are then injected into the LINAC2, a linear accelerator responsible for increasing the proton energy to about 50 MeV through RF cavities that push charged particles forward by switching from positive to negative electric fields. LINAC2 additionally divides the constant stream of particles into equally spaced "bunches" by careful tuning of the frequency of the field switch. The accelerated protons are then injected into the Proton Synchrotron Booster (PSB), where their energy is increased thirty-fold more, to an energy of roughly 1.4 GeV. The two final acceleration stages before the protons reach the LHC ring are the Proton Synchrotron and Super Proton Synchrotron, eventually leaving the protons with a total energy of 450 GeV. The protons are now ready for the final stage of their travel and are injected into the two beam pipes of the LHC in oppositely going direction. They are injected in trains of 144 bunches each (with an order of  $10^{11}$  protons per bunch), where each bunch is roughly 7.5 meters apart (or 25 ns). There are some larger beam gaps present in each beam in order to give the beam dump and injection kickers sufficient time to reach full voltage, where the largest one, the beam abort gap, is roughly 3 ms or 900 m long. The ring is filled with proton bunches until these are equally distributed throughout the two rings, a process taking roughly 4 minutes. This is called a "fill". Here, the protons are accelerated to their maximum energy of 6.5 TeV, a process taking roughly 20 minutes, through eight

RF cavities. These RF cavities are also responsible of keeping the proton bunches tightly bunched, ensuring maximum luminosity at the four collision points. A complete sketch of the CERN accelerator complex is shown in Figure 3.1.

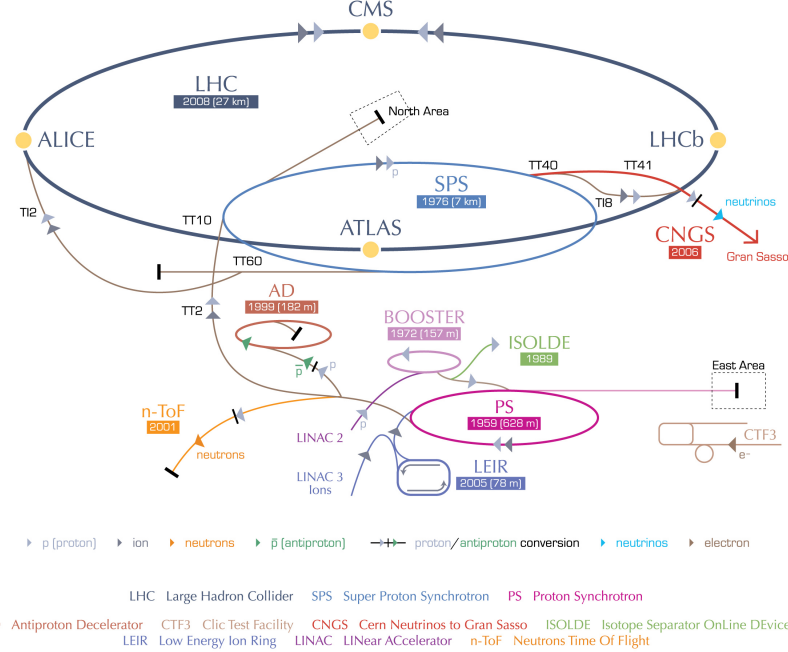


**Figure 3.1:** The Large Hadron Collider accelerator complex. The four collision points along the ring correspond to the location of the LHC particle detectors CMS, LHCb, ATLAS and ALICE [1].

After the beams have reached their maximum energy and are stably circulating in the LHC ring, they are brought to collide. The goal of such a collision, which occurs every 25 nano seconds, is that some of the protons will undergo an inelastic collision, allowing the quark/gluon constituents of each proton to interact with one another and produce new and interesting particles. The number of times such an interaction will take place inside a detector per area and time is quantified through the luminosity,  $\mathcal{L}$ , which is the proportionality factor between the number of observable events per second, and the cross section  $\sigma$  of the process you are interested in

$$\frac{dN_{events}}{dt} = \mathcal{L}\sigma. \quad (3.1)$$

The cross section is the probability that an event (like one which would produce new and interesting particles) will occur and is measured in barns, where 1 barn =  $10^{-28} \text{ m}^2$ . This proportionality factor should therefore be as high as possible. It depends only on parameters of the detector and can, in the case of LHC, be defined through the following accelerator quantities

$$\mathcal{L} = \frac{N_b^2 n_b f_{rev} \gamma_r}{4\pi\epsilon_n\beta_*} F, \quad (3.2)$$

Parameter	Units	Nominal	2015	2016	2017
Energy	[TeV]	7.0	6.5	6.5	6.5
Bunch spacing	[ns]	25	25	25	25
Bunch intensity	$\times 10^{11}$ [protons/bunch]	1.15	1.15	1.15	1.2-1.45
Bunches per train		144	144	96	144
Total number of bunches		2808	2244	2220	2556
$\beta^*$	[cm]	55	80	40	27/25
Peak luminosity	$\times 10^{34}$ [cm $^{-2}$ s $^{-1}$ ]	1.0	0.5	1.4	2.0
Integrated luminosity			4.2	39.7	50.2

**Table 3.1:** Some key LHC detector parameters achieved during the first years of 13 TeV data taking

where  $N_b$  is the number of particles per bunch,  $n_b$  is the number of bunches,  $f_{rev}$  is their revolution frequency,  $\gamma_r$  is the relativistic gamma factor,  $\epsilon_n$  is the transverse beam emittance (how confined the particles are in space and momentum),  $\beta^*$  is the beta function at the collision point (how narrow, or "squeezed", the beam is) and  $F$  is a reduction factor to account for a constellation where the beams do not collide heads-on but at slight crossing angles. From this, it becomes clear that the main goal of the LHC is to; maximize the number of particles ( $N_b, n_b$ ), their frequency ( $f_{rev}$ ) and their energy ( $\gamma_r$ ), while at the same time ensuring the protons are packed together as tightly as possible (lower  $\epsilon_n$  and  $\beta^*$ ). Using the nominal values of the LHC, the peak luminosity is roughly  $\mathcal{L} \sim 10^{34} \text{ cm}^{-2} \text{ s}^{-1}$ .

The peak luminosity of the LHC by the end of Run 2 in 2018 was grazing around  $2.0 \cdot 10^{34} \text{ cm}^{-2} \text{ s}^{-1}$ , corresponding to 2 times the nominal design luminosity.

To quantify the size and statistical power of a given LHC dataset, the integrated luminosity is used. This is the integral of the instantaneous luminosity over time and is defined as

$$\mathcal{L}_{int} = \int \mathcal{L} dt. \quad (3.3)$$

It is usually defined in units of inverse cross section, b $^{-1}$ .

Despite the LHC starting up in 2008, there would be another year before data taking began. In March 2010, the LHC saw its first collision with a center-of-mass energy of 7 TeV, and continued running at this energy collecting around 5 inverse femtobarns of data by the end of 2011. In 2012, the energy was increased to 8 TeV and the LHC continued running until a planned long shutdown scheduled to begin in February 2013, collecting a total of  $\sim 20 \text{ fb}^{-1}$  and discovering the Higgs boson. This marked the end of Run 1 and the beginning of a two-year maintenance project intended to prepare the LHC for running at a center-of-mass energy of 13 TeV; Run 2.

Run 2, and where this thesis begins, started in June 2015. With the accelerator now running at 90% of its nominal energy, and with a peak luminosity between 1-2 times the design luminosity, the LHC managed to collect an impressive  $\sim 160 \text{ fb}^{-1}$  at this energy until its planned shutdown at the end of 2018. Some key LHC accelerator parameters that were in use for the datasets analyzed in this thesis, are quoted in Table 3.1

## 3.2 The CMS detector

The Compact Muon Solenoid (CMS) detector is true to its name; with a diameter of 15 meters and a weight of 14000 tons, it is 60 % smaller but two times heavier than its general purpose counterpart, the ATLAS detector. Its large weight is due to the CMS housing the world's largest and most powerful solenoid: A superconducting niobium titanium coil

circulating 18500 Amps and capable of generating a magnetic field of 3.8 Tesla. Together with its corresponding iron return yoke, responsible for reflecting the escaping magnetic flux, it accounts for 90% of the total detector weight. The CMS detector is cylindrically symmetric and organized in the following way: closest to the beam pipe and at a radius of about 3 cm, the inner tracking system begins. It consists of an inner silicon pixel detector and an outer silicon strip tracker, stretching out to a radius of roughly 1.2 meters. Following the tracker are two calorimeter layers: the electromagnetic calorimeter (ECAL) consisting of lead tungstate scintillating crystals and responsible for measuring the energy of electromagnetically interacting particles, followed by the hermetic hadronic calorimeter (HCAL) measuring the energy of hadrons. Contrary to "standard" configurations for general purpose detectors, the CMS calorimeters are located inside the superconducting solenoid. This allows the detector to be rather compact, by reducing the necessary radius of the calorimeters, and additionally for the magnet to be strong enough (the magnetic field strength depends on the coil radius) to allow muon detectors to be located within the magnetic field so their momentum can be measured. The muon detectors are alternated with three layers of steel return yoke responsible for containing and reflecting the magnetic field and which only allows muons and weakly interacting particles to pass. A schematic overview of the CMS detector is shown in Figure 3.2. In the following, the different sub-detectors will be described in detail.

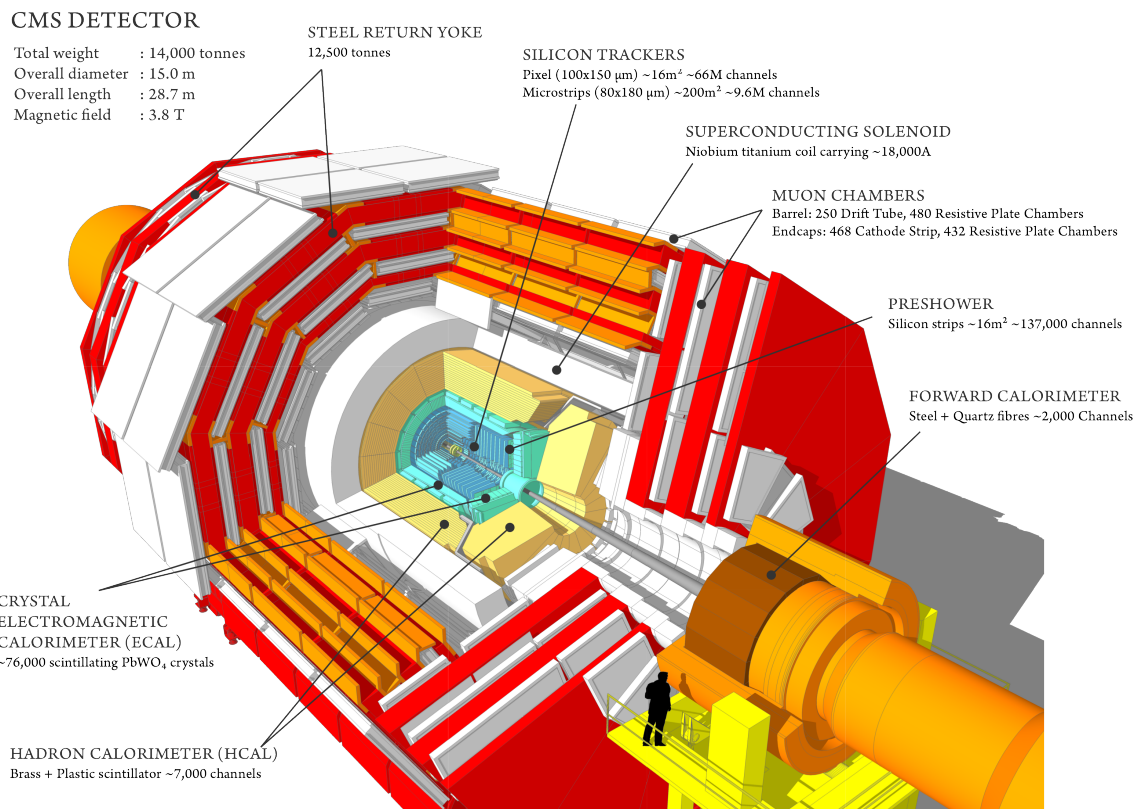


**Figure 3.2:** The CMS detector and its subsystems: The silicon tracker, electromagnetic and hadron calorimeters, the superconducting solenoid and the muon chambers inter-layered with the steel return yoke [2].

### 3.2.1 Coordinate system

To describe locations within the CMS detector, a Euclidian space coordinate system is used. Here, the positive z axis points along the beam pipe towards the west, the positive x axis points towards the center of the LHC ring, and the positive y axis upw towards the earths surface. Due to the cylindrical symmetry of the detector, polar coordinates are more convenient and most frequently encountered. In this scheme, the azimuthal angle  $\phi$  is measured in the xy-plane, where  $\phi = 0$  correspond to the positive x axis and  $\phi = \pi/2$  correspond to the positive y axis. The polar angle  $\theta$  is measured with respect to the z axis,  $\theta = 0$  aligning with the positive and  $\theta = \pi$  with the negative z axis. To define a particles angle with respect to the beam line, the pseudorapidity  $\eta = -\ln \tan(\theta/2)$  is preferred over  $\theta$ . This is due to the fact that particle production is approximately constant as a function of pseudorapidity and, more importantly, because differences in pseudorapidity are Lorentz invariant under boosts along the z-axis when assuming massless particles. To measure angular difference between particles in the detector, the variable  $R = \sqrt{\eta^2 + \phi^2}$  is used, again Lorentz invariant under longitudinal boosts. A summary of the CMS coordinate system together with some example values are shown in Figure 3.3.

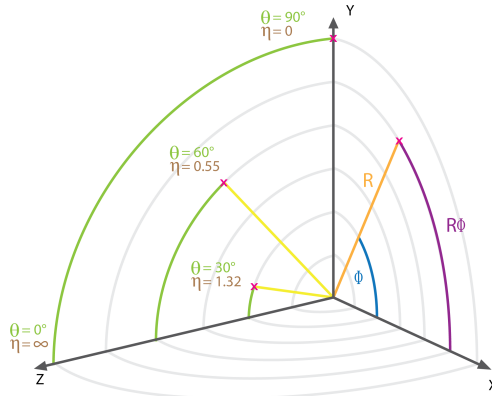


**Figure 3.3:** The CMS coordinate system [3]

### 3.2.2 Tracking detectors

The CMS tracker is responsible for accurately reconstructing the momentum of charged particles and consists of two sub-detectors. Closest to the interaction point, and where the particle intensity is the highest, the silicon pixel detector is located. Upgraded in 2017, from the so-called Phase-0 to the Phase-1 layout, it is structured in four cylindrical barrel layers at radii 2.9, 6.8, 10.9 and 16.0 cm (the barrel pixel) and three disks in each of the forward regions placed at a distance from the nominal interaction point of 29.1, 39.6 and 51.6 cm (the forward pixel). A sketch of the current Phase-I pixel detector compared to the Phase-0 detector is shown in Figure 3.4. The sensors located closest to the beam pipe are subject to hit intensities of  $\mathcal{O}(\text{MHz}/\text{mm}^2)$  which puts strict constraints on the maximum sensor size in order to minimize occupancy in the detector. The pixel sensors are  $100 \mu\text{m} \times 150 \mu\text{m}$  with a thickness of  $285 \mu\text{m}$ , and when counting both barrel and pixel sensors, sum up to a total of 79 million. The pixel sensors are mounted on detector modules with 16 read-out chips each, where the type of read-out chip depends on how close the module is to the beam pipe: the inner layer uses read-out chips with a rate capability of  $600 \text{ MHz/cm}^2$  while for the outer layers, read-out chips with a rate capability of up to  $200 \text{ MHz/cm}^2$  are sufficient.

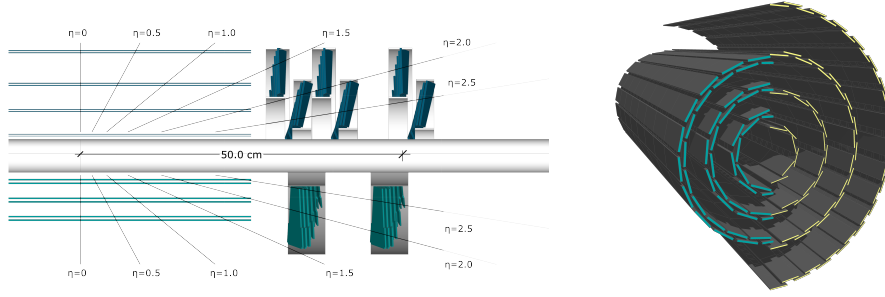


**Figure 3.4:** Left: The forward pixel detector layout before (bottom) and after (top) the Phase-I upgrade. Right: The barrel pixel detector before (left) and after (right) the Phase-I upgrade [4].

As the hit intensity reduces as you go further away from the beam pipe, the pixel sensors are replaced by silicon strip sensors, making up the second of the two tracker sub-systems, the silicon strip tracker. There are ten strip layers in total, stretching out to a radius of roughly 130 cm. These are divided into four sections: The inner barrel (TIB) with four strip layers, the two inner endcaps (TID) consisting of three disks each, the outer barrel (TOB) consisting of 6 cylindrical layers and the two endcaps (TEC) with 9 strip layers each. A schematic overview of the strip tracker layout is shown in Figure 3.5. The strips in the TIB and TID are 10 cm long, with a width of 80  $\mu\text{m}$  and a thickness of 320  $\mu\text{m}$ . The TOB and TEC sections consist of slightly larger strips of 25 cm x 180  $\mu\text{m}$  and a thickness of 500  $\mu\text{m}$ . The strip tracker has a total of 10 million detector strips and covers an area of  $\sim 200 \text{ m}^2$ . To prolong the silicon detector lifetime, the entire tracker (pixel and strip) is kept at a temperature of  $-20^\circ\text{C}$  through a liquid cooling system. The tracker has a coverage up to  $|\eta| < 2.6$  and a resolution of roughly  $\sigma/p_T \approx 1.5 \times 10^{-5} p_T \oplus 0.005$ .

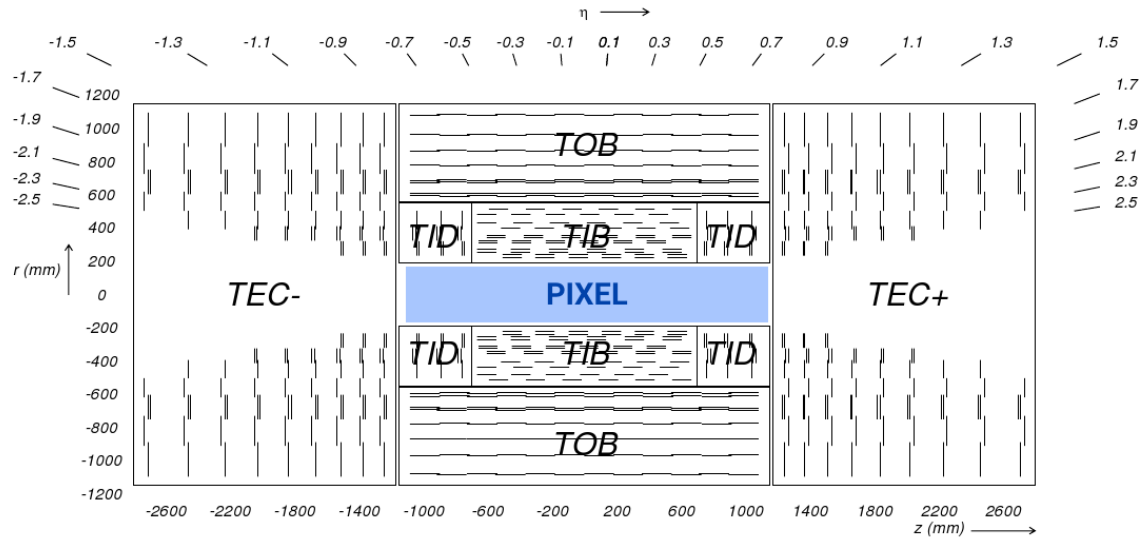


**Figure 3.5:** Schematic of the CMS silicon strip tracker and its four subsections: The inner barrel (TIB), inner endcaps (TID), the outer barrel (TOB) and the two endcaps (TEC) [5].

### 3.2.3 Electromagnetic calorimeter

Following the tracking detectors is the electromagnetic crystal calorimeter (ECAL). Consisting of 75 848 laterally segmented scintillating lead tungstate ( $\text{PbWO}_4$ ) crystals, it was designed

to have the highest possible photon energy and position resolution in order to resolve a Higgs boson decaying into two photons, the cleanest of the Higgs discovery channels. With a goal of a photon/electron energy resolution of 0.5% above 100 GeV, the choice of detector material for the ECAL has been its most crucial design feature. In order to withstand the high doses of radiation and the high magnetic field present within the detector, while at the same time generating well-defined signal responses within the 25 nanoseconds between particle collisions, an extremely dense and transparent material capable of producing fast and clean photon bursts when hit, is required. The choice eventually fell on metal-heavy lead tungstate crystals, each taking roughly two days to artificially grow (and a total of about ten years to grow all of them). With a density of  $\delta = 8.28 \text{ g/cm}^3$  (slightly higher than for stainless steel), the crystals are compact enough to yield excellent performance without taking up too much volume, allowing the ECAL to sit within the CMS superconducting solenoid. The homogeneous medium allows for a better energy resolution as it minimizes sampling fluctuation effects and it additionally contains enough oxygen in crystalline form to make it highly transparent to their entire scintillation emission spectrum. With an extremely short radiation length and small Moli  re radius ( $X_0 = 0.85 \text{ cm}$ ,

$$R_M = 2.19$$

cm), the required homogeneity, granularity and compactness is obtained while at the same time emitting 80% of generated light within the 25 ns timeframe required. The largest drawbacks with a lead tungstate detector is the low light yield (100  $\gamma$  per MeV), requiring dedicated avalanche photodiodes to increase the gain, as well as a light yield which strongly depends on the temperature. The detector response to an incident electron changes by  $3.8 \pm 0.4 \%$  per degree Celsius which requires the ECAL temperature to be kept stable around  $18.0(5)^\circ\text{C}$ , obtained through an intricate water cooling system. The ECAL is completely hermetic and sorted into a barrel part (EB), covering pseudorapidities up to  $|\eta| < 1.48$ , and two endcap parts (EE) extending the total coverage to  $|\eta| < 3.0$  in order to match the tracker coverage of  $|\eta| < 2.5$ . In order to improve the  $\gamma/\pi_0$  separation power, a pre-shower detector (ES) using lead absorbers and silicon sensors covers the forward region between  $1.65 < |\eta| < 2.6$ . The crystals in the barrel are organized into supermodules, each consisting of about 1700 crystals, while the endcap is divided into two half disks consisting of 3662 crystals each (so-called "Dees"). Each PbWO<sub>4</sub> crystal weighs around 1.5 kilogram and has a slightly tapered shape with a front face of  $2.2 \times 2.2 \text{ cm}^2$  in the barrel and  $2.86 \times 2.86 \text{ cm}^2$  in the endcaps. The crystals are 2.3 and 2.2 cm long in the barrel and endcaps, respectively. The total volume of the calorimeter including barrel and endcaps is  $11 \text{ m}^2$  and weighs a total of 92 tons. The ECAL detector layout is illustrated in Figure 3.6.

Having no longitudinal segmentation, the ECAL relies on an accurate reconstruction of the event primary vertex, provided by the tracker, in order to reconstruct the photon angle correctly.

The obtained energy resolution of the ECAL can be parametrized in three parts: a stochastic, a noise and a constant term [6]. It is given as

$$\frac{\sigma E}{E} = \frac{2.8\%}{\sqrt{E}} \oplus \frac{0.128 \text{ GeV}}{E} \oplus 0.3\%$$

where the constant values were estimated in an electron test beam. The constant term of 0.3% is dominated by the non-uniformity in longitudinal light collection [7], and one of the main goals of the detector design was to get this term below 1%. The energy resolution as a function of electron energy is shown in Figure 3.7.

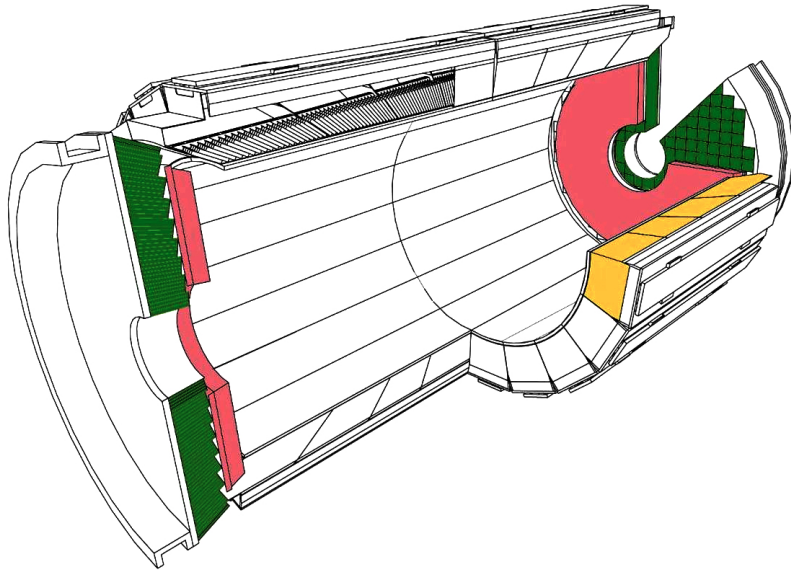


**Figure 3.6:** A schematic of the CMS electromagnetic calorimeter showing the barrel supermodules (yellow), the individual barrel crystals (black,top left), the endcap modules (green) and the pre-shower detectors (pink) [5].

### 3.2.4 Hadron calorimeter

Outside the crystal calorimeter is the hadron calorimeter (HCAL). It is the combined response of the ECAL and the HCAL that are responsible for measuring the energy of quarks, gluons and neutrinos through the reconstruction of particle jet energy and missing transverse energy. The HCAL is a sampling calorimeter, meaning it consists of alternating layers of dense brass absorber material and plastic scintillators. When a particle hits an absorber plate, it interacts with the absorber material and generates a shower of secondary particles which themselves generate new particle showers. These particles then generate light in the scintillating material which is proportional to their energy, and summing up the total amount of generated light over consecutive layers within a region, called a "tower", is representative of the initial particles energy. The hadron calorimeter is split into four regions: the inner (HB) and outer (HO) barrel, the endcap (HE) and the forward region (HF). A schematic of the CMS HCAL is shown in Figure 3.8.

The inner barrel lies within the superconducting solenoid volume and covers the pseudorapidity range  $|\eta| < 1.3$ . It consists of 36 identical wedges, each of which weighing 26 tonnes, split into two half barrels (HB+ and HB-). A photograph of the wedges taken during installation is shown in Figure 3.9.

The wedges are made up of flat brass absorber plates oriented parallel to the beam axis. These plates consist of a 4 cm thick front steel plate followed by eight 5 cm thick brass plates, six 5.6 cm thick brass plates and ending with a 7.5 cm thick steel back plate. The absorber plates are then alternated by 4 mm thick plastic scintillator tiles, the detectors active medium, which are read out using wavelength-shifting plastic fibers. The effective thickness of the barrel hadron calorimeter in terms of interaction lengths increases with the polar angle  $\theta$ , starting out at about  $5.8 \lambda_I$  at an angle of 90 degrees, and increases to  $10.6 \lambda_I$  at  $|\eta| < 1.3$ . As the energy resolution of the calorimeter depends on how much of the particles shower can be absorbed by the calorimeter, the quality of the energy measurement depends on its thickness. Due to the CMS design, the HB is confined to the volume between the ECAL

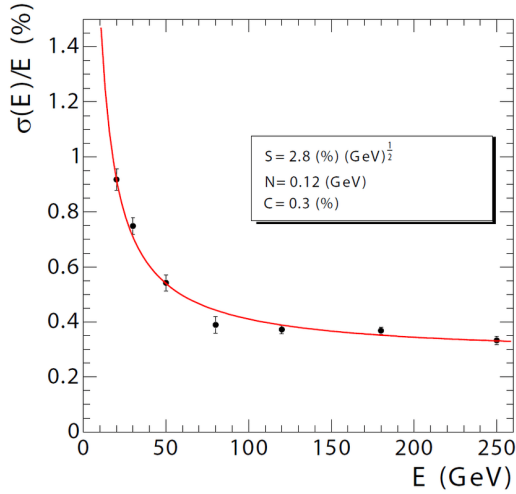


**Figure 3.7:** The ECAL energy resolution as a function of electron energy as measured in an electron test beam. [6]

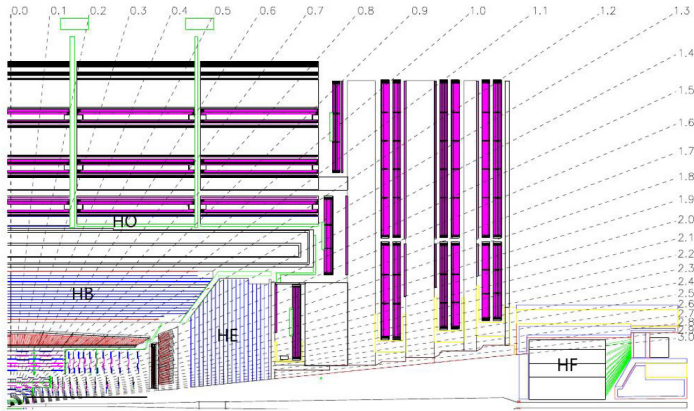


**Figure 3.8:** The four regions of the CMS hadron calorimeter: the inner (HB) and outer (HO) barrel, the endcap (HE) and the forward region (HF) [5]

(ending at a radius of 1.77 m) and the magnetic coil (starting at a radius of 2.95 m). In the central  $\eta$  region, the combined ECAL and HCAL interaction length is too small to sufficiently contain hadron showers. In order to ensure adequate sampling, especially of late starting showers, an additional layer of scintillator has therefore been added outside of the solenoid coil. This is the outer barrel (HO). It uses the coil itself as absorbing material and increases the total barrel calorimeter interaction length to  $11.8 \lambda_I$ . The hadron calorimeter endcaps (HE) are located in the forward region close to the beam pipe and covers the pseudorapidity range  $1.3 < |\eta| < 3.0$ , a region containing about 35 % of the particles produced in collisions. Due to its close proximity to the beam pipe, the endcaps need to handle extremely high rates as well as have a high radiation tolerance. As the resolution in the endcap region anyways is limited by pile-up and magnetic field effects, the hadron calorimeter endcaps were designed to minimize the cracks between HB and HE rather than having the best single-particle resolution (as is the case for the barrel). The absorber plates in the endcaps are mounted in a staggered geometry rather than on top of each other as is done in the barrel, in order to contain no dead material and provide a hermetic self-supporting construction. The HCAL is read out in individual towers with a size  $\Delta\eta \times \Delta\phi = 0.087 \times 0.087$  in the barrel, and  $0.17 \times 0.17$  at larger pseudorapidities. In order to obtain a completely hermetic calorimeter, an additional



**Figure 3.9:** The installation of the barrel HCAL wedges consisting of alternating layers of brass absorber plates and plastic scintillator, each weighing roughly 26 tonnes [8].

hadron forward calorimeter (HF) is added in the very forward region. Stretching out to a pseudorapidity of  $|\eta| = 5.2$ , this detector is located so close to the beam pipe that the particle rate exceeds  $10^{11}$  per  $\text{cm}^2$ , receiving roughly 760 GeV per proton-proton collision compared to an average of 100 GeV for the rest of the detector. It consists of a cylindrical steel structure with an outer radius of 130 cm and inner radius of 12.5 cm, located 11.2 meters from the interaction points. Also a sampling calorimeter, it consists of grooved 5 mm thick steel absorber plates, where the quartz fiber active medium is inserted into these grooves. The energy resolution of the CMS ECAL and HCAL for pions is measured in a test beam as a function of energy and is shown in Figure 3.10.

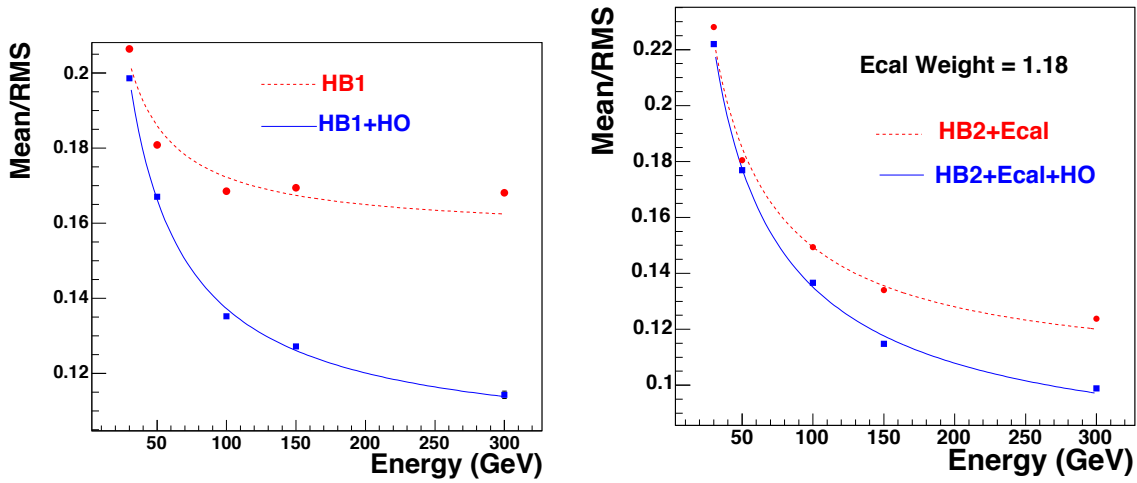


**Figure 3.10:** The calorimeter energy resolution as a function of pion energy using the HB only or HB+HO (left) and when adding ECal and HCal measurements (right) [9].

The typical HCAL electronics noise is measured to be 200 MeV per tower. The inclusion of the HO increases the resolution by 10 % for a pion energy of 300 GeV. The final energy resolution parametrization when using ECal+HB+HO is given by a stochastic and a constant

term, as for ECAL, and is

$$\frac{\sigma E}{E} = \frac{84.7\%}{\sqrt{E}} \oplus 7.4\%.$$

### 3.2.5 Muon chambers

The outer part of the CMS detector is dedicated to performing muon identification, momentum measurement and triggering. In order to do so, the muon system is made up of three types of gaseous particle detectors: drift tube (DT) chambers, cathode strip chambers (CSCs) and resistive plate chambers (RPCs), all integrated into the magnetic return yoke structure. In the barrel region, where particle rates are low and the magnetic field uniform, DT chambers are used and cover the pseudorapidity region  $|\eta| < 1.2$ . In the endcap regions, however, the muon rates and background levels are considerably higher and the magnetic field itself is large and non-uniform. Here, faster, finer segmented and more radiation hard CSCs are used, covering the region  $0.9 < |\eta| < 2.4$ . To ensure accurate muon triggering, a complimentary dedicated muon triggering system has been added both in the barrel and in the endcaps. Made out of RPCs, they provide an excellent time resolution at a sharp  $p_T$  threshold and cover the region  $|\eta| < 1.6$ . These chambers also assist in resolving ambiguities if multiple hits are present within a DT/CS chamber. A schematic overview of the muon system is shown in Figure 3.11.

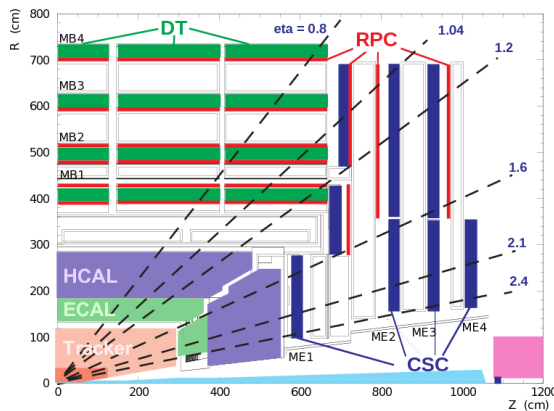


**Figure 3.11:** A schematic overview of the muon chambers: the DT chambers in the barrel, the CSCs in the endcaps and the redundant RPC system stretching out to  $|\eta| < 1.6$  and used for triggering purposes [10].

## 3.3 Trigger system: From collision to disk

With protons in CMS colliding at a rate of 40 MHz, there are only 25 nanoseconds between collisions available to process event data. One billion collisions take place every second, and with an event size of roughly 1 MB, it is impossible for all of these events to be read out and stored to disk. The CMS triggering system is therefore designed to make ultra fast high-quality decisions of which events are interesting and which events are not. The first stage of triggering, called Level 1 (L1), is designed to reduce the event rate to a maximum of 100 kHz through custom-designed hardware. It uses coarse data from the muons system and calorimeters in order to make a decision on whether the event should be recorded or not, a decision that needs to happen within 3.2 micro seconds. In the mean time, the full granularity data is stored in detector front-end electronics awaiting the L1 decision. The information

used by L1 is gathered in three steps. First, trigger primitives are created. For the muon system, these consist of track segments from each of the three types of muon detectors. For the calorimeter, trigger primitives are generated by calculating the transverse energy of a trigger tower (energy deposits with an  $\eta - \phi$  coverage of  $0.087 \times 0.087$ ) and assigning it to the correct bunch crossing. Trigger primitives from the calorimeter information is then passed on to a regional trigger which defines electron, muon and jet candidates. Some of this information is passed to the muon trigger (is particle a minimum ionizing particle?). The muon trigger combines the track information with the calorimeter information and selects a maximum of four muon candidates and calculates their momentum, position, charge and quality. This is done in the global muon trigger. The output from the regional calorimeter trigger is also passed to a global calorimeter trigger which provides information about the jets, total transverse energy and missing energy in the event. Combining the information from the global muon trigger and the global calorimeter trigger, the L1 decides whether to keep the event or not by combining several decisions by simple logic operations (AND/OR/NOT) to form up to 128 algorithms.

If the events is accepted, the full event information is read out at a rate of 100 kHz and passed to the so-called "event filter farm", a single processor farm made out of commodity computers. Here, the full precision of the detector data is used on order to take decisions based on offline-quality reconstruction algorithms. The goal of the HLT is to eventually reduce the event rate to an average rate of 400 Hz for offline event storage.

---

---

CHAPTER 4

---

Event reconstruction

## 4.1 Track and primary vertex reconstruction

The CMS tracker gets traversed by  $\mathcal{O}$  1000 charged particles at each bunch crossing, produced by an average of roughly 34 proton-proton interactions happening simultaneously. This makes track reconstructions extremely challenging, and is the reason why a high granularity of the tracker is vital. The average number of vertices per event for the whole Run 2 is shown in Figure 4.1, with a combined average of 34 number of interactions per bunch crossing.

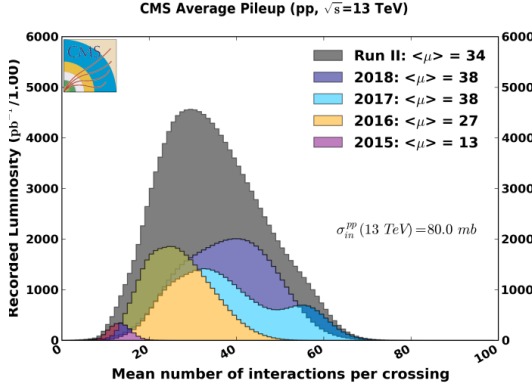


**Figure 4.1:** The average number of vertices per event in CMS during the Run 2 datataking [11].

Track reconstruction describes the process of taking hits from the pixel and strip detectors, combining them and estimating the momentum and flight direction of the charged particle responsible for producing the hits. It is an extremely computationally heavy process and is based on what is called a combinatorial Kalman filter [12]. A Kalman filter is an algorithm that uses time-dependent observations in order to estimate unknown variables, by proceeding progressively from one measurement to the next, improving the knowledge of the trajectory with each new measurement. The track reconstruction software in CMS (called the Combinatorial Track Finder (CTF)) constructs its collection of tracks by iteratively looping over the hits and reconstructing tracks, then removing those which are already used as inputs for a previous track. It starts from a seed in the inner most tracker layers, usually two or three hits, and then extrapolates the seed trajectories searching for additional hits to associate to that candidate. It then disregards tracks that fail certain criteria based on a  $\chi^2$  calculation taking both hit and trajectory uncertainties into account, as well as the number of missing hits. The track reconstruction algorithm is effective over the full tracker coverage range up to  $|\eta| < 2.5$  and can reconstruct particles with momenta as low as 0.1 GeV or particles which are produced up to 60 cm from the beam line. In the central region, particles with a momentum of 100 GeV have a  $p_T$ -resolution of roughly 2.8 %, a transverse impact parameter resolution of 10  $\mu\text{m}$  and a longitudinal impact parameter of 30  $\mu\text{m}$ .

In order to define the location and uncertainty of every proton-proton interaction in an event, primary-vertex reconstruction is performed. Primary vertices lie within a radius of a few millimeters of the beam axis and are defined as the common origin of groups of tracks. The reconstruction algorithm takes as input the reconstructed tracks from the previous step which pass certain selection criteria, clusters the tracks that share a common origin and then fit for the position of each vertex. Each track must have at least 2 hits in the pixel layers and no less than 5 hits in the pixel+strip as well as a  $\chi^2 < 20$  from a fit to the particle trajectory to be considered as input for the vertex finder. The primary vertex resolution is around 12  $\mu\text{m}$  in x and 10  $\mu\text{m}$  in z for vertices with at least 50 tracks.

Offline, all events are required to have at least one primary vertex reconstructed within a

24 cm window along the beam axis, with a transverse distance from the nominal interaction region of less than 2 cm. The reconstructed vertex with the largest value of summed physics object  $p_T^2$  is selected as the primary interaction vertex where the hard scattering process occurred.

## 4.2 The Particle Flow Algorithm

After track reconstruction, what remains is an incoherent collection of tracks, calorimeter clusters and hits in the muon chambers. In order to connect these, CMS uses an algorithm called Particle Flow (PF) [13] to combine the information obtained from all sub-detectors in order to infer which particles were actually produced in the event. The reconstructed physics object in the order of which they are reconstructed are

- Muons, through hits in the tracker and in the muon chambers
- Charged hadrons, through hits in the tracker and energy deposits in the calorimeters
- Neutral hadrons, through energy deposits in the calorimeters but no hits in the tracker
- Photons, through energy deposits in the ECAL but not in the HCAL and no hits in the tracker
- Electrons, through hits in the tracker and energy deposits in the ECAL

How these different particles propagate through the CMS detector is illustrated in Figure 4.2.

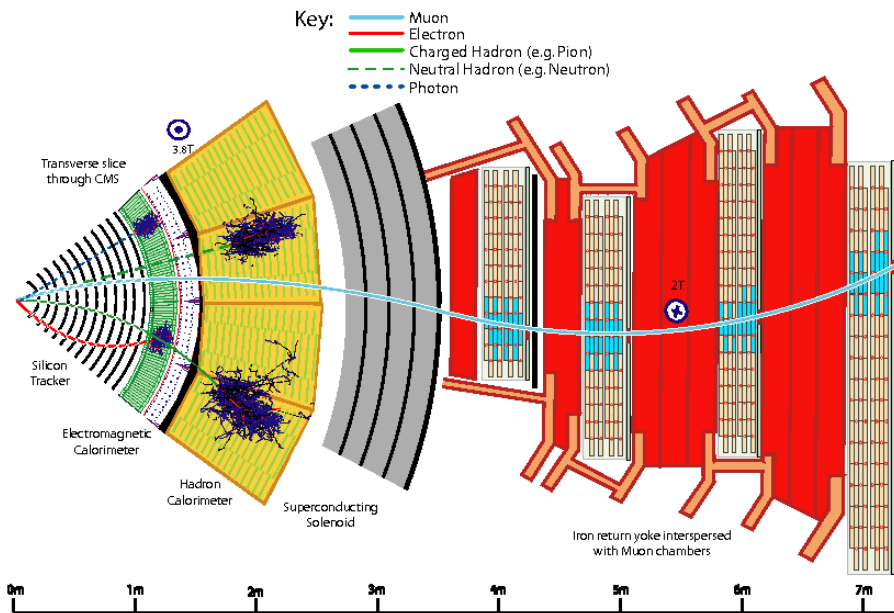


**Figure 4.2:** Particle interactions in the different subdetectors for a transverse slice through the CMS detector [13].

### 4.2.1 Reconstruction of the Particle Flow inputs

#### Electron tracking

Electron seeding is done in two different ways: ECAL-based or tracker-based electron seeding. In the ECAL-based method, electrons are seeded from ECAL clusters with  $E_T > 4 \text{ GeV}$ , where the position of the cluster is used to infer which hits in the inner tracker belongs to a given electron or positron. As a large fraction of the electron/positron energy is emitted through bremsstrahlung before even reaching the ECAL, ECAL superclusters covering a small window in  $\eta$  and a larger window in  $\phi$  are defined in order to fully contain the electron as well as its bremsstrahlung photons. As these superclusters are prone to contamination, tight isolation requirements need to be applied, leading to reconstruction inefficiencies. Therefore, an additional tracker-based seeding approach has been developed. All tracks with  $p_T > 2 \text{ GeV}$  are used as potential electron seeds. These tracks are then extrapolated to the ECAL and matched to the closest ECAL cluster. The ratio of the cluster energy to the track momentum is required to be 1. The electron candidates are then fit with a Gaussian-sum filter (GSF) [14] and required to pass certain criteria based on the score of a boosted-decision-tree (BDT) which combines the number of tracker hits, the  $\chi^2$  of the GSF track, the energy loss along the track, and the distance between the extrapolated track to the closest ECAL cluster.

#### Muon tracking

Muon tracking consists of two part: the muon spectrometer allows muons to be identified with high efficiency over the full pseudorapidity range, while maintaining a low background due to the absorbing calorimeter layers upstream. The inner tracker on the other hand, provides an accurate measurement of the muon momentum. Three muon quality flags are defined

- Standalone muon: Muon tracks based on hits in the DT or CSC only
- Global muon: A standalone muon track matched to a track in the tracker if the track parameters of the two are compatible
- Tracker muon: An inner track with  $p_T > 0.5 \text{ GeV}$ , a total momentum greater than 2.5 GeV and at least one muon segment matching the extrapolated inner track

Around 99% of muons produced within  $|\eta| < 2.4$  are reconstructed as a global muon or a tracker muon, and very often as both. If the global and tracker muon share the same inner tracker segment, the two are combined.

#### Calorimeter clusters

The calorimeter clustering is performed separately for each calorimeter subdetector (ECAL barrel and endcaps, HCAL barrel and endcaps and the preshower layers). The first step is to define cluster seeds from cells with an energy exceeding some predefined threshold and in addition is larger than the energy in its neighboring cells. Topological clusters are then formed by adding cells to the seed which has at least one corner in common with a cell already in the cluster, and that has an energy which is at least twice the noise level of the detector. In Figure 4.3, an example of calorimeter clustering for a five-particle jet is shown for the HCAL (left) and ECAL (right). In the HCAL (left), two seeds have been identified (gray filled areas) inside a topological cluster consisting of 9 cells. These are then defined as two HCAL clusters, with a position as indicated by the red circles. The green solid lines

correspond to charged tracks reconstructed in the tracker, both pointing to the center of the HCAL cluster seeds. The observed deposits left by the same particles are shown on the right in Figure 4.3, where the  $K^0_L$ ,  $\pi^-$  and the two photons from the decay of a  $\pi^0$  leave distinct clusters in the ECAL. The  $\pi^+$  leaves no energy deposit in this case.

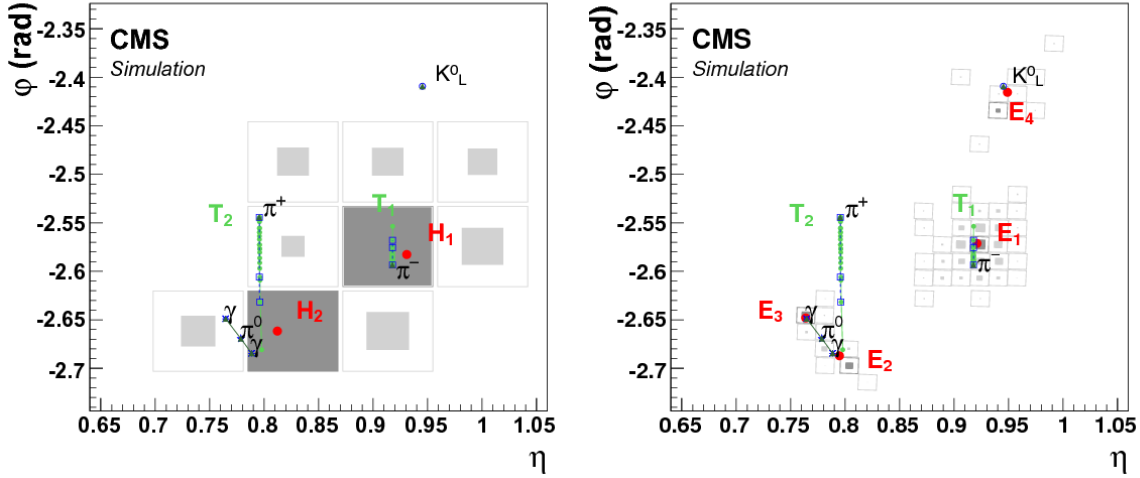


**Figure 4.3:** The  $\eta - \phi$  vies of calorimeter clusters generated by a five-particle jet in the HCAL (left) and in the ECAL (right). The squares correspond to calorimeter cells, where the inner area is proportional to the logarithm of the cell energy. Cluster seeds are depicted in dark gray. The dotted blue lines correspond to the simulated particle trajectory, while the green lines correspond to charged tracks reconstructed in the tracker [13].

## 4.2.2 Particle Flow identification

### The link algorithm

The link algorithm is the algorithm responsible for combining the particle flow elements from different subdetectors. It can test any pair of elements in the event based on specific requirements depending on the nature of the element, but is restricted to the nearest neighbors in the  $\eta - \phi$  plane. The outputs of the link algorithm are so-called *PF blocks* of linked elements, either directly linked or linked through having common elements.

- **Inner track - calorimeter cluster link:** The track is interpolated from its last hit, through the preshower layers, the ECAL and ending in the HCAL at an interaction length depth of 1. A link is made if the track is within the cluster area, where the areas is enlarged by up to a cell in each direction to account for detector gaps. In case several ECAL/HCAL clusters are linked to the same track, only the one with the smallest distance in  $\eta - \phi$  is kept.
- **Calorimeter cluster - cluster link:** A link between ECAL and HCAL clusters as well as between ECAL and preshower clusters is made when the cluster position of the more granular calorimeter is within the cluster envelope in the less granular calorimeter. Also here, if there is link overlap, only the link with the smallest distance is kept
- **Inner tracker -muon chamber link:** As described in Section 4.2.1

For each PF block, the reconstruction proceeds in the following order. First, muons are reconstructed and their corresponding PF elements removed from the PF block. Then the electrons are reconstructed, with the hopes of removing their corresponding bremsstrahlung photons from the list of PF elements. Energetic photons are reconstructed in the same step. Finally, neutral and charged hadrons are reconstructed.

## Muons

First, isolated global muons are selected by requiring the sum of track  $p_T$  and calorimeter energy deposits within a cone of  $\Delta R = 0.3$  not belonging to the muon track, to be smaller than 10 % of the muon  $p_T$ . If the muons are non-isolated, they are required to pass the tight muon requirement [15] and have at least three matching track segments in the muon detector or have matched calorimeter deposits compatible with being a minimum ionizing particle. Muons failing both the requirements above are kept if the standalone muon track is of high quality and have a lot of hits in the muon detectors, otherwise they are discarded. The muon momentum is defined from the inner tracker measurement if the muon  $p_T$  is less than 200 GeV. Otherwise, its chosen according to the track fit with the smallest  $\chi^2$  probability.

## Electrons

The electrons are seeded from a GSF track, as described in Section 4.2.1. To differentiate electrons from charged hadrons, the energy deposit in the HCAL within a distance of 0.15 in the  $\eta - \phi$  plane of the supercluster , is required to be less than 10 % of that of the supercluster. The electron candidate must further pass a requirement on the output of a dedicated electron-identification BDT, using inputs such as track-cluster distance, track  $\chi^2$  and number of hits as input. In this step, isolated photons are also reconstructed, seeded from ECAL superclusters with  $|E_T > 10 \text{ GeV}|$  and no link to a GSF track. All the tracks and calorimeter deposits used to reconstruct electrons and isolated photons are further removed from the list of PF blocks.

## Hadrons

Finally, after the removal of muons and electrons, the remaining hadrons and non-isolated photons are identified. HCAL clusters with no track link are defined as neutral hadrons, while ECAL clusters with no track link are defined as photons (photons are exclusively associated to the ECAL deposits as neutral hadrons leave only 3 % of their energy in the ECAL). The remaining HCAL clusters are then linked to one or more tracks from the inner tracker. In order to determine the particle content within a cluster, the sum of track momenta and the calorimeter energy is compared.If the calorimeter energy is compatible with the sum of track momenta, a particle for each track is inferred, with its corresponding energy taken from the track momentum. If the calorimeter energy is larger than the sum of track momenta, a photon or a neutral hadron is added, togehter with one charged hadron for each track within the cluster area.

### 4.3 Pile-up removal

Particles originating from proton-proton interactions not associated with the hardest primary vertex, are denoted pileup events. These distorts observables of interest from the hard scattering event and must be mitigated through dedicated pileup removal techniques

### 4.3.1 Charged Hadron Subtraction

As mentioned previously, primary vertices are reconstructed using tracks from charged hadrons. If a primary vertex does not correspond to the hard scattering vertex of the event, the charged hadrons (as reconstructed through Particle Flow) associated to this vertex (called pileup vertex) are removed from the event collection of particles and will not participate in any further object reconstruction. This method is denoted charged hadron subtraction (CHS).

### 4.3.2 Pile up per particle identification (PUPPI)

CHS was the default pileup removal algorithm in CMS until very recently. In 2014, a new pileup removal algorithm with improved performance was proposed; the pileup per particle identification (PUPPI) [16] algorithm. PUPPI uses a combination of local shape information, event pileup properties and tracking information to compute a weight describing the degree of "pileup-likeness" of a given particle. First, a variable denoted  $\alpha$  is computed based on the difference between soft radiation coming from pileup and the harder collinear QCD pattern. The shape of  $\alpha$  for charged particles is then used as a proxy for all pileup particles and is used on an event-by-event basis to calculate a weight for each particle. This weight in turn describes the degree to which particles are pileup-like and are used to rescale the particle four-momenta.

The shape variable for a given particle  $i$  is defined as

$$\alpha_i = \log \sum_{\substack{j \in \text{Ch,PV} \\ j \neq i}} \left( \frac{p_{T,j}}{\Delta R_{ij}} \right)^2 \Theta(R_0 - \Delta R_{ij}), \quad (4.1)$$

where  $\Theta$  is the step function and  $j$  refers to the neighboring charged particles from the primary vertex within a cone of radius  $R_0 = 0.4$ . Charged particles are defined as coming from the primary vertex if they are associated to the leading vertex of the event or are within a distance of  $d_z < 0.3$  cm from the leading vertex.

In order to determine the probability that a particle comes from pileup, a  $\chi^2$  calculation is performed. The probability is defined as

$$\chi_i^2 = \frac{(\alpha_i - \bar{\alpha}_{PU})^2}{RMS_{PU}^2}, \quad (4.2)$$

where  $\bar{\alpha}_{PU}$  is the median value of the  $\alpha_i$  distribution for pileup particles in the given event and  $RMS_{PU}$  is its RMS.

Each particle (neutral and charged) is then assigned a weight  $w_i = F_{\chi^2, NDF=1}(\chi_i^2)$ , where  $F_{\chi^2, NDF=1}$  is the cumulative distribution function of the  $\chi^2$  distribution with one degree of freedom. Particles with  $w_i < 0.01$  are rejected. In addition, a cut on the weighted  $p_T$  of neutral particles of  $w_i \cdot p_{T,i} > (A + B \cdot N_{PV})$  GeV is applied, where  $N_{PV}$  correspond to the number of reconstructed vertices in the event and A and B are tunable parameters.

The performance of the PUPPI algorithm compared to CHS for jet observables is shown in Figure 4.4.

The top row shows the absolute mass resolution (left) as well as the mass resolution as a function of  $N_{PV}$  for CHS jets (red) and PUPPI (pink) jets. The bottom row shows the corresponding quantities but for jet transverse momentum. A significantly better resolution on jet observables can be achieved using PUPPI compared to CHS.

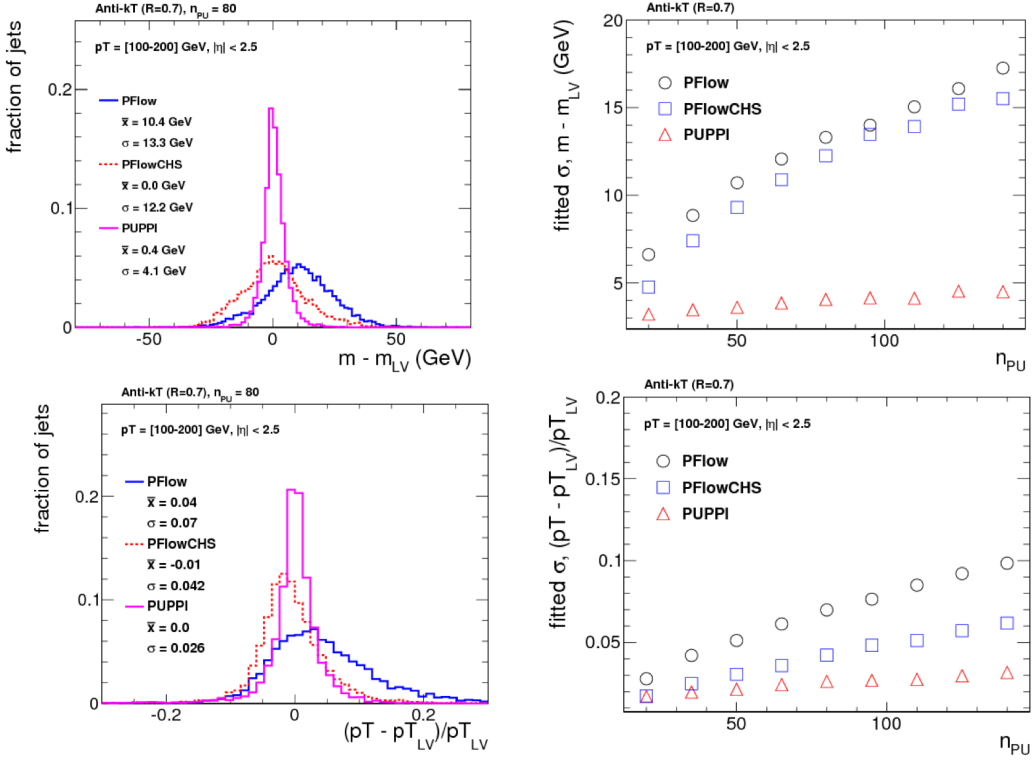


**Figure 4.4:** The mass (top) and  $p_T$  (bottom) resolution comparing PF only (blue), PF+CHS (red) and PUPPI (pink) jets. The absolute resolution (left) as well as the resolution as a function of the number of reconstructed primary vertices in the event (right) is shown [16].

## 4.4 Jet reconstruction

As explained in Section 1.1.4, quarks and gluons are never themselves visible in a detector. Within  $10^{-23}$  seconds, the timescale of the strong interactions, they fragment and hadronize into a collimated spray of hadrons, a so-called jet. In order to infer the properties of the original parton generating the jet, the properties of the full particle spray needs to be evaluated. Combining these particles algorithmically is non-trivial, and several algorithms designed to do, called jet clustering algorithms, exist. These provide a set of rules for grouping particles together into jets and are usually based on certain distance requirements between particles as well as rules for how to recombine their momenta. Thanks to Particle Flow, objects like charged hadrons, neutral hadrons and photons together with their estimated energy and direction are already defined, and jet clustering in CMS therefore consists of associating these particles to one common origin.

### 4.4.1 Jet clustering

The most common jet clustering algorithms used in hadron colliders are the Cambridge/Aachen algorithm [17], the  $k_T$  algorithm [18] and the anti- $k_T$  algorithm [19]. These are all sequential recombination algorithms, meaning they systematically go through each particle pair in the event and recombines them into one particle if the combination satisfies certain criteria. The rules, shared by all three algorithms, are as follows:

- For each pair of particles  $i$  and  $j$ , compute the longitudinally invariant distances

$$d_{ij} = \min(p_{ti}^{2p}, p_{tj}^{2p}) \frac{\Delta R_{ij}^2}{R^2}, \text{ with } \Delta R_{ij}^2 = (\eta_i - \eta_j)^2 + (\phi_i - \phi_j)^2 \quad (4.3)$$

$$d_{iB} = p_{ti}^{2p}, \quad (4.4)$$

where  $d_{ij}$  is a measure of the relative transverse momenta between the particles,  $\Delta R_{ij}^2$  is the distance between them in the  $\eta - \phi$  plane (which can be roughly translated into a jet radius),  $\Delta R^2$  corresponds to a distance parameter which controls the extension of the jet and  $d_{iB}$  is the distance between the particle and the beam. The parameter  $p$  is what separates the three algorithms from one another and controls the relative power of energy versus geometrical scales. For the anti- $k_T$  algorithm, it is defined as  $p = -1$ , for the  $k_T$  algorithm  $p = 1$  and in the case of the C/A algorithm,  $p = 0$ . The consequences of these choices are explained in detail below.

- Find the minimum distance of  $d_{ij}$  and  $d_{iB}$ .
- If this is  $d_{ij}$ , recombine particles  $i$  and  $j$  and return to step 1.
- If it is  $d_{iB}$ , the particle is defined to be a final state jet, and is removed from the list of particles. The algorithms proceeds back to step 1.
- Repeat until no particles remain.

## Infrared and collinear safety

There are two requirements that are extremely important when defining jet algorithms: They must be 1) *infrared* (IR) and 2) *collinear* (C) safe. *Infrared* safety corresponds to the requirement that if the final state particles are modified by the presence of a soft emission, and there are always soft emission in QCD events (both perturbative and non-perturbative), then the set of hard jets should remain unchanged. This is illustrated by the two left figures in Figure 4.5.

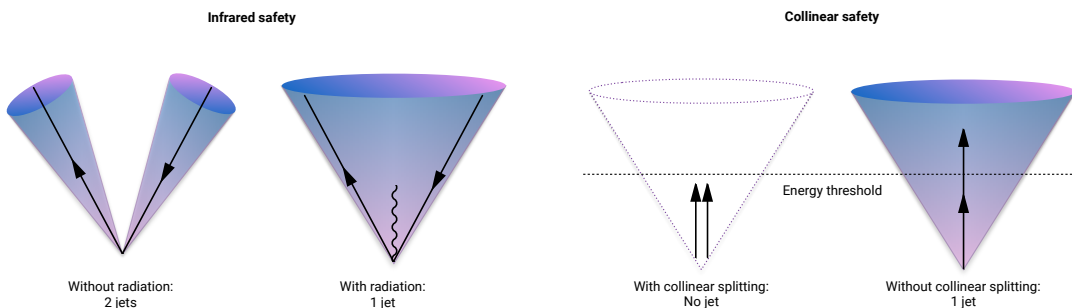


**Figure 4.5:** An illustration of what would happen for an infrared (left) and collinear (right) unsafe jet algorithm. If an algorithm is infrared unsafe, the presence of a soft emission changes the jet configuration. If an algorithm is collinear unsafe, then if a parton undergoes a collinear splitting this will change the configuration of the jet

Here, the algorithm is infrared unsafe: the presence of an additional soft gluon changes the jet configuration from 2 to 1 jets. If an algorithm is *collinear* unsafe, it means that the jet configuration would change if the hard parton undergoes collinear splitting (which a hard parton often does as part of the fragmentation process and which are also part of non-perturbative dynamics, like the decay of highly energetic hadrons). This is shown in the

two left figures of Figure 4.5, where a hard parton undergoing collinear splitting fails to be reconstructed due to its daughters being below the energy threshold of the algorithm.

All sequential recombination algorithms are trivially infrared safe.

## The $k_T$ algorithm

The  $k_T$  algorithm is the oldest of the sequential recombination algorithms and, due to its  $p = 1$  definition in the distance measures, follows the QCD branching structure in both  $p_T$  and in angle (in reverse). Soft particles are clustered together first, and the final step is the clustering of the two hardest particles. A consequence of this definition is that there is nothing that keeps arbitrarily soft particles from being defined as jets, and a minimum cut on the jet  $p_T$  should be introduced. Despite several favorable qualities, the  $k_T$  algorithm is not the algorithm of choice in most hadron collider experiments due to the irregular jets it produces, a consequence of clustering soft particles first.

## The Cambridge/Aachen algorithm

The Cambridge/Aachen algorithm, with  $p = 0$  in the distance measures, follows the QCD branching structure only in angle as the clustering order is based solely on spatial separation. The simplest of the algorithms, it recombines all pairs close in  $\Delta R$  until  $\Delta R_{ij} > R$ . The benefits of this is that the clustering history contains information about the presence of any geometrical substructure within a jet, a feature that will become important in Section 4.5.

## The anti- $k_T$ algorithm

The default jet clustering algorithm in CMS is the anti- $k_T$  algorithm [19], which follows the rules and distance measures above with  $p = -1$ . The algorithm favors the clustering of high- $p_T$ - high- $p_T$  and high- $p_T$  – low- $p_T$  particles first, disfavoring clustering between soft particles. That means the algorithm grows around a hard core, yielding jets with a well-defined cone shaped area. Together with being IRC-safe and insensitive to the underlying event (any event not arising the primary hard scattering process) and pileup, makes it the main jet algorithm in CMS.

A comparison of the resulting jet area in the  $\phi - \eta$  plane after clustering with either  $k_T$ , C/A and anti- $k_T$ , is shown in Figure 4.6. The z-axis correspond to the parton  $p_T$ . One can clearly see that when clustering with the anti- $k_T$  algorithm, the produced jets are circular, with a radius set by  $R$ , around the hardest parton.

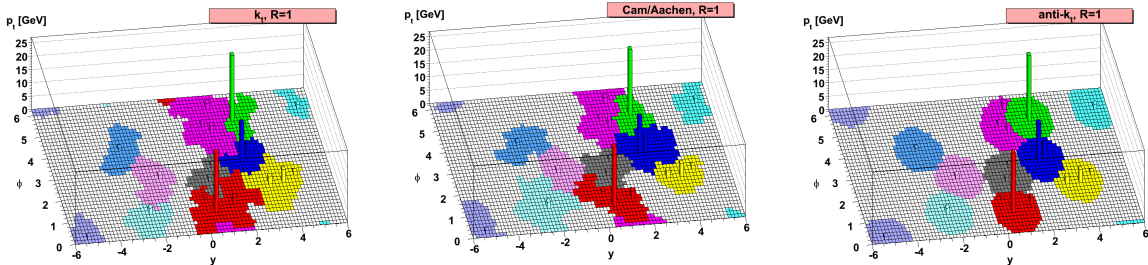


**Figure 4.6:** A comparison of the resulting jet cone area in the  $\phi - \eta - p_T$  plane after clustering the same event with three different jet algorithms:  $k_T$ , C/A and anti- $k_T$ . [19]

#### 4.4.2 PF jets in CMS

Jet algorithms in CMS mainly use PF candidate four-vectors as input and a pileup removal algorithm is usually applied before clustering occurs. If using CHS (Section 4.3.1), charged hadrons not associated to the primary vertex are discarded before clustering. If PUPPI is used (Section 4.3.2), all the PF candidates are reweighted based on how likely they are to have originated from pileup. For the anti- $k_T$  algorithm, CMS by default uses two jet cone sizes: R=0.4 and R=0.8. Jets with R=0.4, called PFAK4, are used for single-prong jets while the larger R=0.8 jets, PFAK8, are more often used when looking for jets containing multiple hard quarks/gluons in order to contain all the hadronization products.

#### 4.4.3 Jet energy corrections

### 4.5 Jet substructure reconstruction

In analyses looking for highly energetic ("boosted") vector bosons like, a main theme of this thesis, the opening angle between the vector boson quark decay products become so small that the highly boosted boson appears as a single large jet instead of two well-separated smaller jets. The distance between the two quarks, in the case of an hadronic decay, depends on the mass of the vector boson and its  $p_T$  and goes as

$$\Delta R = \frac{2M_V}{p_{T,V}}. \quad (4.5)$$

Above a W boson  $p_T$  of 200 GeV, the two quarks are therefore merged into a single large cone jet of size R = 0.8. A sketch of the two different situation is shown in Figure 4.7. If the W  $p_T$  is well below 200 GeV, its decay products are well-defined jets in their own right (left). However, once the W transverse momenta starts exceeding 200 GeV, both the quarks are completely contained within a single jet (right).

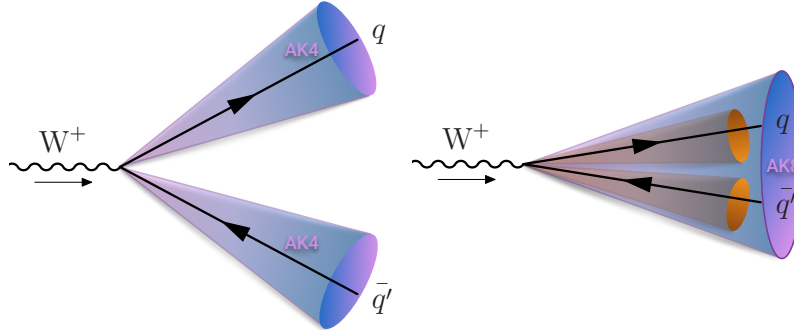


**Figure 4.7:** If the mass of the resonance is low enough, the quark decay products of each vector boson are well separated and clustered into distinguishable AK4 jets (left). If the transverse momentum of the vector boson is greater than 200 GeV, the vector boson decay products are merged into one single large cone AK8 jet.

In order to distinguish hadronically decaying vector boson from QCD quark/gluon jets, the jet mass would in principle be a good discriminant as we know the W has a mass of around 80 GeV while the quark/gluon mass is close to zero. At very high transverse momenta, however, the width (and therefore the mass) of QCD jets may become equally large. In addition, diffuse radiation caused by the Underlying Event and pileup give rise to a significant number of additional particles in the event contributing to the total jet mass. Therefore,

being able to accurately and efficiently separate highly boosted QCD jets from highly boosted vector bosons, requires other methods. In order to get rid of UE and pileup, algorithms like PUPPI and CHS can be used. Then, to improve the mass resolution further, dedicated grooming algorithms must be applied.

#### 4.5.1 Grooming

Grooming was introduced as a tool to improve the signal, most often W/Z/, mass resolution without significantly changing the background and signal event numbers. It consists of removing the softest parts of a jet in order to resolve its "true" mass, by means of reclustering and identifying soft particles within the jet which then are removed.

### Trimming

The trimming algorithm [20] is a grooming algorithm mostly used at trigger level in CMS (also where it is used in this thesis) due to it being less aggressive than other grooming algorithms. It works in the following way: Starting from a large jet clustered with either anti- $k_T$  or C/A (in the case of CMS), it reclusters the jet using the  $k_T$  algorithm in order to create subjets of some size  $r_{sub}$ . It then proceeds to check whether each subjet has a momentum fraction above a certain threshold,

$$p_{T,i}/p_{T,jet} > p_{T,frac}.$$

If the subjet fails this requirement, it is removed. The remaining subjets are then assembled into a new "trimmed" jet. The effect of trimming on real W jets and QCD quark/gluon jets for different values of  $r_{sub}$  and  $p_{T,frac}$  is shown in Figure 4.8. The best signal mass resolution is obtained with  $r_{sub} = 0.2$  and  $p_{T,frac} = 0.03$ , which is also the parameter setting that provides the best signal and background discrimination by pushing the QCD jet mass closer to zero. These are the default values of the tuned parameters of the trimming algorithm in CMS ( $r_{sub} = 0.2$  and  $p_{T,frac} = 0.03$ ).

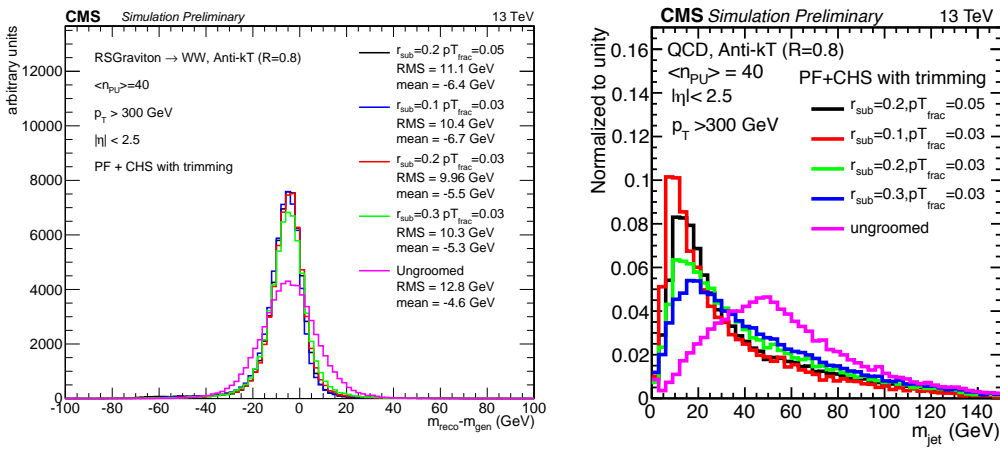


**Figure 4.8:** The effect of trimming on a signal jet (left) and a background jet (right) for different values of the tuned parameters  $r_{sub}$  and  $p_{T,frac}$  [21].

## Pruning

The pruning algorithm, in addition to removing soft particles, has an additional requirement on the distance between any recombination that are at wide angle. It proceeds by reclustering the jet with the C/A algorithm, requiring at each step that

$$\frac{\min(p_{T,i}, p_{T,j})}{p_{T,P}} > z_{cut} \quad \text{and} \quad \Delta R_{i,j} < D_{cut} = \frac{2r_{cut}m_{jet}}{p_T}.$$

The first requirement is a requirement on the hardness of the combination.  $p_{T,i}$  and  $p_{T,j}$  correspond to the transverse momenta of each protojet (single particle or group of particles already combined in a previous step) and  $p_{T,P}$  is the combined  $p_T$  of the two. The protojet with the lowest transverse momenta is removed if its hardness is below  $z_{cut}$ , or if it forms an angle wider than  $D_{cut}$  relative to the axis of the recombination of the two protojets. In CMS, the tuned parameters are set to  $r_{cut} = 0.5$  and where  $z_{cut} = 0.1$ . Figure 4.9 shows the ungroomed as well as the pruned jet mass distribution for signal (left) and background jets. The highest amount of signal and background separation in CMS, is achieved with  $r_{cut} = 0.5$  and  $z_{cut} = 0.1$ .

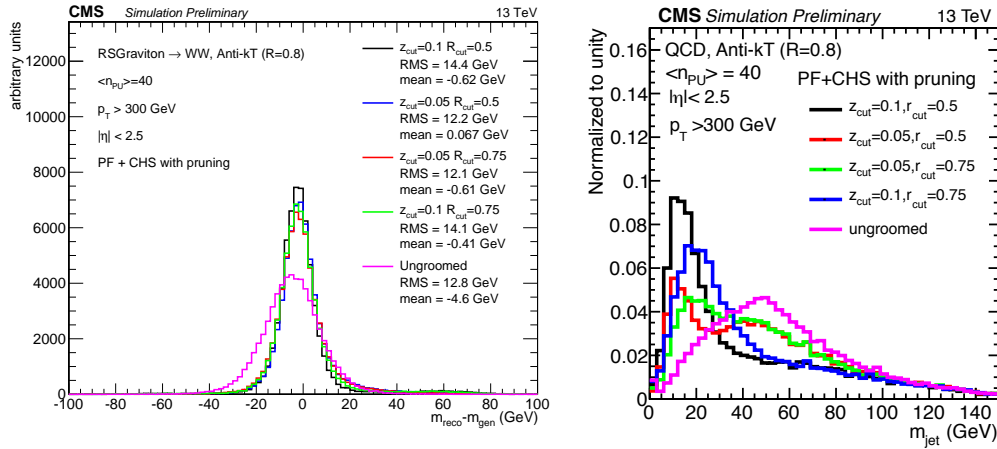


**Figure 4.9:** The effect of pruning on a signal jet (left) and a background jet (right) for different values of the tuned parameters  $z_{cut}$  and  $r_{cut}$  [21].

## Modified Mass Drop Tagger and Soft Drop

The modified mass drop tagger (mMDT) [22] (a modified version of the originally suggested mass drop tagger [23]) is based on the idea that a W/Z jet is formed by two quark subjets and that, therefore, the mass of each subjet is much smaller than their combined mass (and much smaller than the mass of the boson itself). A QCD jet is, on the other hand, formed by continuous soft radiation, meaning that its heaviest subjet should be close to the mass of the jet itself. The mMDT tagger therefore starts from an already clustered jet, reclusters it with the C/A algorithm and then declusters it again defining subjets  $s_1$  and  $s_2$ . It then looks for a significant mass drop going from total jet mass to the mass of each subjet, and checks that the splitting is not too asymmetric. The modified mass drop condition is generalized through the soft drop declustering method [24], simply called Soft Drop, which allows for different types of angular requirements to enter the condition. The Soft Drop condition is the following

$$\frac{\min(p_{T,1}, p_{T,2})}{p_{T,1} + p_{T,2}} > z_{cut} \frac{\Delta R_{12}}{R_0}^\beta.$$

If no significant mass drop occurred and the splitting is not to asymmetric, the condition is met and the full jet is deemed the softdrop jet. Otherwise only the highest- $p_T$  subjet is kept and the declustering continues. If the jet can not be declustered any further, it can either be removed from consideration, so-called "tagging"-mode, or deemed the final soft-dropped jet, "grooming"-mode. A  $\beta = 0$  corresponds to the modified mass drop tagger and removes all soft emission from the jet. For  $\beta > 0$ , soft radiation is removed, but some fraction of soft-collinear radiation is kept. Lastly, with  $\beta < 0$ , Soft Drop can remove soft as well as collinear radiation. The performance of Soft Drop on W jets and QCD quark/gluon jets for different values of  $\beta$  is shown in Figure 4.10. The modified mass drop tagger (Softdrop with  $\beta=0$ ) with  $z_{cut} = 0.1$  is the default Soft Drop settings in CMS, due to it providing the best signal/background discrimination while maintaining an excellent signal mass resolution.

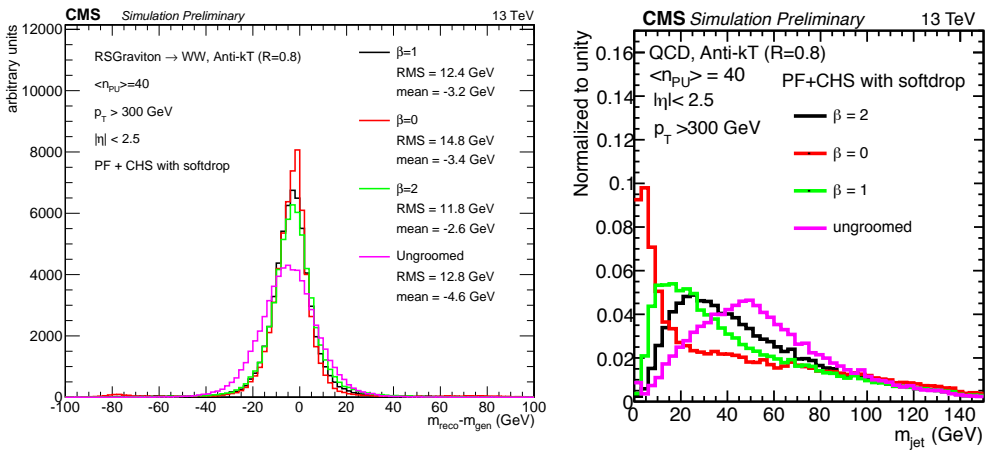


**Figure 4.10:** The effect of softdrop on a signal jet (left) and a background jet (right) for different values of the tuned parameters  $\beta$ .  $\beta = 0$  corresponds to the Modified Mass Drop Tagger, which is the default Softdrop setting in CMS [21].

### 4.5.2 N-subjettiness

After hopefully having resolved the particle mass with one of the grooming algorithms above, there is still discriminating information to be gathered from the jet structure itself. A W or Z jet consists of two well-defined high- $p_T$  subjets. A quark/gluon jet on the other hand, made from a single parton, consists of several large angle, asymmetric splittings, as illustrated in Figure 4.11.

The N-subjettiness algorithm [25] takes advantage of this fact by attempting to count the number of hard subelements within a jet. This is quantified through the n-subjettiness variable,  $\tau_N$ , defined as

$$\tau_N = \frac{1}{d_0} \sum_k p_{T,k} \min(\Delta R_{1,k}, \Delta R_{2,k}, \dots, \Delta R_{N,k}) \quad (4.6)$$

where  $k$  runs over all the jet constituents,  $p_{T,k}$  is the constituent transverse momentum and  $\Delta R_{i,k}$  is the distance between the constituent and candidate subjet axes. These subjet axes are obtained through a one-pass optimization procedure which minimizes N-subjettiness [26]. The normalization factor in front is given as

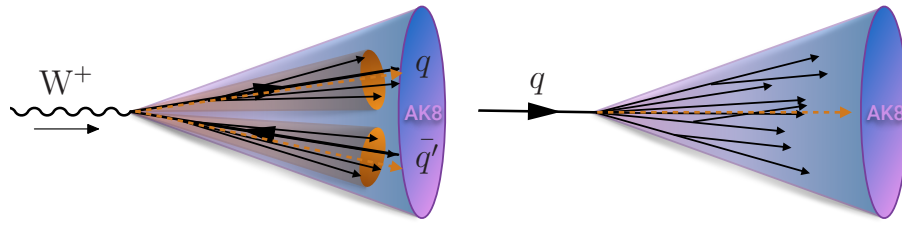


**Figure 4.11:** A jet stemming from the decay of a  $W$  will usually have two well-separated high- $p_T$  subjets, while a jet with a single-prong origin consists of several large angle splittings.

$$d_0 = \sum_k p_{T,k} R_0 \quad (4.7)$$

where  $R_0$  corresponds to the cone size of the initial jet. With this definition, jets with  $\tau_N = 0$  have most of its constituents aligned along the subjet axes. However, if  $\tau_N >> 0$ , a large fraction of the energy is radiated away from the subjet directions and are more likely to have more than  $N$  subjets. In CMS, and as recommended by the authors in [25], the ratio  $\tau_2/\tau_1$  is used to discriminate  $W$  jets from QCD jets. The reason for this is that, while signal jets are expected to have a large  $\tau_1$ , quark/gluon can similarly have large  $\tau_1$  due to the diffuse radiation present. However, QCD jets with a large  $\tau_1$  tend to have an equally large  $\tau_2$ , while signal jets do not, hence the ratio of the two provides greater separation power. In CMS, the n-subjettiness algorithm is by default applied to ungroomed jets. The distribution of  $\tau_{21}$  for signal and background jets with different pileup subtraction algorithms applied are shown in Figure 4.12, where  $\tau_{21}$  in combination with PF+PUPPI (green) yields a distribution most similar to the generated one (black).

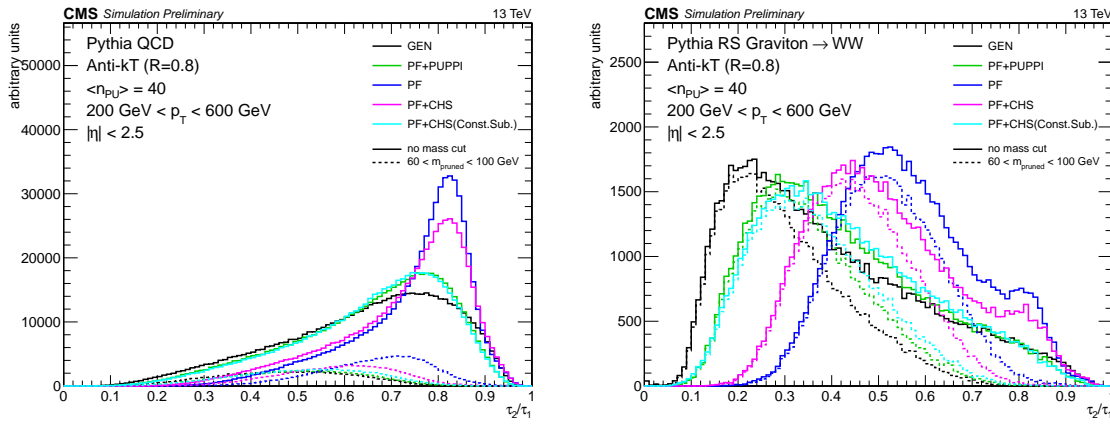


**Figure 4.12:** The distribution of the n-subjettiness ratio  $\tau_{21}$  for signal jets (left) and background jets (right) with different combinations of pileup subtraction algorithms applied. The solid lines corresponds to the  $\tau_{21}$  distribution with no mass cut applied, while the dotted lines are within a mass window of 60–100 GeV [21].

### 4.5.3 Vector boson tagging

In order to discriminate  $W$  and  $Z$  bosons from quark/gluon jets a combination of a groomer and shape-tagger (like n-subjettiness) is usually used. Typical values for a  $W$ -tagger are jet

groomed mass between 60 and 100 GeV and  $\tau_{21} < 0.5$ . Which combination and which cuts to use is analysis dependent, and have been optimized for each search presented in this thesis. The details are thoroughly explained in each section.

## Polarization effects

The vector boson polarization has a significant effect on the W-tagging efficiency. The helicity angle  $\theta$ , defined as the angle between the outgoing quark daughters of the W in the W bosons rest frame relative to its direction of motion [27], is very different for longitudinally polarized vector bosons,  $W_L$ , and transversely polarized vector bosons  $W_T$  [28]. Figure 4.13 shows the  $\cos \theta^*$  distribution for the outgoing quarks from a  $W_L \rightarrow q\bar{q}$  (black) and  $W_T \rightarrow q\bar{q}$  (red) decay, and it can be observed that transversely polarized W bosons decay with the quarks emitted closer to the vector boson direction of motion.

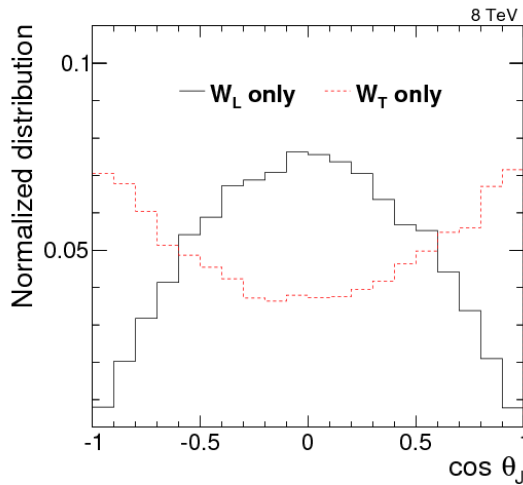


**Figure 4.13:** The helicity angle for generated quarks from  $W_L \rightarrow q\bar{q}$  (black) and  $W_T \rightarrow q\bar{q}$  (red) decays [28].

The consequence of this, is that there is a higher asymmetry in the transverse momenta of the two quarks from a  $W_T$  decay. This in turn makes grooming algorithms, designed to remove soft constituents of a jet, tend to reject particles coming from the softer quark, resulting in a lower jet mass and a drop in tagging efficiency. Figure 4.14 shows the W-jet tagging efficiency versus q/g jet mistagging rate for a selection on the jet pruned mass of  $60 \text{ GeV} < m_{\text{pruned}} < 100 \text{ GeV}$ , scanning  $\tau_{21}$  cuts (here for CA R=0.8 jets).

The tagging efficiency for transversely polarized W bosons (green) is significantly lower than the tagging efficiency for longitudinally polarized bosons (red). This can be explained by looking at the  $\cos \theta^*$  distribution on reconstructed level, using the C/A subjets, with a cut on the jet pruned mass of  $60 \text{ GeV} < m_{\text{pruned}} < 100 \text{ GeV}$ , shown in Figure 4.15. When comparing to the distribution at generator level with no groomed mass window applied, Figure 4.13, one can see that the  $W_T$  jets with  $\cos \theta^* \approx 1$  are completely removed.

This is due to two effects: the  $p_T$ -asymmetry explained above and the fact that the  $\Delta R$  distribution between the two quarks is much smaller in the case of  $W_L$ , making them more likely to be fully contained within a jet cone of R=0.8.

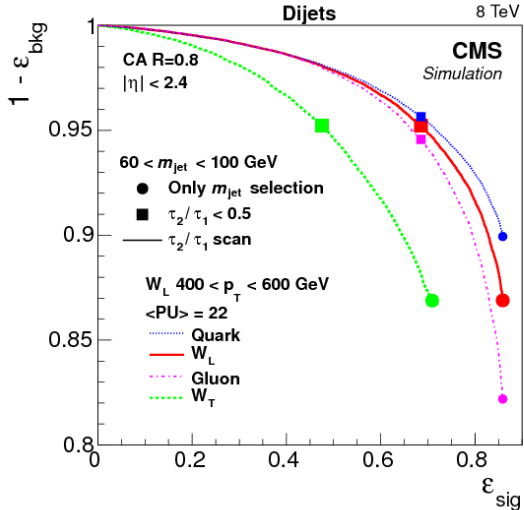


**Figure 4.14:** The helicity angle for generated quarks from  $W_L \rightarrow q\bar{q}$  (black) and  $W_T \rightarrow q\bar{q}$  (red) decays [28].

## 4.6 Monte Carlo Event Generators

Monte Carlo event generators offer a realistic estimate of high-energy collisions on an event-by-event basis, allowing us to estimate signal and background processes accurately. Simulated events are usually produced in three steps, describing a process from very short timescales up until hadronization and decay. First, a matrix element generator simulates the hard scattering process and subsequent decays. Secondly, the showering and hadronization of unstable particles is performed and, lastly, the final state particles are passed through a full detector simulation in order to reproduce a range of experimental effects.

General-purpose Monte Carlo (GPMC) generators, like HERWIG ++ [29] and PYTHIA 8 [30], deal with both perturbative as well as hadronization phenomena, simulating an event all the way up until detector simulation. In HERWIG ++ and PYTHIA 8, the hardest processes are only simulated at the lowest order of perturbative expansion, meaning  $2 \rightarrow 2$  or  $2 \rightarrow 3$  scatterings. In order to have tree-level matrix elements with an arbitrary final-state multiplicity, they can be combined with programs used to generate parton-level events at higher accuracy, which are then processed through showering and hadronization with the GPMC generators. One popular program for generating matrix elements is MADGRAPH [31]. This, however, still correspond to a tree-level (leading order) approach. To go to next-to-leading-order (NLO), meaning the inclusion of virtual corrections, two methods exist: MC@NLO [32, 33] and POWHEG [34]. These combine the full next-to-leading-order prediction for inclusive processes with the subsequent parton showers, either by a subtraction method regularizing the real contributions, or by a matrix-element correction of the parton shower branching probability. After hadronization, all final state particles are passed through a full simulation of the CMS detector. This is done with GEANT4 [35], where experimental effects like object reconstruction and detector resolution are accounted for.

For the work presented in this thesis, simulated samples of the Standard Model background processes are used to optimize the analysis and in some cases provide flexible background templates. QCD multijet production is simulated with four generator configurations: 1. PYTHIA standalone, 2. the LO mode of MADGRAPH matched with PYTHIA, 3. POWHEG matched with PYTHIA and 4. HERWIG++ 2.7.1 with tune CUETHS1 [36]. Top quark pair

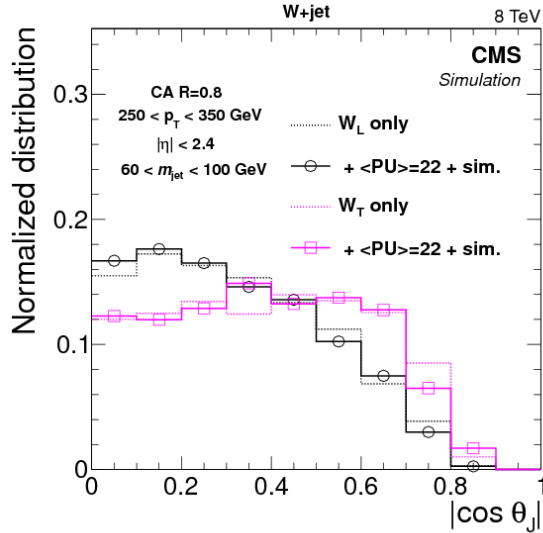


**Figure 4.15:** The helicity angle for subjets from  $W_L \rightarrow q\bar{q}$  (black) and  $W_T \rightarrow q\bar{q}$  (pink) decays. [28].

production is modeled with POWHEG and showered with PYTHIA unless otherwise stated.  $W+jets$  and  $Z+jets$  production are simulated with the leading-order (LO) mode of MADGRAPH matched with PYTHIA. Signal samples are generated with standalone PYTHIA.

All samples are processed through a GEANT4-based simulation of the CMS detector. To simulate the effect of additional proton-proton collisions within the same or adjacent bunch crossings (pileup), additional inelastic events are generated using PYTHIA and superimposed on the hard-scattering events. The MC simulated events are finally weighted to reproduce the distribution of the number of pileup interactions observed in data.

---

## CHAPTER 5

---

# Diboson resonance searches in CMS

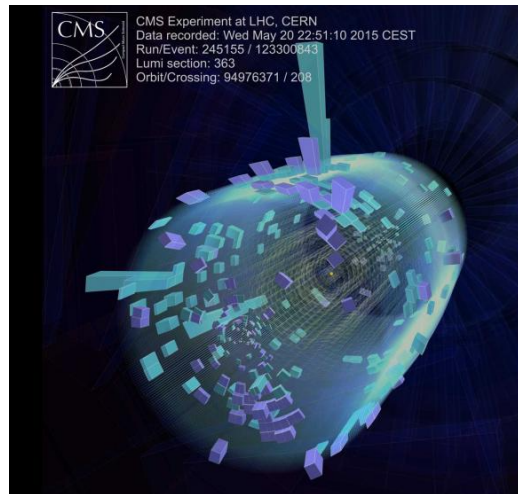
## Search I: First search for diboson resonances at 13 TeV

*When the LHC started its Run II data taking period in summer 2015, it would be the first time ever for a particle collider to produce collisions with center-of-mass energies of 13 TeV. The high-energy physics community was at cross roads. The Higgs boson for which the LHC was designed to find, had been discovered at the end of the previous data taking era. We were stuck with a Standard Model that we knew was, in the best case, in need of extensions and in the worst case an effective theory valid only in a certain region of phenomena phase space. The search program in Run II would therefore be oriented around two main efforts: Precision measurements of the newly discovered Higgs boson and searches for Beyond Standard Model physics.*

*I started my PhD four months before the first 13 TeV collisions took place and was faced with the following questions: What was the most interesting search that could be done on a short time scale (to be presented 6 months after first collisions, at the CERN end-of-year Jamboree), would be manageable for a student with no previous analysis experience and would be robust enough incase there were issues with the never-before-validated 13 TeV Monte Carlo?*

*Every year in high-energy physics has its hot topic: In 2018, this was most certainly leptoquarks (driven by a dimuon excess around 30 GeV), in 2016 and 2017 it was diphoton resonances (with  $> 3\sigma$  excesses observed both in ATLAS and in CMS). And in 2015 during the 13 TeV LHC start-up, it was centered around diboson resonances in the all-hadronic final state. The choice was therefore clear: My first analysis would be a search for diboson resonances in the boosted dijet final state. With a background model based on a smooth fit to data in the signal region, eliminating the need for accurate QCD MC predictions, this was a simple one-background only (QCD) analysis, feasible for a first-year PhD student to finalize within a year. Despite its straightforwardness, due to observed 8 TeV excesses, it was in addition considered a high-profile analysis.*

*It became one of the first "boosted" searches published with 13 TeV data as well as the first search to take advantage of dedicated grooming triggers.*



### 5.0.1 A small bump

On June 2nd 2015, the day before CMS recorded its first ever 13 TeV event, a pre-print appeared on the arXiv "Search for high-mass diboson resonances with boson-tagged jets in proton-proton collisions at  $\sqrt{s} = 8$  TeV with the ATLAS detector" [31]. It was an analysis of the full ATLAS Run 1 dataset, corresponding to  $20.3 \text{ fb}^{-1}$ , searching for heavy resonances decaying to vector bosons in the all-hadronic state. The analysis documented a  $3.4\sigma$  excess for a heavy resonance decaying to W Z around 2 TeV. The corresponding CMS analysis, published the previous year, had a  $1.3\sigma$  excess at roughly the same resonance mass, but mostly compatible with a W W final state hypothesis [37]. Figure 5.1 shows the corresponding dijet invariant mass spectrum as seen by ATLAS (left) and the upper limit on the production times the cross section for a  $G_{\text{Bulk}}$  decaying to W W (right) as documented by CMS.

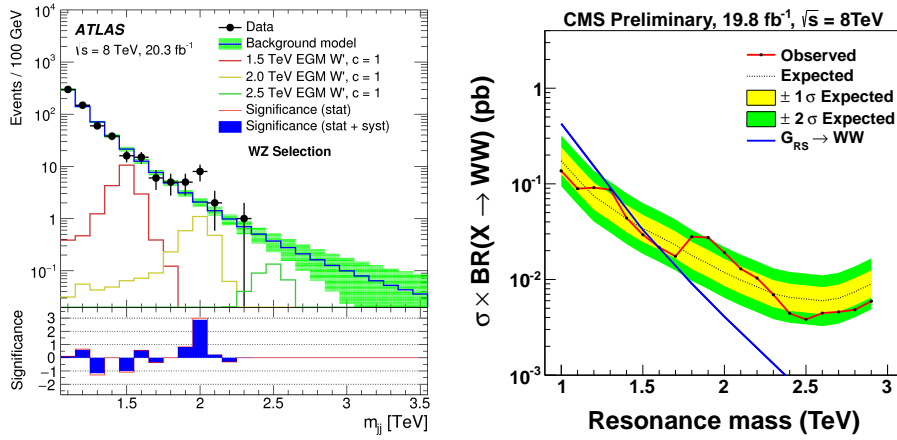


**Figure 5.1:** The mass (top) and  $p_T$  (bottom) resolution comparing PF only (blue), PF+CHS (red) and PUPPI (pink) jets. The absolute resolution (left) as well as the resolution as a function of the number of reconstructed primary vertices in the event (right) is shown [16].

The two measurements were found to be compatible, favoring a heavy resonance with a production cross section of around  $5 \text{ fb}^{-1}$  and a mass between 1.9 and 2.0 TeV decaying to either W W, W Z or Z Z [38]. Figure 5.2 show the obtained p-value of the ATLAS (red) and CMS (blue) search as well as their combination (black).

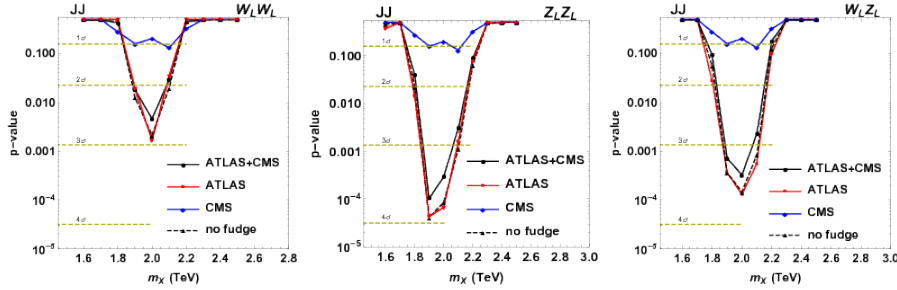


**Figure 5.2:** p-values as a function of resonance mass obtained with an emulation of the ATLAS (red) and CMS (blue) searches as well as the combination of the two (black). Here for a W W (left), W Z (middle) and Z Z (right) hypothesis [38].

The combination of the two excesses and the timing of the ATLAS paper, naturally lead to some excitement and in the coming weeks, the arXiv was flooded with theory papers seeking an explanation for the measurements. The pressure on seeing early results with 13

TeV data in the VV all-hadronic final state was high, and it was agreed with CMS Physics Coordination that a preliminary analysis would be ready in December that same year, only 6 months after the first 13 TeV collision.

### 5.0.2 Analysis strategy

When a resonance  $X$  with a mass above 1 TeV decays into a vector boson pair, the bosons have a very high energy ( $\tilde{p}_T = M_X/2 = 500$  GeV, assuming  $X$  is produced at rest). The boson is co-called "boosted". The decay products of a hadronically decaying boosted vector boson, will therefore not appear as back-to-back in the lab frame but rather be very collimated, as described in Section 4.5. This results in a final state with two large high- $p_T$  jets, where an AK R=0.8 jet is expected to fully contain the two quarks coming from the vector boson decay. This is illustrated in Figure 5.3.

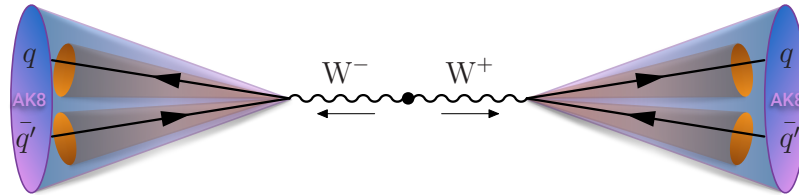


**Figure 5.3:** If a heavy ( $> 1$  TeV) resonance decays into vector bosons, the transverse momentum of each boson will be large and its decay products are merged into one single large cone AK8 jet.

The two jets are both expected to have a mass around the  $W$  or  $Z$  mass, and some intrinsic substructure stemming from their two-prong origin. The invariant mass of the dijet system,  $m_{jj}$ , should be roughly equal to the resonance mass  $M_X$ . This dijet system is the final state under scrutiny and the dijet invariant mass is the parameter of interest. Both  $WW$  and  $ZZ$ , as well as  $WZ$  final states are of interest.

The main background for such an analysis, is QCD multijet events. As mentioned in Section 4.5, quark/gluon jets can obtain a high mass due to diffuse radiation and QCD processes have such a large cross section that the number of QCD jets with a mass compatible with the  $W$  mass can be large. In order to discriminate between the two, we take advantage of three properties: 1. The groomed mass of signal and background jets should be very different, 2. signal jets should appear two-prong like, quark/gluon jets not, and 3. the dijet invariant mass for a signal process should peak around the resonance mass while the QCD spectrum is predicted to be smoothly falling (we will get back to why this assumption is justified in Section 5.0.5). The strategy therefore consists of performing a smoothness test on  $m_{jj}$  of the observed data, a so-called "bump-hunt", by assuming that the signal will appear as a bump on top of a smooth distribution. This is illustrated in Figure 5.4.

The benefit of such a method is that there is no need for any background simulation and the strategy is simple and robust. The disadvantage is that the analysis is intrinsically limited to regions where the dijet invariant mass spectrum is smooth, hence must avoid regions with continuities due to trigger turn-ons or kinematic selections.

### 5.0.3 Data and simulated samples

The data analyzed in this search correspond to a total integrated luminosity of  $2.7 \text{ fb}^{-1}$  collected at a center-of mass energy of 13 TeV between June and December 2015. The

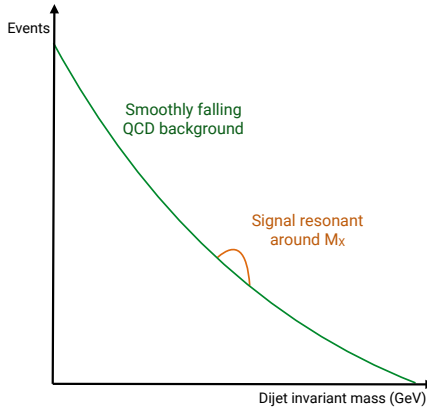


**Figure 5.4:** The search strategy consists of looking for signal "bumps" in the dijet invariant mass on top of a smoothly falling QCD multijet background.

instantaneous luminosity of the LHC during this run was around half of the design luminosity ( $0.5 \times 10^{34} \text{ cm}^{-2} \text{ s}^{-1}$ ), with an average number of primary vertices per event of  $\langle \mu \rangle = 13$ .

The bulk graviton model (see Section 1.2.2) and the HVT model ( $W'$  and  $Z'$ , see Section 1.2.3) are used as benchmark signal processes. In these models, the vector gauge bosons are produced with a longitudinal polarization in more than 99% of the cases, which leads to a 24% higher acceptance per boson for reasons explained in Section 4.5.3. For the HVT model, a scenario (model B) with  $g_V = 3$ ,  $c_H = -0.976243$ , and  $c_F = 1.02433$  is chosen, where the heavy resonance predominantly couple to bosons and the coupling to fermions is suppressed. The bulk graviton samples were generated with  $\tilde{k} = 0.5$ . The resonance masses considered lie in the range 1.2 to 4 TeV and has a width of 0.1% of the resonance mass. The narrow width allows us to neglect detector effect as the natural width of the resonance is smaller than the detector resolution, making the modeling of detector effects on the signal shape independent of the model. All signal samples are generated at leading order with MADGRAPH5\_AMC@NLO v2.2.2 [39]

Simulated samples of the production of QCD multijet events are generated to leading order using PYTHIA version 8.205 [40] with the CUETP8M1 tune [36].

## 5.0.4 Event selection

### Triggering

The first selection to be confronted in any analysis, is the trigger selection. Due to an overwhelming QCD background in all-hadronic final states, the threshold for fully-hadronic triggers is very large in order to keep the trigger rate low (preferably around 10-30 Hertz). In this analysis, we therefore decided to take advantage of triggers that place requirements on the jet groomed mass in addition to the "standard" triggers based on the scalar sum of jet transverse energy  $H_T$ . These "boosted" triggers were never before tested in data, and this analysis was the first published result taking advantage of grooming at the trigger level in CMS. The following  $H_T$ -based triggers (called inclusive triggers in the following) are used

- HLT\_PFHT650\_WideJetMJJ900DEtaJJ1p5
- HLT\_PFHT650\_WideJetMJJ950DEtaJJ1p5,
- HLT\_PFHT800

where the two first triggers apply an additional cut on the  $|\Delta\eta|$  between the two jets for reasons that will be explained below. In addition, two grooming triggers cutting on the jet trimmed mass (see Section 4.5.1) of 30 and 50 GeV are used

- HLT\_AK8PFJet360\_TrimMass30
- HLT\_AK8PFHT700\_TrimR0p1PT0p03Mass50.

The tuneable parameters for the trimming algorithm at HLT are  $r_{sub} = 0.2$  and  $p_{T,frac} = 0.03$ . The HLT\_AK8PFJet360\_TrimMass30 trigger is seeded by single-object Level 1 triggers with jet  $p_T$  thresholds of 176 or 200 GeV (L1\_SingleJet176 or L1\_SingleJet200), and the remaining triggers requires an online  $H_T > 150$  or 175 GeV (L1\_HTT150 or L1\_HTT175).

In order to avoid any kinks in the dijet invariant mass spectrum due to the presence of a trigger turn-on, we need to define for which dijet invariant mass the analysis triggers are fully efficient ( $> 99\%$ ), then cut away everything below that point.

In order to estimate the trigger efficiency, we use a lower threshold prescaled  $H_T$  trigger HLT\_PFHT650 as reference trigger. This trigger has a prescale of 40, meaning it only stores information for every 40 events that trigger it, and is seeded by L1 triggers L1\_HTT150 or L1\_HTT175. We then define the efficiency as

$$\text{Efficiency} = \frac{N_{trigger+ref}}{N_{ref}}$$

where  $N_{trigger+ref}$  corresponds to events passing the trigger under study as well as the reference trigger and  $N_{ref}$  corresponds to all events passing the reference trigger. Figure 5.5 shows the trigger turn-on curves as a function of dijet invariant mass for jets where one of the jets is required to have a pruned mass larger than 65 GeV (in other words, compatible with a W jet). A sharp turn-on for the inclusive triggers (top left) is observed, reaching the 100% efficiency plateau for dijet masses of around 1.0–1.1 TeV. The grooming triggers, however, turn on more slowly and are not fully efficient before dijet invariant masses of around 1.2 TeV (top right). The real power of the grooming triggers become clear when adding them in OR with the  $H_T$ -based triggers. The bottom plot in Figure 5.5 compares the trigger turn-on curves as a function of dijet invariant mass for jets passing one of the three inclusive triggers only, one of the grooming triggers only and when combining all of them. Here, one can see that the 99% efficiency threshold is lowered by 75 GeV when including the substructure triggers, once substructure is required at analysis level. This allowed for the analysis to start at a dijet invariant mass of 1 TeV.

As a measure of the performance of the grooming triggers, we have in addition looked at the trigger efficiencies as a function of the offline groomed mass (pruned and softdrop, see Sections 4.5.1 and 4.5.1), for the grooming trigger with the lowest mass threshold (30 GeV). This is shown in Figure 5.6, where an additional cut on the jet transverse momentum of one of the jets of 600 GeV is required and no other mass cut is applied. The trigger plateau is reached for offline groomed-jet masses around 50 GeV, an impressively sharp turn-on for a trigger paths first test i data (as reference trigger for this study, the prescaled trigger HLT\_PFAgent320 was used).

## Preselection

After trigger selections and the corresponding requirement of a dijet invariant mass above 1 TeV to ensure a smooth falling background, the process of maximizing the signal significance while keeping the background low can begin. This is done through a set of jet requirements.

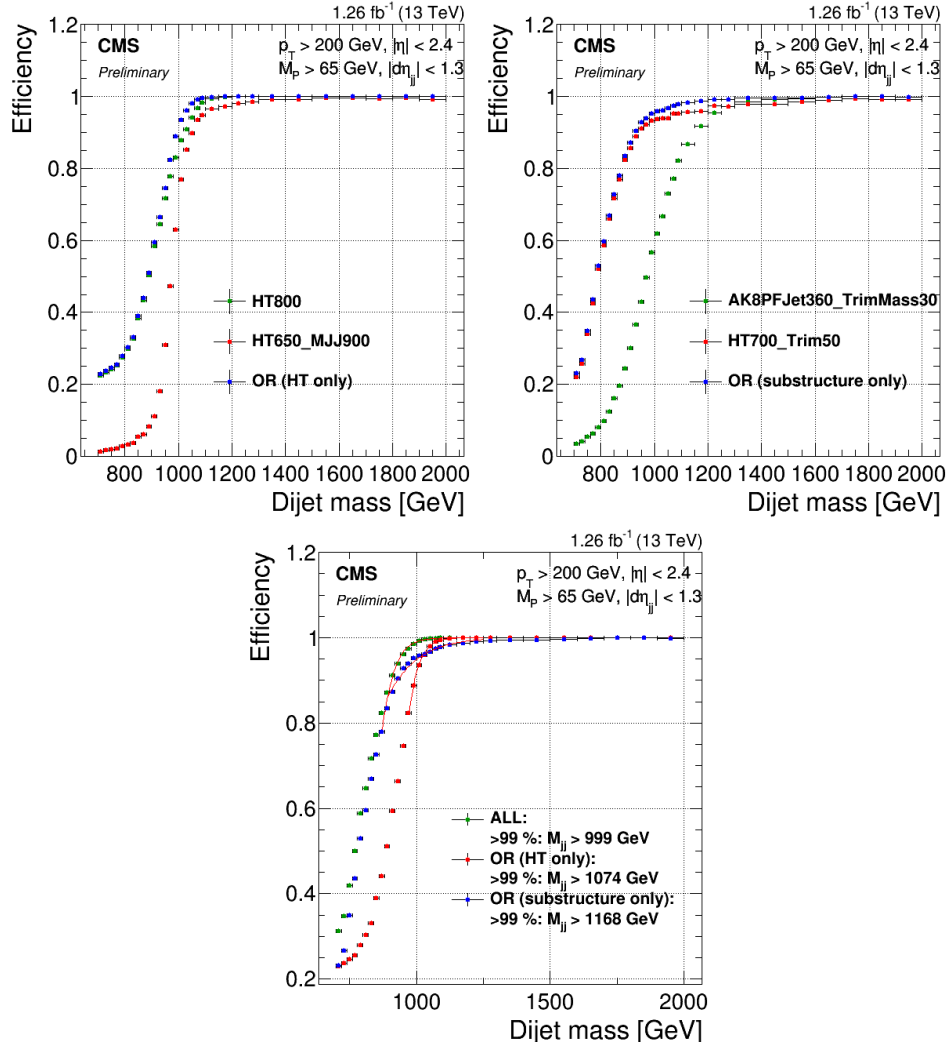


**Figure 5.5:** Top: Efficiency for the inclusive triggers (top left) and the grooming triggers (top right) as a function of dijet invariant mass for jet pairs where one jet has a pruned mass larger than 65 GeV. Bottom: Comparison of trigger efficiencies for jets passing one of the HT-triggers only (red), for jets passing one of the grooming-triggers only (blue) and for jets passing one of the HT-triggers or one of the grooming triggers (green). Here as a function of dijet invariant mass for all jet pairs passing loose selections and where one jet has a pruned mass larger than 65 GeV. The 99% efficiency threshold is lowered by 75 GeV when including substructure taggers.

The jets used in this analysis are clustered with the anti- $k_T$  jet clustering algorithm with a clustering parameter of  $R = 0.8$  (see Section 4.4) to allow containment of the full vector boson decay products. These jets are further required to pass certain jet identification requirements provided by the JetMET POG [41], in order to distinguish them from fake jets. These are as follows:

- Number of Constituents  $> 1$ , for all jet  $\eta$
- Neutral Hadron Energy Fraction  $< 0.90$ , for all jet  $\eta$
- Neutral EM Energy Fraction  $< 0.90$ , for all jet  $\eta$
- Charged Hadron Multiplicity  $> 0$ , for jet  $|\eta| < 3.0$

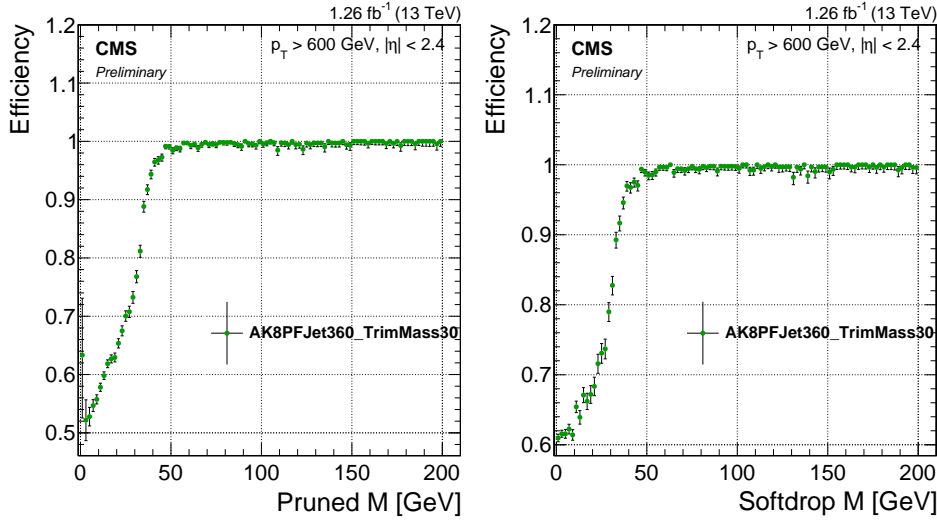


**Figure 5.6:** Efficiency for the lowest threshold grooming trigger as a function of pruned-jet (left) and softdrop-jet (right) mass for jets with  $p_T > 600 \text{ GeV}$ .

- Charged EM Energy Fraction  $< 0.99$ , for jet  $|\eta| < 3.0$

Jets are further corrected for nonlinearities in  $p_T$  and rapidity using standard jet energy corrections at CMS as described in Ref. [42] for  $R=0.8$  anti- $k_T$  jets. As we know that a minimum transverse of 200 GeV is required for the decay products of a W/Z to be fully contained within an  $R=0.8$  jet, events are further selected by requiring at least two jets with  $p_T > 200 \text{ GeV}$ . These are in addition required to be central, with an  $|\eta| < 2.4$ .

The two highest  $p_T$  jets in the event passing these criteria are selected as potential vector boson candidates. As our main background is QCD multijet events, we further take advantage of the fact that the angular distribution between these, mainly t-channel, processes are very different from the s-channel signal processes under study. The crosssection for QCD t-channel processes as a function of the opening angle with respect to the beam axis ( $\theta^*$ ), exhibit a pole around  $\cos \theta^* = 1$ , meaning QCD t-channel jets are mostly forwardly produced, with an opening angle with respect to the beam axis close to zero. The signal jets on the other hand, produced through an s-channel process, are concentrated in the barrel region. We therefore require the jets to have a separation of  $|\Delta\eta| < 1.3$  in order to reduce the QCD multijets background. The distribution of  $|\Delta\eta|$  between the two highest- $p_T$  jets for QCD as well as for different signal scenarios, is shown in Figure 5.7

A cut of  $|\Delta\eta|_{jj} < 1.3$  makes sure to remove the t-channel pole at  $\cos \theta^* = 1$  and is in addition found to yield the best separation between signal and the QCD background.

The  $p_T$ ,  $\eta$ , dijet invariant mass and  $|\Delta\eta|_{jj}$  distribution for the two leading jets in the event after the above preselections have been applied is shown in Figure 5.8.

## Vector boson tagging

After preselections, we take advantage of the jet substructure algorithms described in Section 4.5 to further separate boosted W/Z jets from the QCD multijets background. In the 8 TeV analysis [37] published the previous year, the pruning algorithm was the groomer of choice. However, recent progress had been made in the development of alternative groomers which had favorable properties from a theoretical point of view (see Sections 4.5.1 and 5.0.13). We therefore studied two different grooming algorithms: pruning and softdrop (with  $\beta = 0$

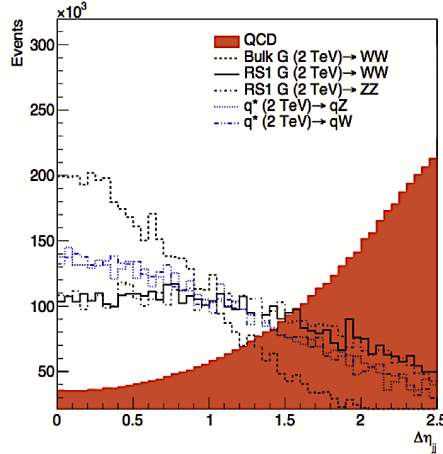


**Figure 5.7:**  $|\Delta\eta|$  between the two highest- $p_T$  jets for QCD jets and jets stemming from different signal scenarios.

and  $z_{cut} = 0.1$ ). A comparison of the softdrop (dotted lines) and pruned (solid lines) jet mass for W, Z and H jets is shown in Figure 5.9.

One of the first observations we made comparing the two groomers, was that there appeared to be a strong dependence of softdrop mass on the jet  $p_T$ . Figure 5.10 shows the pruned (left) and softdrop (right) mass distributions for W jets coming from the decay of a  $G_{bulk}$  with a resonance mass of  $0.8 \text{ TeV} < M_X < 4 \text{ TeV}$ . While the pruned jet mass mean appeared stable as the jet transverse momenta of the jet increased ( $p_T \sim M_X/2$ ), the softdrop jet mass mean shifted towards lower values as jet  $p_T$  increased.

In order to investigate whether this was a reconstruction effect or an algorithmic effect, we additionally looked at the pruned and softdrop mass for generator level jets (jets clustered with generator level particles before they are passed through the detector simulation). Figure 5.11 shows the reconstructed (solid line) and generator level (dotted line) jet mass distributions after pruning (left) or softdrop (right) have been applied. Again, the distributions are compared for jets with very different  $p_T$  profiles, here for W jets coming from a  $G_{bulk} \rightarrow WW$  of mass  $M_X = 0.8 \text{ TeV}$  (red), roughly  $p_T \sim 400 \text{ GeV}$ , and  $M_X = 2.0 \text{ TeV}$  (blue),  $p_T \sim 1 \text{ TeV}$ . Interestingly, we observe a  $p_T$ -dependent mass shift already for generator level softdrop jets (comparing the dotted lines in the right plot); an effect further enhanced at reconstruction level. This effect is not present for pruned jets, neither at generator level nor reconstruction level.

The observed softdrop mass  $p_T$ -dependence was problematic, due to the fact that it would require a  $p_T$  dependent mass window. This would again require several different measurements of data to simulation tagging efficiency scale factors, for the respective mass windows, or a significantly higher uncertainty on the signal yield. Due to these observations, the grooming algorithm of choice for this analysis is pruning, with  $65 \text{ GeV} < m_{pruned} < 105 \text{ GeV}$ . However, this would be a study we would return to in Search II (Section 5.0.8).

The shape tagger we chose for this analysis was the n-subjettiness ratio  $\tau_{21}$ .  $\tau_{21}$  is strongly correlated to the pruned jet mass, and the discriminating power of the variable is reduced when applying a pruned mass cut. The  $\tau_{21}$  distribution for the QCD background and W jets from a signal decay before (left) and after (right) a pruned mass cut of  $65 \text{ GeV} < m_{pruned} < 105 \text{ GeV}$  have been applied, is shown in Figure 5.12.

We therefore perform a cut optimization on  $\tau_{21}$  after all analysis selections, including a

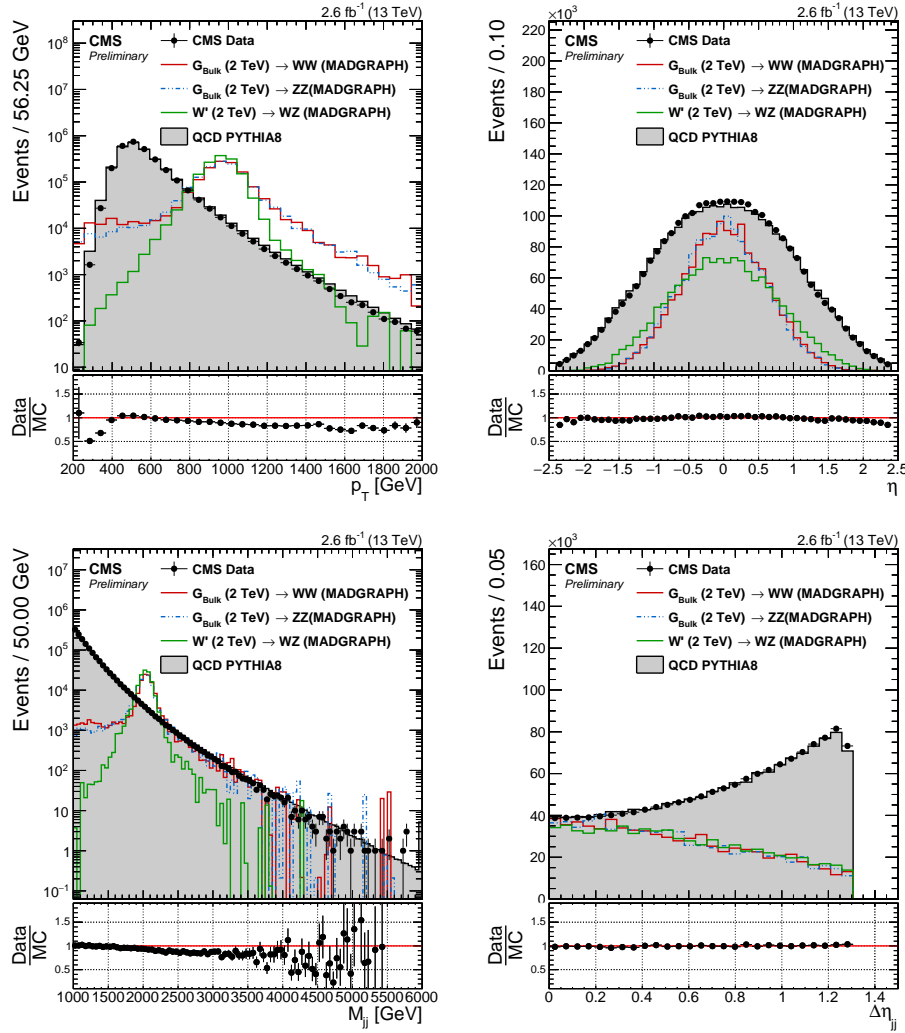


**Figure 5.8:** Jet  $p_T$  (top left),  $\eta$  (top right), dijet invariant mass (bottom left) and  $|\Delta\eta|_{jj}$  (bottom right) distribution for the two leading jets in the event after loose preselections are applied. The signal is scaled by an arbitrary number.

pruned mass window of  $65 \text{ GeV} < m_{\text{pruned}} < 105 \text{ GeV}$ , have been applied. This is done by scanning the  $\tau_{21}$ cut, and for each cut computing the Punzi significance [43] defined as

$$S = \frac{\epsilon_S}{1 + \sqrt{B}}$$

where  $\epsilon_S$  is the signal efficiency and  $B$  is the total background. The cut with the highest significance is defined as the optimal cut value. The signals under consideration are W jets coming from the decay of a  $G_{\text{bulk}}$  with  $M_X = 1 - 4 \text{ TeV}$ , against a background of light flavored QCD jets. Only jets with a dijet invariant mass in a 20% window around the resonance mass are considered. The Punzi significance as a function of the upper cut value on  $\tau_{21}$  is shown on the left in Figure 5.13.

The optimal cut gets looser as the dijet invariant mass increases, something which can be understood when looking at the QCD dijet invariant mass spectrum in Figure 5.8. The number of QCD jets falls off exponentially with  $m_{jj}$ , meaning that the background at 4 TeV is considerably lower than at 1 TeV. This allows for a looser cut on  $\tau_{21}$  as  $m_{jj}$  increases. In order to choose a single cut which works reasonably well for all masspoints, we look at the

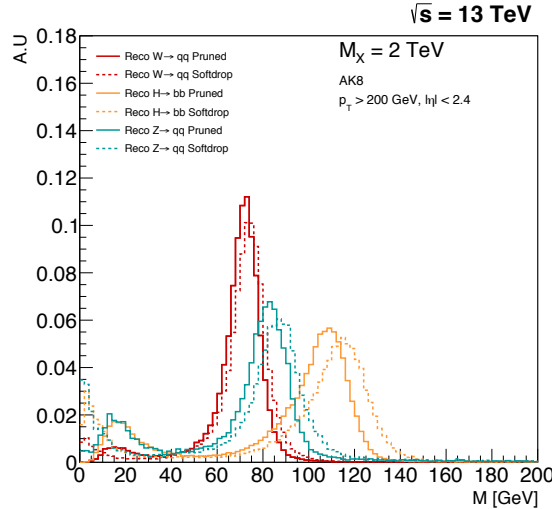


**Figure 5.9:** The softdrop (dotted lines) and the pruned (solid lines) jet mass for W, Z and H jets.

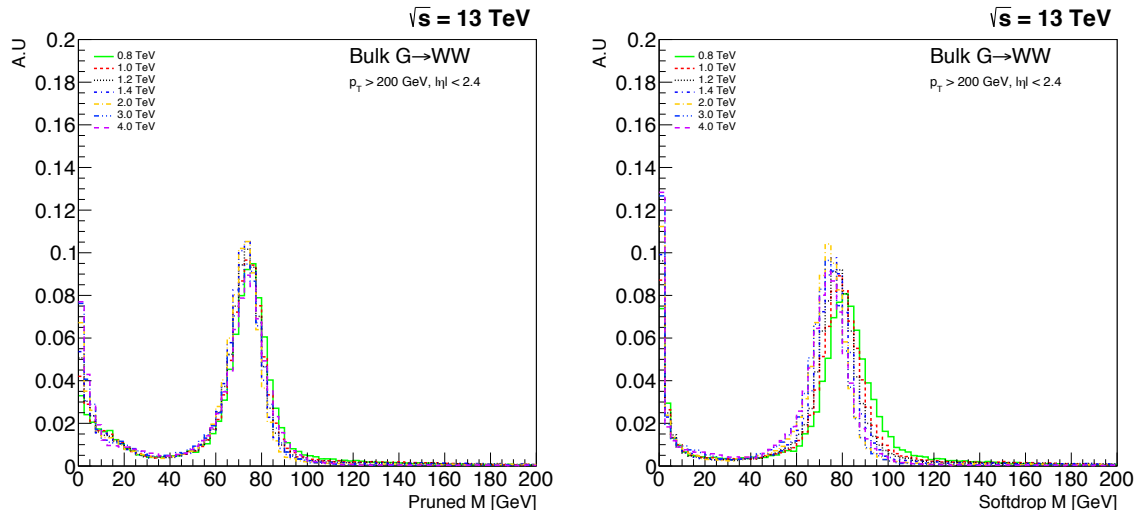


**Figure 5.10:** The jet mass distribution for W jets coming from a  $G_{\text{bulk}}$  of masses in the range  $0.8 \text{ TeV} < M_X < 4 \text{ TeV}$  decaying to WW, here with pruning applied (left) and softdrop (right). A strong shift in the jet mass mean as a function of  $p_T$  ( $\sim M_X/2$ ), is observed for jets groomed with the softdrop algorithm. Charge hadron subtraction is applied to all jets before clustering.

ratio of a given  $\tau_{21}$ cut over the significance of the best cut at that mass points. This is shown in the right plot of Figure 5.13. The cut  $\tau_{21} < 0.45$  has the most stable performance out of the investigated cut values and is due to that, and due to the desire of keeping the background as low as possible at low  $m_{jj}$ , chosen as the nominal cut. In order to account for the fact that background is lower at high- $m_{jj}$ , we add an additional analysis category,  $0.45 < \tau_{21} < 0.75$ , which contains  $> 95\%$  of the signal and enhances the analysis sensitivity where the background is low. These categories are hereafter referred to as the "high purity" (HP) category, for jets with  $0 < \tau_{21} \leq 0.45$ , and the low purity (LP) category, for jets with  $0.45 < \tau_{21} \leq 0.75$ .

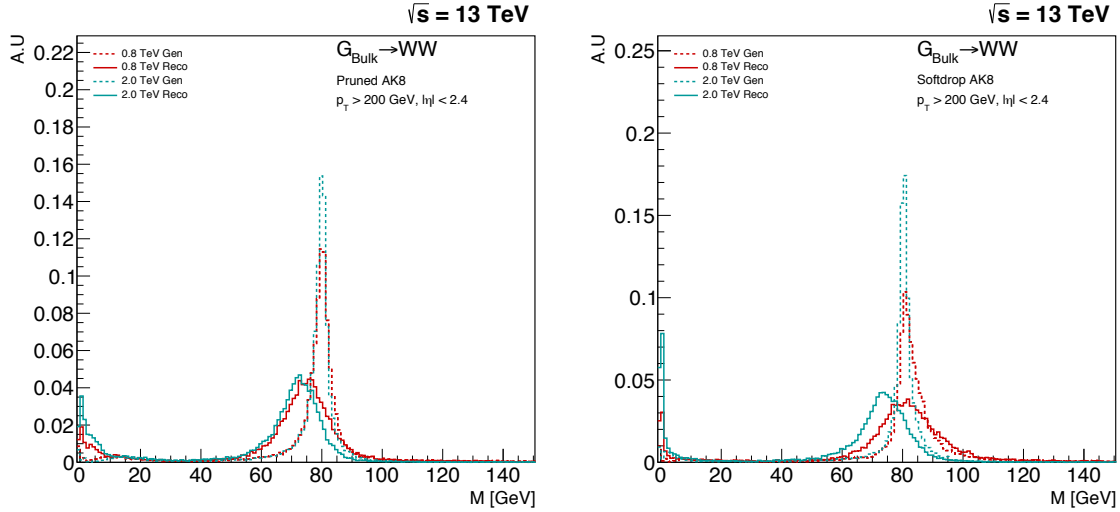


**Figure 5.11:** The reconstructed (solid line) and generator level (dotted line) jet mass distribution for W jets coming from a  $G_{\text{bulk}} \rightarrow WW$  of mass  $M_X = 0.8 \text{ TeV}$  (red), roughly  $p_T \sim 400 \text{ GeV}$ , and  $M_X = 2.0 \text{ TeV}$  (blue),  $p_T \sim 1 \text{ TeV}$ . Here for the pruned (left) and softdrop (right) jet mass.

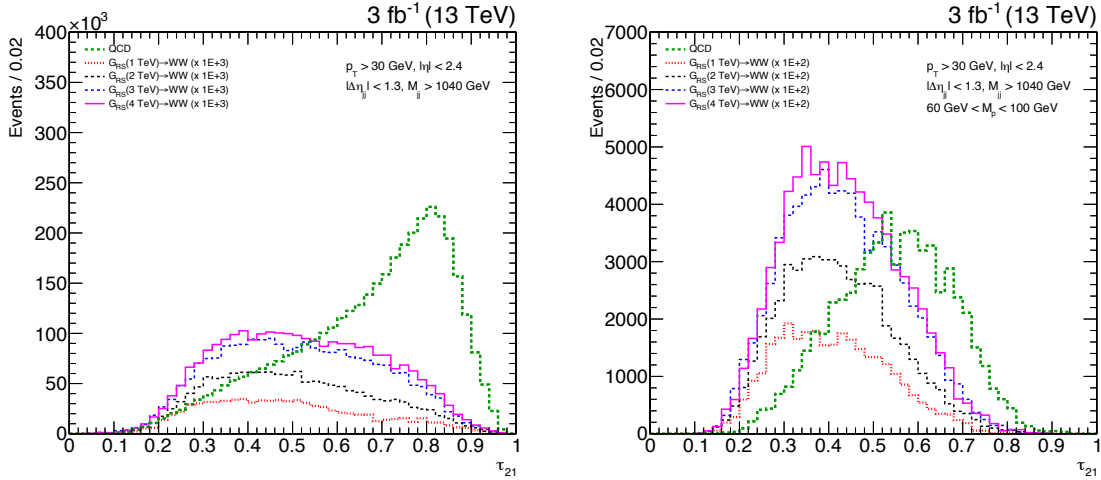


**Figure 5.12:** The  $\tau_{21}$  distribution for QCD background and signal jets before (left) and after (right) a pruned mass window is applied. The discriminating power of  $\tau_{21}$  is strongly reduced after grooming.

The W-tagging efficiency and QCD light-flavored jet mistagging rate for a W-tagger consisting of  $0 < \tau_{21} \leq 0.45$  and  $65 \text{ GeV} < m_{\text{pruned}} < 105 \text{ GeV}$  is shown in Figure 5.14, both as a function of jet  $p_T$  and as a function of number of primary vertices in the event.

The signal efficiency for a pruned jet mass cut only, is around 80 % with a mistag rate of  $\sim 15\%$ . After adding a  $\tau_{21}$  cut, the signal efficiency drops to around 55% and the mistagging rate to  $\sim 2\%$ . Another interesting feature is the dependence of  $\tau_{21}$  on  $p_T$  on pileup, compared to the resilience of the groomed mass as a function of the same variables. This will be another feature we explore in Search II (Section 5.0.8).

Figure 5.15 shows the pruned-jet mass (left) and the n-subjettiness  $\tau_{21}$  distribution (right) for signal and background Monte Carlo, as well as the distributions measured in data.

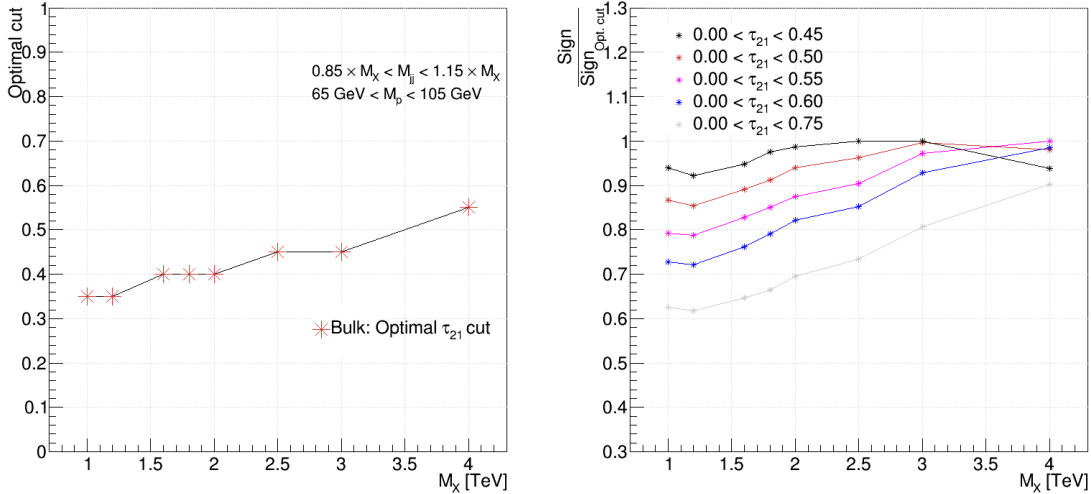


**Figure 5.13:** Optimal upper cut on  $\tau_{21}$  as a function of  $G_{\text{bulk}}$  mass (left). The optimal  $\tau_{21}$  selection for  $W'$  (HTV model) resembles the Bulk graviton selection.

## Analysis categorization

As the analysis requires two W/Z-tags, we always require one HP tagged jet and then divide into LP and HP categories depending on whether the other jet is of high or low purity. In addition, in order to further enhance the analysis sensitivity, we further split the pruned jet mass window into a W and a Z boson window where the W window is defined as  $65 \text{ GeV} < m_{\text{pruned}} < 85 \text{ GeV}$  and the Z boson window as  $85 \text{ GeV} < m_{\text{pruned}} < 105 \text{ GeV}$ . This has the added benefit of allowing us to make a discrimination between a  $G_{\text{bulk}}$  decaying to WW or ZZ, and a  $W'$  decaying into WZ through counting events in each category. We, for instance, expect a higher signal yield in WZ category for a  $W'$  decaying to a W and Z boson than for a  $G_{\text{bulk}}$  decaying to WW or ZZ. Figure 5.16 shows the relative expected signal yield (left) and expected limits (left) in the different mass categories for a 2 TeV  $W'$ .

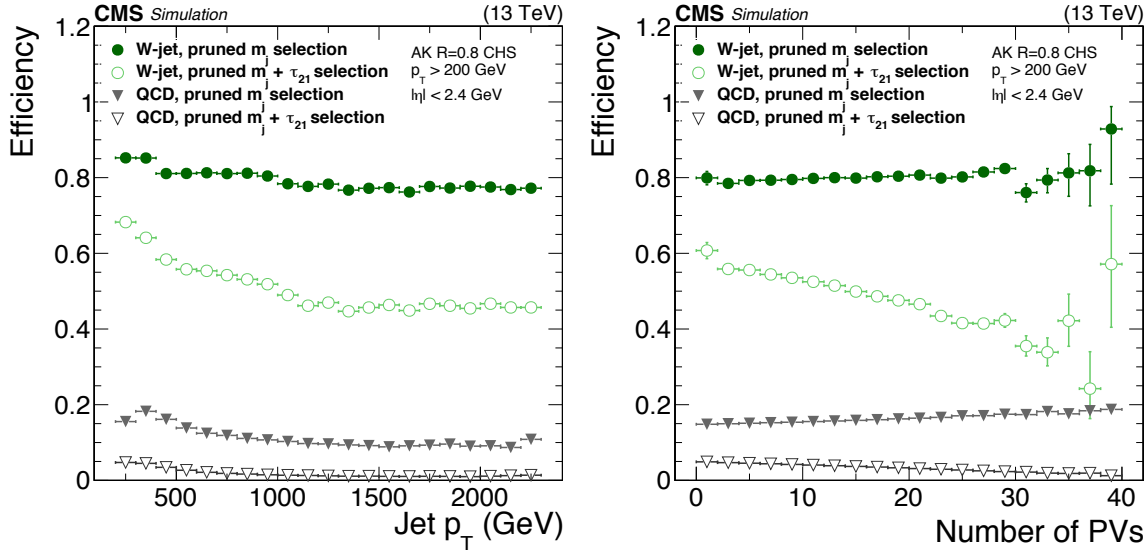
All categories are combined in the end, leading to the same or better sensitivity than when using the whole pruned mass window.

Figure 5.17 shows the expected 95% CL upper limits on the production cross section of a  $W'$  decaying to WZ (left) and a  $G_{\text{bulk}}$  decaying to WW (right) as function of the resonance mass in the HP category. The blue line corresponds to the expected limits obtained when not splitting into mass categories and the red line corresponds to the limit using the combination of two categories. The dotted and solid black lines are the limits in the W and Z categories, respectively. The combination of two mass categories leads to a slightly better (10%) or to the same sensitivity as when using one large mass window.

The real benefit of splitting into mass categories becomes obvious when defining a test statistics based on the likelihood ratios of each signal hypothesis,  $q = -2 \ln(L_{G_{\text{bulk}}} / L_{W'})$ , shown in Figure 5.18. For a signal with a signal strength corresponding to a 3-4  $\sigma$  excess, the test statistics for each signal hypothesis are well separated ( $\sim 3.5\sigma$ ), allowing us to make a statement of how  $G_{\text{bulk}}$  or  $W'$  like a possible signal is.

With the high-purity and low-purity categories as defined above for each mass window combination, this leaves us with six different signal categories. They are as follows:

- High-purity, 3 mass categories: WW, ZZ and WZ



**Figure 5.14:** The W-tagging efficiency (green) and light jet mistag rate (grey) for a pruned jet mass cut only and pruned jet mass +  $\tau_{21}$ cut as a function of  $p_T$  (left) and number of primary vertices (right).

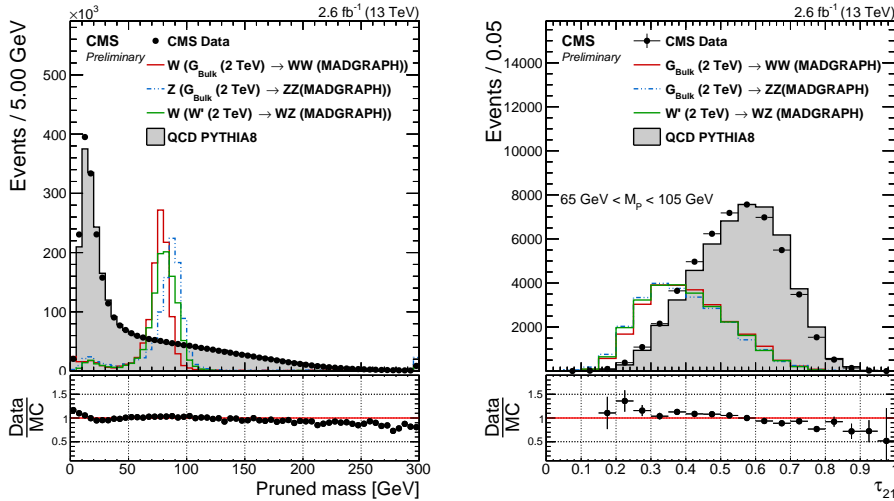


**Figure 5.15:** Pruned jet mass distribution (left) and n-subjettiness  $\tau_{21}$  (right) distribution for data and simulated samples. Simulated samples are scaled to match the distribution in data. The  $\tau_{21}$  distribution is shown for jets after a cut of  $65 \text{ GeV} < M_p < 105 \text{ GeV}$  has been applied.

- Low-purity , 3 mass categories: WW, ZZ and WZ

In parallel to the mass-category based analysis, we perform an analysis without categorization in mass (similar to the 8 TeV analysis) as a cross-check. These studies can be found in the Appendix ??.

The final tagging efficiency for different signal hypothesis (top) together with the QCD mistag rate (bottom) in the different signal categories is shown in Figure 5.19. The solid lines represent the tagging efficiency in the full mass window ( $65 \text{ GeV} < M_p < 105 \text{ GeV}$ ) before splitting into mass categories. A lower signal efficiency the ZZ mass category is observed in all cases. This can be explained from the pruned jet mass distribution on the left in

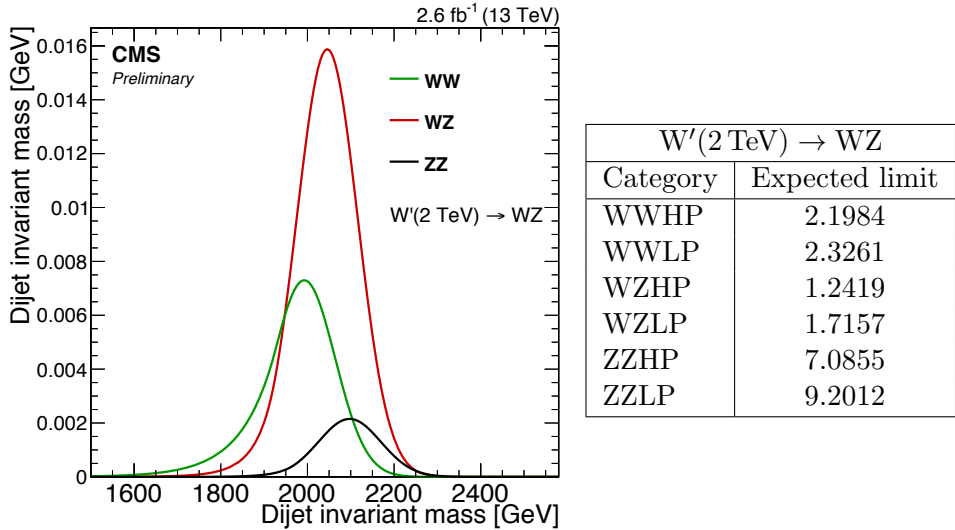


**Figure 5.16:** The expected signal yield per mass category for  $W'$  (2 TeV) decaying to a  $W$  and  $Z$  (left) together with the expected limit per mass category for the same signal (right).

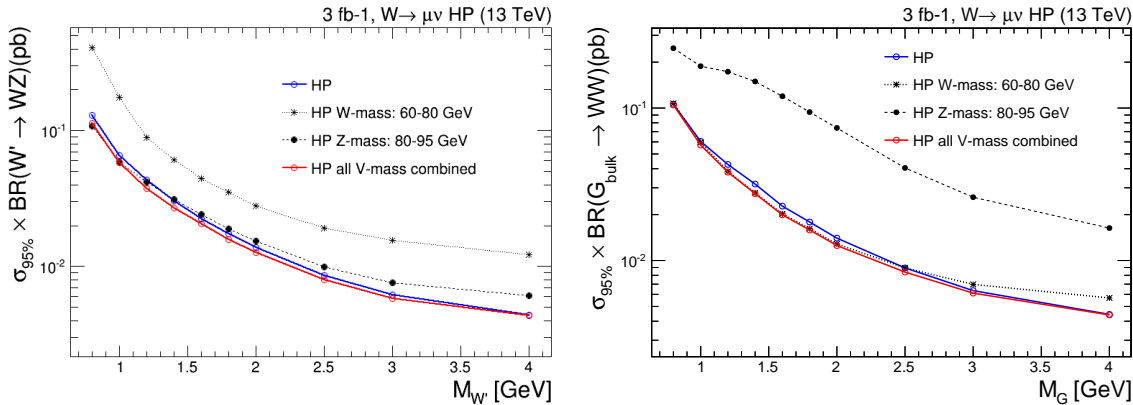


**Figure 5.17:** Expected 95% CL upper limits on the production cross section of a  $W'$  (left) and  $G_{bulk}$  (right) signal as function of the resonance mass for the different mass categories for events passing the high-purity  $\tau_{21}$  selections.

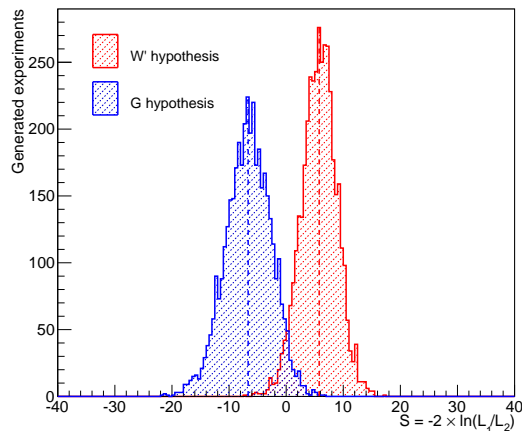


**Figure 5.18:** Distribution of the test statistic  $q = -2 \ln(L_{G_{bulk}}/L_{W'})$  for a  $G_{bulk}$  (blue) and  $W'$  signal hypothesis.

Figure 5.15, where a cut at 85 GeV leaves a large fraction of the Z peak in the W mass window. As the main benchmark models under consideration preferably decays to W bosons (in the Bulk Graviton model the branching ratio  $\text{BR}(G_{\text{Bulk}} \rightarrow WW) = 2 * \text{BR}(G_{\text{Bulk}} \rightarrow ZZ)$ , and in the HVT model  $W'/Z' \rightarrow WZ/WW$  (but not  $ZZ$ )), a high tagging efficiency for the W boson is preferred. In the limit-setting procedure all the categories are combined and the overall signal efficiency is conserved. For the combined mass-categories (solid line) the signal efficiency is between 16 and 23 % in the double-tag categories, and between 20 and 34 % in the single-V tag categories. The mistagging rate in the double-V tag categories is below 1 % in the high-purity category.

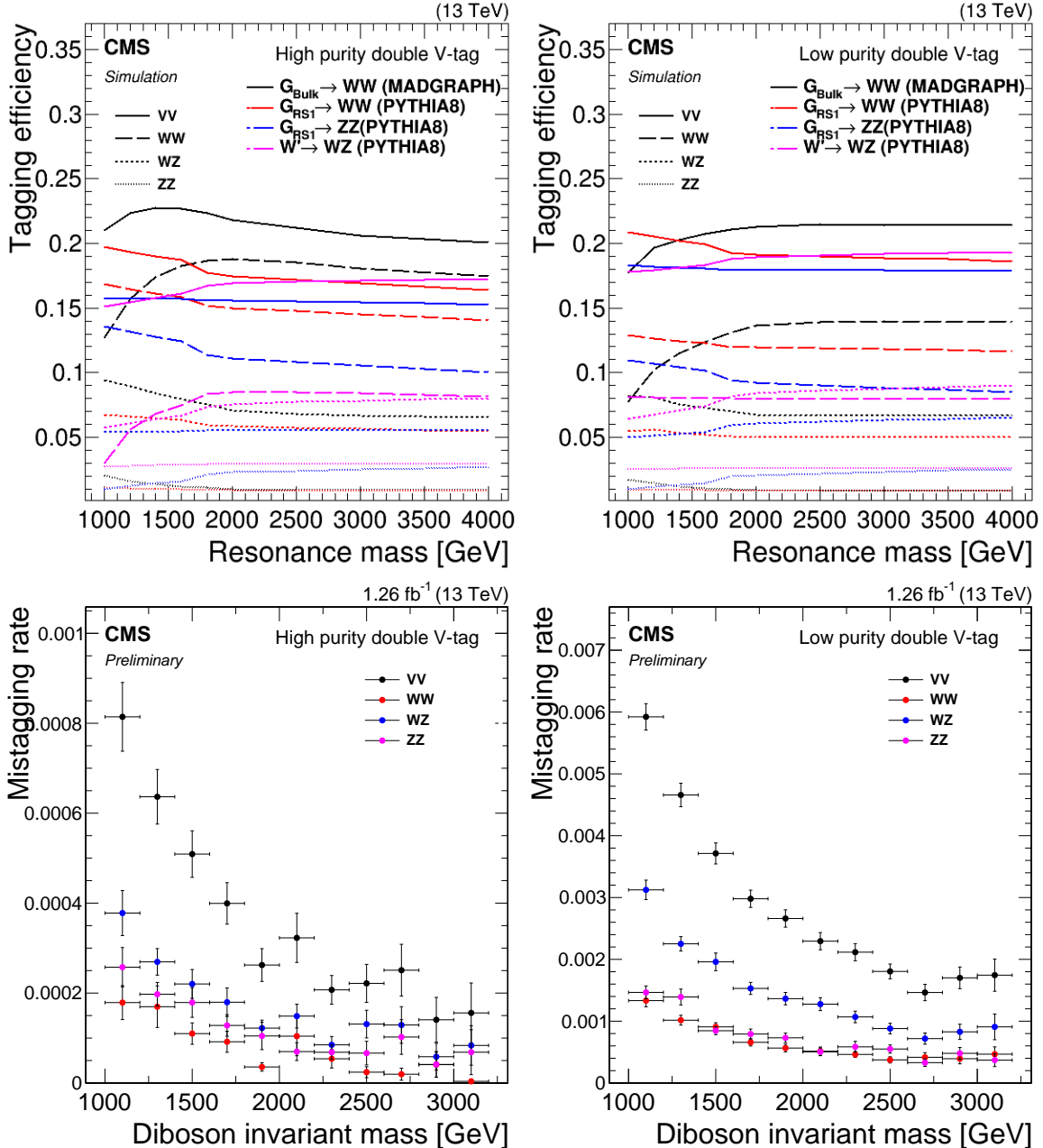


**Figure 5.19:** Tagging efficiency (top) and mistagging rate (bottom) in the different pruned mass categories in the high-purity category (left) and in the low-purity category (right)

The full analysis selections and final categories are listed in Table ??.

Selection	Value
Boson selections	
$V \rightarrow q\bar{q}$ (2 AK8 jets)	$p_T > 200 \text{ GeV}$ $ \eta  < 2.4$
Pruned jet mass	$65 < m_{\text{jet}_1}, m_{\text{jet}_2} < 105 \text{ GeV}$
Topology	$ \Delta\eta_{jj}  < 1.3$
Dijet invariant mass	$m_{jj} > 1 \text{ TeV}$
2- to 1-subjettiness ratio	$\tau_{21} < 0.75$
$m_{\text{jet}}$ categories	
WW	$65 < m_{\text{jet}_1} < 85 \text{ GeV}, 65 < m_{\text{jet}_2} < 85 \text{ GeV}$
WZ	$65 < m_{\text{jet}_1} < 85 \text{ GeV}, 85 < m_{\text{jet}_2} < 105 \text{ GeV}$
ZZ	$85 < m_{\text{jet}_1} < 105 \text{ GeV}, 85 < m_{\text{jet}_2} < 105 \text{ GeV}$
$\tau_{21}$ categories	
High-purity	$\tau_{21,\text{jet}1} < 0.45, \tau_{21,\text{jet}2} < 0.45$
Low-purity	$\tau_{21,\text{jet}1} < 0.45, 0.45 < \tau_{21,\text{jet}2} < 0.75$

**Table 5.1:** The full analysis selections, mass and  $\tau_{21}$  categories.

### 5.0.5 Background modeling

The background modeling in this analysis is based on a smoothness test performed directly on unblinded data, similar to what is done in previous CMS analyses looking for bumps in the dijet invariant mass spectrum [44, 45]. We assume that the QCD multijet background in the different analysis categories can be described by smooth, monotonically decreasing functions of 2 or 3 parameters

$$\frac{dN}{dm_{jj}} = \frac{P_0}{(m_{jj}/\sqrt{s})^{P_2}} \quad \text{and} \quad \frac{dN}{dm_{jj}} = \frac{P_0(1 - m_{jj}/\sqrt{s})^{P_1}}{(m_{jj}/\sqrt{s})^{P_2}} , \quad (5.1)$$

where  $m$  is the dijet invariant mass,  $\sqrt{s}$  the centre of mass energy and  $P_0$  is a normalization parameter for the probability density function and  $P_1$  and  $P_2$  describe the shape. The number of fit parameters is decided through a Fishers F-test [46]. In this test, we start from the 2 parameter function and compare the goodness of fit ( $\chi^2$  divided by degrees of freedom) when fitting the data signal region with a 2, 3, 4 and 5 parameter function. We then check at 10% confidence level (CL) if additional parameters are needed to model the background distribution. The 4 and 5 parameter functions are

$$\frac{dN}{dm_{jj}} = \frac{P_0(1 - m_{jj}/\sqrt{s})^{P_1}}{(m_{jj}/\sqrt{s})^{P_2 + P_3 \times \log(m_{jj}/\sqrt{s})}} \quad (5.2)$$

$$\frac{dN}{dm_{jj}} = \frac{P_0(1 - m_{jj}/\sqrt{s})^{P_1}}{(m_{jj}/\sqrt{s})^{P_2 + P_3 \times \log(m_{jj}/\sqrt{s}) + P_4 \times \log(m_{jj}/\sqrt{s})^2}} \quad (5.3)$$

where  $P_3$  and  $P_4$  are additional free parameters. As an additional cross check, an alternative fit function is also tested:

$$\frac{dN}{dm_{jj}} = \frac{P_0(1 - m_{jj}/\sqrt{s} + P_3(m_{jj}/\sqrt{s})^2)^{P_1}}{(m_{jj}/\sqrt{s})^{P_2}} . \quad (5.4)$$

The fit range is chosen such that it start where the trigger efficiency has reached its plateau to avoid bias from trigger inefficiency, and extends to the bin after the highest  $m_{VV}$  mass point. The binning chosen for the fit follows the detector resolution as in [44, 45]. Before unblinding the signal region, we check that the QCD dijet invariant mass spectrum is expected to be smooth from the distribution in QCD MC as well as exercise the F-test in QCD MC and in a data sideband.

The fits to data in the signal region using the different fit functions, are shown in Figure 5.21, and the corresponding F-test output are given in Table 5.2 through Table 5.4. The findings can be summarized as follows: for the WW enriched category a 2 parameter fit is sufficient to describe the data in both the high- and low-purity categories. In the WZ category, a two parameter fit is sufficient in the high-purity category, while three parameters are needed for the low-purity category. For the ZZ category, a 3 parameter fit is needed for both purity categories. The 2 and 3 parameters fit functions as defined in Equation 5.2 will therefore be used to model the background component in the simultaneous signal and background fit.

WW enriched, HP				WW enriched, LP			
Function	Residuals	$\chi^2$	ndof	Function	Residuals	$\chi^2$	ndof
2 par	0.034	9.279	11	2 par	0.270	13.462	17
3 par	0.034	9.160	10	3 par	0.300	13.819	16
4 par	0.040	8.030	9	4 par	0.324	13.680	15
Fishers23	-0.053	CL	1.0	Fishers23	-1.723	CL	1.0
Fishers34	-1.456	CL	1.0	Fishers34	-1.191	CL	1.0

**Table 5.2:** Residuals,  $\chi^2$ , and degrees of freedom for the WW enriched HP and LP categories. A 2 parameter fit is needed to describe the data in both categories.

WZ enriched, HP				WZ enriched, LP			
Function	Residuals	$\chi^2$	ndof	Function	Residuals	$\chi^2$	ndof
2 par	0.039	9.105	16	2 par	1.016	17.602	20
3 par	0.047	7.915	15	3 par	0.270	11.424	19
4 par	0.048	8.370	14	4 par	0.269	11.421	18
Fishers23	-2.598	CL	1.0	Fishers23	55.258	CL	0.0
Fishers34	-0.491	CL	1.0	Fishers34	0.078	CL	0.783

**Table 5.3:** Residuals,  $\chi^2$ , and degrees of freedom for the WZ enriched HP (left) and LP (right) categories. A 2 parameter fit is sufficient to describe the data in the high-purity category, while three parameters are needed for the low-purity category.

ZZ enriched, HP				ZZ enriched, LP			
Function	Residuals	$\chi^2$	ndof	Function	Residuals	$\chi^2$	ndof
2 par	0.220	9.901	11	2 par	0.448	18.832	15
3 par	0.140	9.511	10	3 par	0.121	17.463	14
4 par	0.124	9.781	9	4 par	0.118	17.394	13
Fishers23	6.302	CL	0.029	Fishers23	40.438	CL	0.0
Fishers34	1.246	CL	0.290	Fishers34	0.356	CL	0.56

**Table 5.4:** Residuals,  $\chi^2$ , and degrees of freedom for the ZZ enriched LP and HP categories. A 3 parameter fit is sufficient to describe the data in both categories.

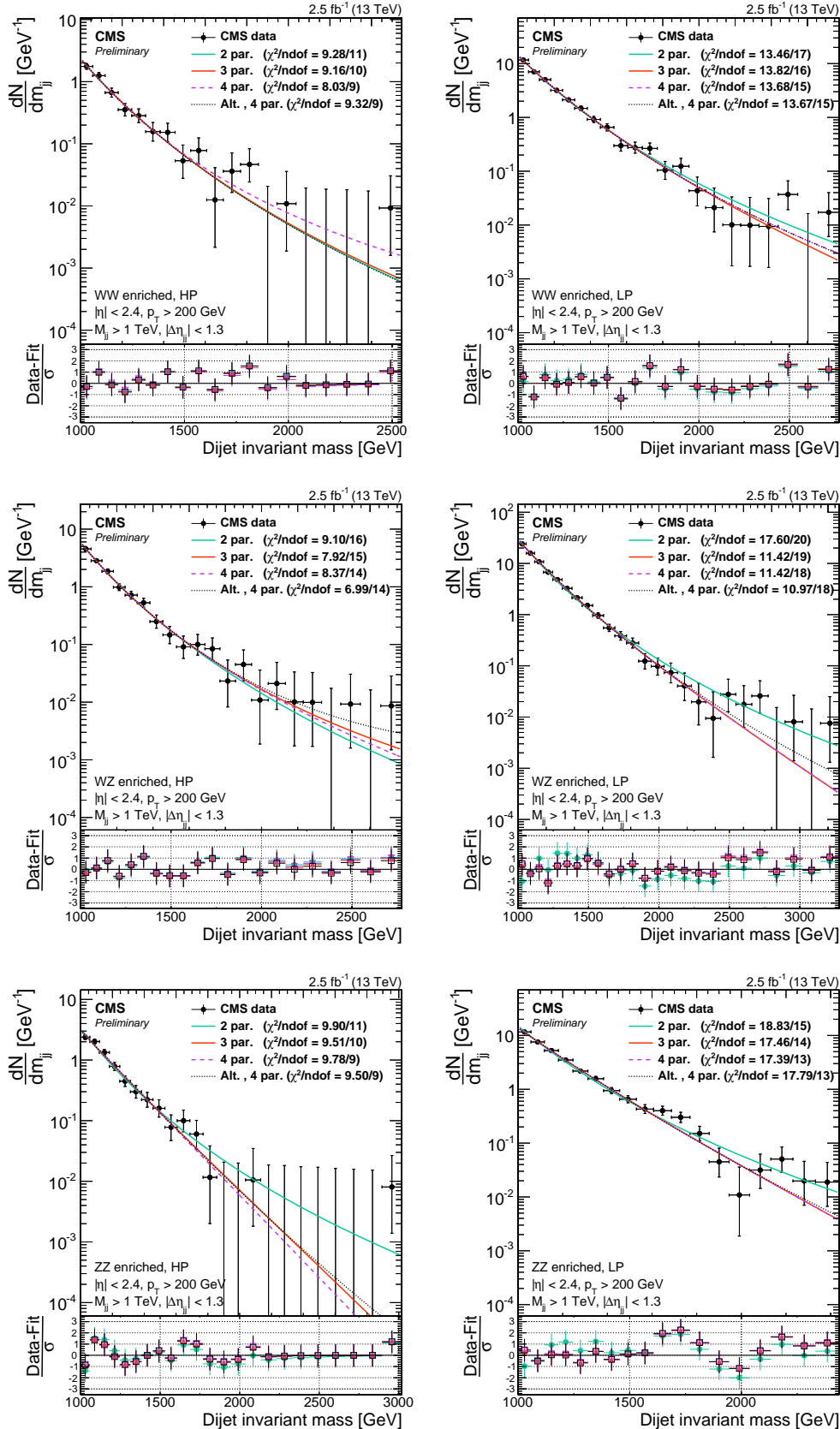


**Figure 5.20:** Fitted dijet mass spectrum in the different mass and purity categories in data for the double V-tag category. A 2 parameter fit is sufficient to describe the data for the WW (HP and LP) and WZ (LP) enriched categories. For the ZZ enriched (HP and LP) and WZ (HP) categories, a 3 parameter fit is needed.

### 5.0.6 Signal modeling

The signal shape is extracted from signal MC with masses in the range from 1 to 4 TeV. A linear interpolation provides shapes for the mass points in between in steps of 100 GeV. From these shapes, pdf models are constructed as composite models with a Gaussian core due to detector resolution and an exponential tail to account for parton distribution function effects. Parametric shape uncertainties due to jet energy scale and resolution uncertainties are inserted by variations of the Gaussian peak position and width. The dijet invariant mass shape for different benchmark model signals are shown in Figure ???. The signal and background components are then simultaneously fitted to the data points.

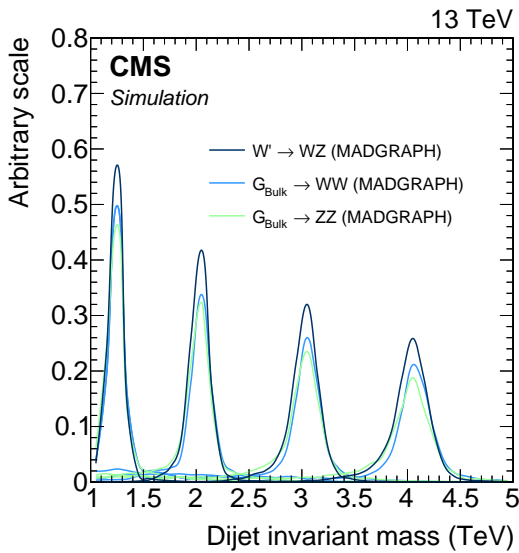


**Figure 5.21:** Dijet invariant mass from signal MC used to extract the signal shape. Here for 1.2, 2, 3 and 4 TeV resonances.

### 5.0.7 Systematic uncertainties

TODO!!

### 5.0.8 Results

The background fits for each analysis category in the data signal region are shown in Figure 5.22. Here a background only fit is performed while, as described above, a simultaneous fit is used for the limit setting procedure. The filled area correspond to the 1 sigma error band of the background fit, obtained using linear error propagation.

We proceed by setting limits on the cross section of the process  $X \rightarrow VV$ , using the asymptotic CL<sub>S</sub> method as described in Section 2.1. The binned likelihood is defined as

$$L = \prod_i \frac{\mu_i^{n_i} e^{-\mu_i}}{n_i!} \quad (5.5)$$

with

$$\mu_i = \sigma \cdot N_i(S) + N_i(B) \quad (5.6)$$

Here  $\sigma$  is the signal strength scaling the expected number of signal events in the  $i$ -th dijet invariant mass bin  $N_i(S)$ ,  $N_i(B)$  is the expected number of background events in dijet invariant mass bin  $i$  and  $n_i$  is the observed number of events in the  $i$ th dijet invariant mass bin. The background per bin  $N_i(B)$  is estimated from the background component of the best signal+background fit to the data points with the signal cross section set to zero. The number of signal events in the  $i$ -th dijet invariant mass bin,  $N_i(S)$ , is then estimated from the signal templates, where only a dijet invariant mass in a 20% window around the resonance mass is considered, containing most of the signal contribution while making sure to keep a good description of the core.

As mentioned in Section 5.0.3, we set limits on three different signal scenarios:  $G_{\text{bulk}} \rightarrow WW$ ,  $G_{\text{bulk}} \rightarrow ZZ$  and  $W' \rightarrow WZ$ . Figure 5.23 shows the asymptotic limits and corresponding p-values obtained with  $2.6 \text{ fb}^{-1}$  of 13 TeV CMS data after combining all mass and purity categories.

The statistics are too low to exclude the excess around 2 TeV observed in the corresponding Run 1 analysis and in addition an under-fluctuation in data is present in this region. The largest excess is observed for a  $G_{\text{bulk}} \rightarrow ZZ$  hypothesis at a resonance mass of 2.8-3 TeV, around  $2.3\sigma$ . This is driven by the ZZ high-purity category, the category with the lowest statistics, where one event at 3 TeV yields a local significance of  $2.8\sigma$ . A 3 parameter fit is the default background fit function for this category, however, a 2 parameter fit could also be used to describe these data. In Figure 5.24 we compare the limits and p-values obtained using a 2 parameter and a 3 parameter fit to describe the background in this category. The significance at 3 TeV is reduced from  $2.8$  to  $1.5\sigma$  with a 2 parameter fit, reflecting the fact that the fit is poorly constrained in the high mass tail due to low statistics. The fit to data using both a 2 and 3 parameter fit in the ZZHP category is shown in Figure 5.25 and we in addition see that the 2 parameter fit lies within the fit uncertainties of the nominal fit.

The lack of constraint on the fit in the dijet invariant mass tail when statistics are very low, is a drawback of a method relying fully on a parametric fit and reduces the analysis sensitivity in the high- $m_{jj}$ region. In Search II (Section 5.0.8) we will keep taking advantage of the dijet fit, however, the integrated luminosity is  $\sim 15$  times higher, resulting in more datapoints in the  $m_{jj}$ tail which further constrains the fit. In Search III (Section 5.1), we will explore alternate methods which allow more control over the background shape across the full mass spectrum.

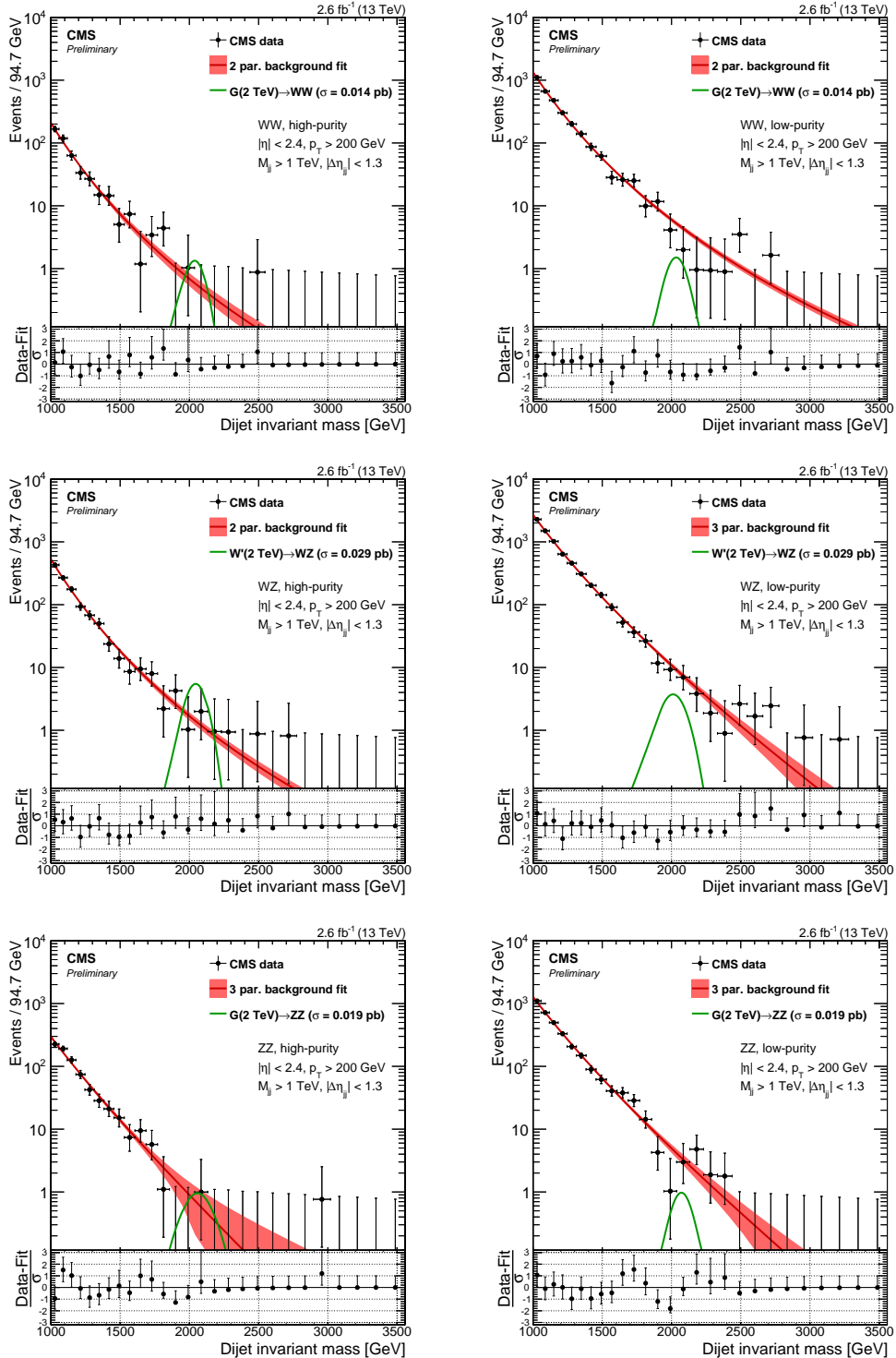


**Figure 5.22:** Fit to data in the signal region using the background fit only for the different mass and purity categories. The filled red area correspond to the 1 sigma statistical error of the fit.

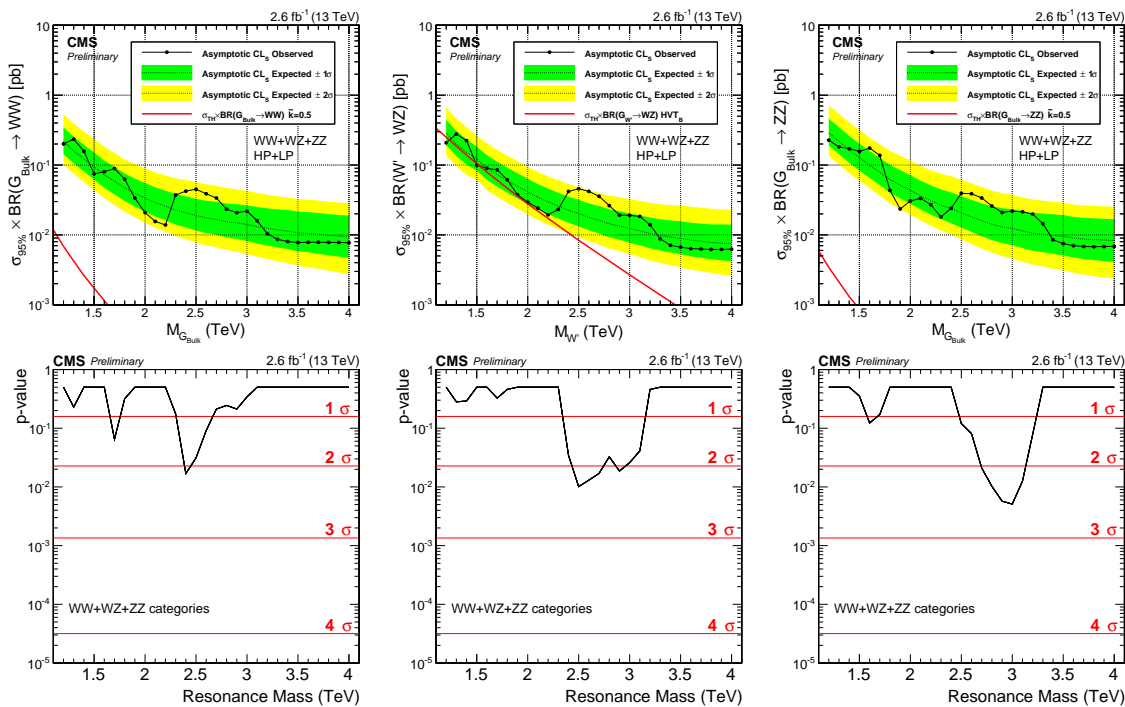


**Figure 5.23:** Expected and observed limits with corresponding p-values obtained using  $2.6 \text{ fb}^{-1}$  of CMS data after combining all mass and purity categories. Here for a Bulk  $G \rightarrow \text{WW}$  (left),  $W' \rightarrow \text{WZ}$  (middle) and  $G \rightarrow \text{ZZ}$  (right) signal.

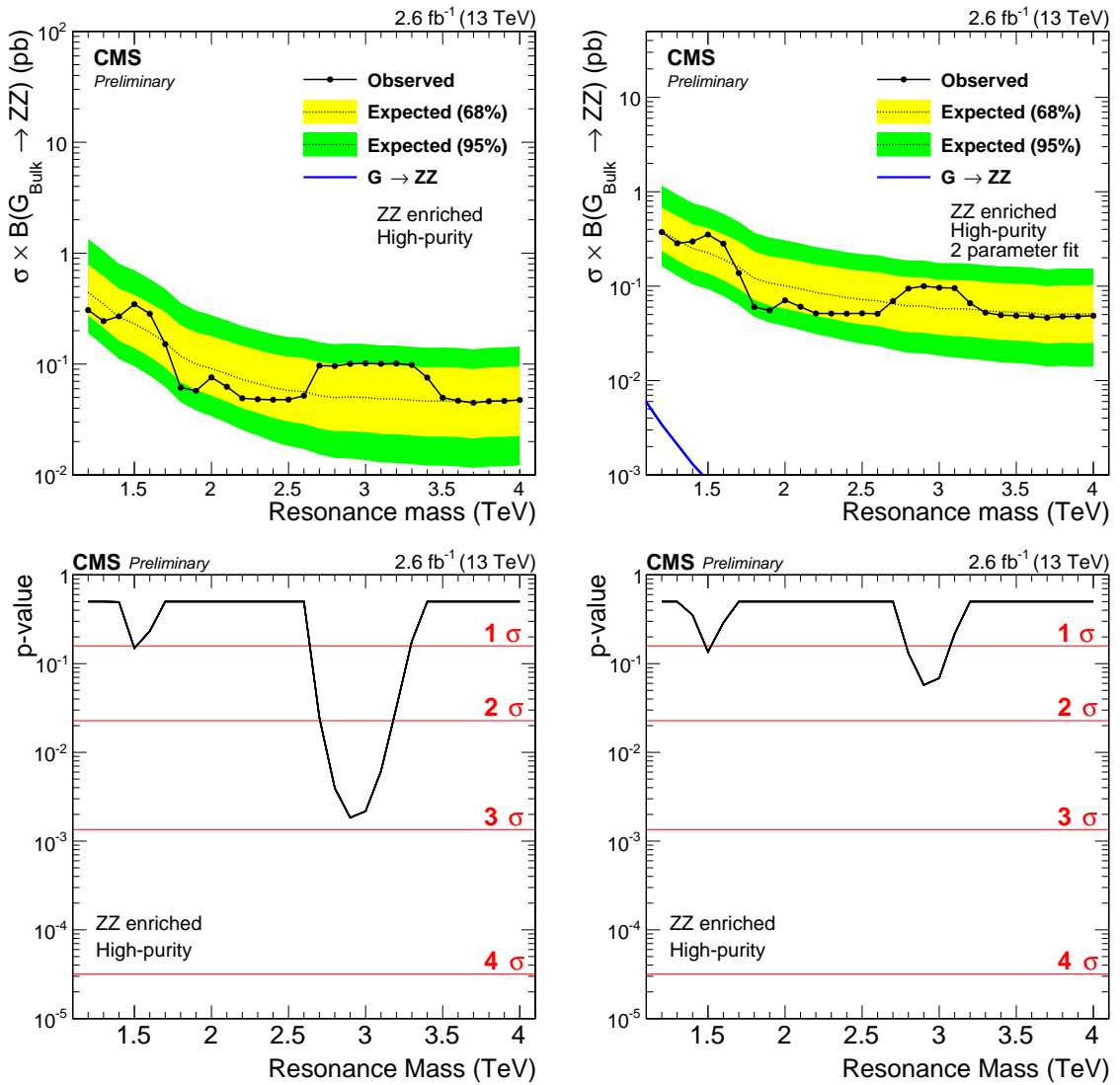


**Figure 5.24:** Expected/observed limits and corresponding p-values obtained in the ZZHP category using a 3 (left) and two (right) parameter fit to describe the background. The significance at 3 TeV is reduced from 2.8 to 1.5  $\sigma$ .

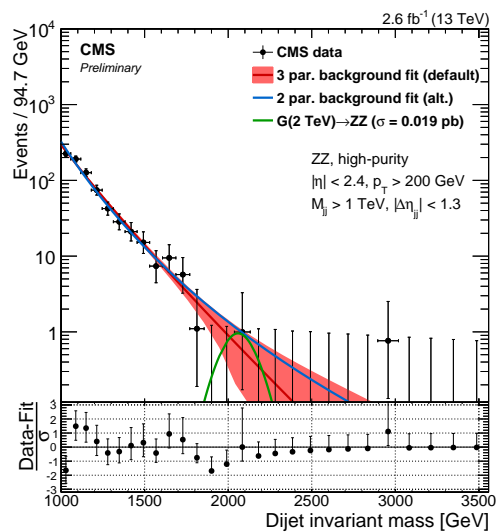


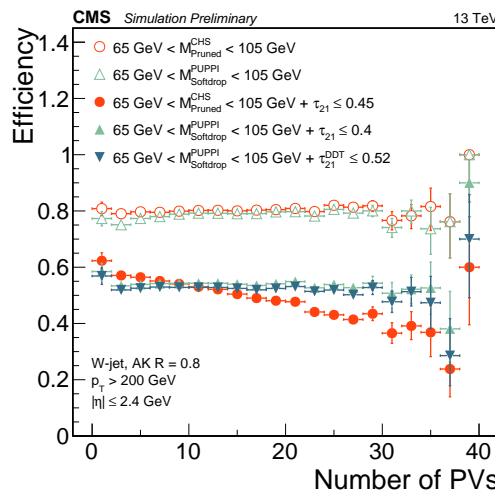
**Figure 5.25:** Background fit to data in the ZZHP category using the default 3 (red) and an alternate 2 (blue) parameter fit to describe the background.

## Search II: A new pileup resistant and perturbative safe tagger

With the first 13 TeV diboson resonance search published, we could conclude that more data would be needed in order to fully exclude the observed Run 1 excess. Luckily, 2016 was right around the corner and, with the LHC planning to reduce  $\beta^*$  from 80 cm to 40, the machine was expected to deliver an instantaneous luminosity three times that of the 2015 peak luminosity. Higher instantaneous luminosity, however, meant double the pileup.

We knew that a novel pileup subtraction algorithm had been developed, which provided far better pileup and underlying event rejection than the current default (CHS). We also knew that there had been made progress on the theory side in the development of a groomer which was insensitive to the soft divergences of QCD and allowed to accomplish jet grooming in a theoretically calculable way, SoftDrop (mMDT). With more time at hand than in 2015, I therefore decided to pursue a novel W-tagger for this second search. This included work like optimization, development of dedicated jet mass corrections (in use today and recommended by the jet physics object group) as well as validation of the new tagger. The tagger, as well as the mass corrections, afterwards became the default W-tagging algorithm in CMS.

Search II became the first published analysis to use the novel PUPPI+softdrop algorithm, now default for W-tagging in CMS. Through this search, the tagger was optimized, commissioned and validated, making it available for several analysis to come. In addition, the search was extended to setting limits on three additional signal hypothesis. Two of these were in a final state never before explored at 13 TeV, the  $q^* \rightarrow qV$  single V-tag analyses.



### 5.0.9 Towards robust boosted jet tagging

When we first studied W-tagging at 13 TeV in context with the analysis of the 2015 dataset, Section 5.0.14, two interesting correlations were observed:

- 1) A strong dependence of the AK8 CHS softdrop ( $\beta = 0$ ) jet mass on jet  $p_T$  and
- 2) a strong dependence of the AK8 CHS  $\tau_{21}$  cut efficiency on pileup.

The reason we studied the softdrop algorithm as an alternative to pruning in 2015 was, besides the possibility it would result in a higher signal efficiency, that we knew it had certain favorable qualities compared to other groomers: Softdrop removes all sensitivity to the soft divergences of QCD, by removing all soft emission, more specifically the non-global logarithmic terms (NGLs) in the jet mass [22]. These arise from constellations where, for instance, a soft gluon is radiated into the jet cone, as illustrated in Figure 5.26.

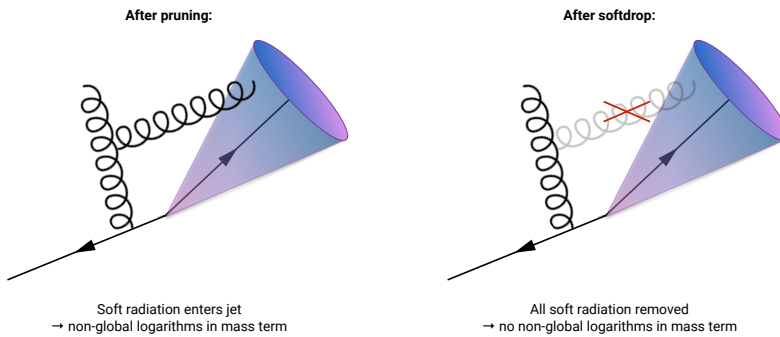


**Figure 5.26:** The pruning algorithm does not remove all soft emission and therefore has non-global logarithmic terms in the jet mass. Softdrop ( $\beta = 0$ ) completely removes soft emissions and is therefore free of non-global logarithms.

The consequence of this is that you can calculate the softdrop jet mass to way higher precision than what is possible for other grooming algorithms or for the plain jet mass (NGLs are the main reason a full resummation of the plain jet mass beyond NLL (considering e.g multiple-emission effects) accuracy does not exist). Despite this not being a precision measurement analysis, we had theoretically well-motivated reasons for wanting the baseline CMS V-tagger to be softdrop-based. However, despite being less sensitive to soft radiation for QCD jets, signal jets groomed with softdrop were found to be far more sensitive to the underlying event than pruned jets [47]. Figure 5.27 shows the signal efficiency for pruning (left) and softdrop (right) as a function of jet transverse momenta when including FSR only, FSR+ISR, hadronization and hadronization + underlying event.

On parton level, as well as after hadronization, the two algorithms perform very similar as a function of  $p_T$ . However, once UE contamination is added, the softdrop tagging efficiency is severely affected. This can be explained by the larger effective radius considered by the softdrop algorithm ( $\propto m_V/p_T \sqrt{z_{cut}(1-z_{cut})}$ ) in comparison to pruning ( $\propto m_V/p_T$ ). This observation corresponds very well with the shift in jet mass we observed for softdrop as a function of  $p_T$  in Section 5.0.14: As the jet  $p_T$  decreases the softdrop effective radius increases and the jet mass mean shifts to higher values, due to absorbing more background radiation. If softdrop would be our new default tagger, a better rejection of pileup and UE contamination would be needed. In parallel to the ongoing theoretical work on groomers, a novel pileup removal algorithm had been proposed: Pileup per particle identification (PUPPI) [16]. Described in detail in Section 4.3.2, PUPPI considers not only charged pileup but rather reweights each particle in the jet with its probability of arising from pileup. PUPPI

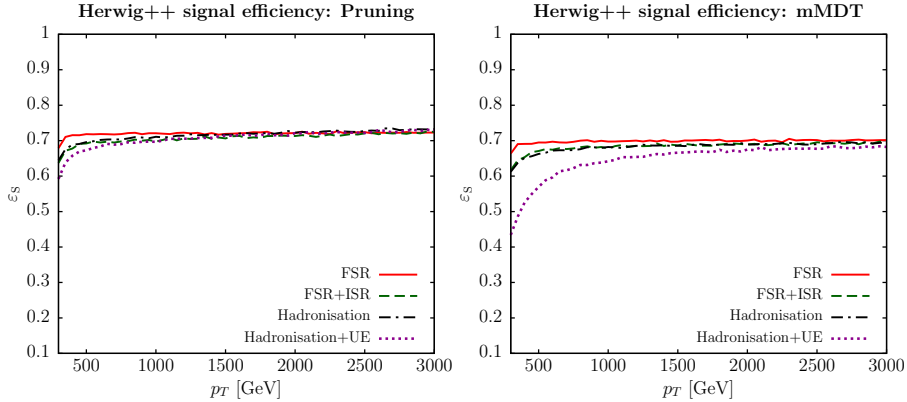


**Figure 5.27:** The signal efficiency for pruning (left) and softdrop (right) as a function of jet  $p_T$  when adding FSR, ISR, hadronization and UE. The UE has a severe impact on the softdrop efficiency for signal jets [47].

had proven it self far superior to the current CHS algorithm in terms of jet observables for large radius jets, and therefore seemed like the obvious choice to address both issues listed above: The sensitivity of softdrop regarding UE contamination and the strong pileup dependence of  $\tau_{21}$ . The focus of Search II would therefore be on the commissioning of a novel W-tagger. There are interesting changes and inclusions in the analysis strategy as well: The inclusion of a  $Z' \rightarrow WW$  signal hypothesis and the addition of a completely new analysis, the single V-tag analysis.

### 5.0.10 Analysis strategy

The analysis strategy for this search is conceptually the same as for Search I. In addition, we'll take advantage of the n-subjettiness categorization and do an additional analysis in parallel: A search for excited quark resonances  $q^*$  [48, 49] decaying to  $qW$  or  $qZ$ . We call this the single V-tag analysis, and the analysis selection only differs in that one jet is not required to pass the V-tag selection (groomed mass and n-subjettiness). The VV analysis is hereby referred to as the double V-tag analysis. The difference between the two analyses is illustrated in Figure 5.28.

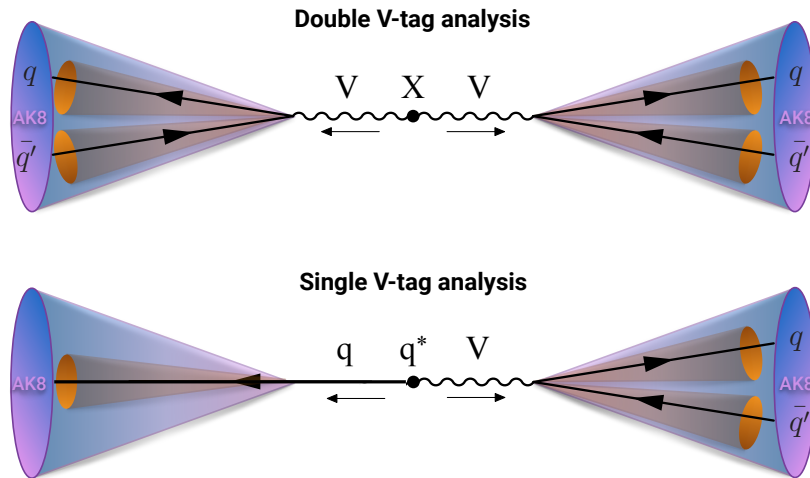


**Figure 5.28:** The double (top) and single (bottom) W/Z-tag analysis.

In addition, limits are set on a  $Z' \rightarrow WW$  signal hypothesis in the double V-tag analysis, another 13 TeV first.

This analysis was published in two steps: An early Physics Analysis Summary (PAS) based on  $12.9 \text{ fb}^{-1}$  of 2016 data [50], describing the new PUPPI+softdrop based V-tagger as well as the single V-tag analysis, and a second analysis topping up with the full 2016 data [51]. The commissioning of the new W Z-tagger has also been documented in a jet performance Physics Analysis Summary [52]. As the new V-tagger was developed and commissioned in the context of the early analysis, which was also where the single V-tag analysis was first published with 13 TeV data, the main emphasis will be on the work presented in CMS-PAS-B2G-16-021 [50]. The second part of the results chapter, Section ??, includes the results obtained using the full 2016 dataset of  $35.9 \text{ fb}^{-1}$ .

### 5.0.11 Data and simulated samples

As mentioned above, the analysis of the 2016 dataset was done in two steps: One based on  $12.9 \text{ fb}^{-1}$  of early 2016 data describing the new W-tagger and single V-tag category, and a second topping up with the full 2016 dataset, corresponding to  $35.9 \text{ fb}^{-1}$ .

The  $G_{\text{bulk}}$  and HVT signal samples are modeled in precisely the same way as in 2015. For the single V-tag  $q^*$  samples, we simulate unpolarized boson with a compositeness scale  $\Lambda$  set equal to the resonance mass. These are generated to leading order using PYTHIA version 8.212 [40].

The background Standard Model processes; QCD,  $W+jets$  and  $Z+jets$  are all simulated to leading order.  $V+jets$  is simulated with MADGRAPH5\_AMC@NLO [39, 53], while three different combinations of matrix element and shower generators is used for QCD as these predictions are known to differ: PYTHIA only, the leading order mode of MADGRAPH5\_AMC@NLO matched with PYTHIA, and HERWIG++ 2.7.1 [29] with tune CUETHS1 [36].

### 5.0.12 Event selection

#### Triggering

The triggers used in this analysis are the same ones as in 2015 (see Section 5.0.4), however, due to the new single V-tag analysis, the trigger turn-ons have this time been re-evaluated separately requiring either one or two jets to have an offline softdrop jet mass above 65 GeV.

Figure 5.29 shows the trigger turn-on curves as a function of dijet invariant mass for jets passing one of the three inclusive triggers only, one of the grooming triggers only and when combining all of them. The turn-on curves are shown for all jet pairs passing loose selections as described in Section 5.0.4. Zero, one or two of the two jets is further required to have a softdrop mass larger than 65 GeV.

Including grooming triggers lowers the 99% trigger efficiency threshold by around 50(80) GeV in the single (double) tag category once substructure is requested on the analysis level. Using the or of all triggers, we are safely on the trigger plateau for dijet invariant masses above 955(986) GeV in the double (single) tag category, setting the analysis threshold at a dijet invariant mass of 955 GeV for the double tag analysis and 990 GeV for the single tag analysis. For controlplots, where no groomed mass window is applied, a trigger threshold of 1020 GeV is used.

Trigger efficiencies as a function of the offline softdrop-jet mass for the `HLT_AK8PFJet360_TrimMass30` trigger are shown in Figure 5.30. Here the jet transverse momentum of one of the jets is required to be at least 600 GeV and no other mass cut is

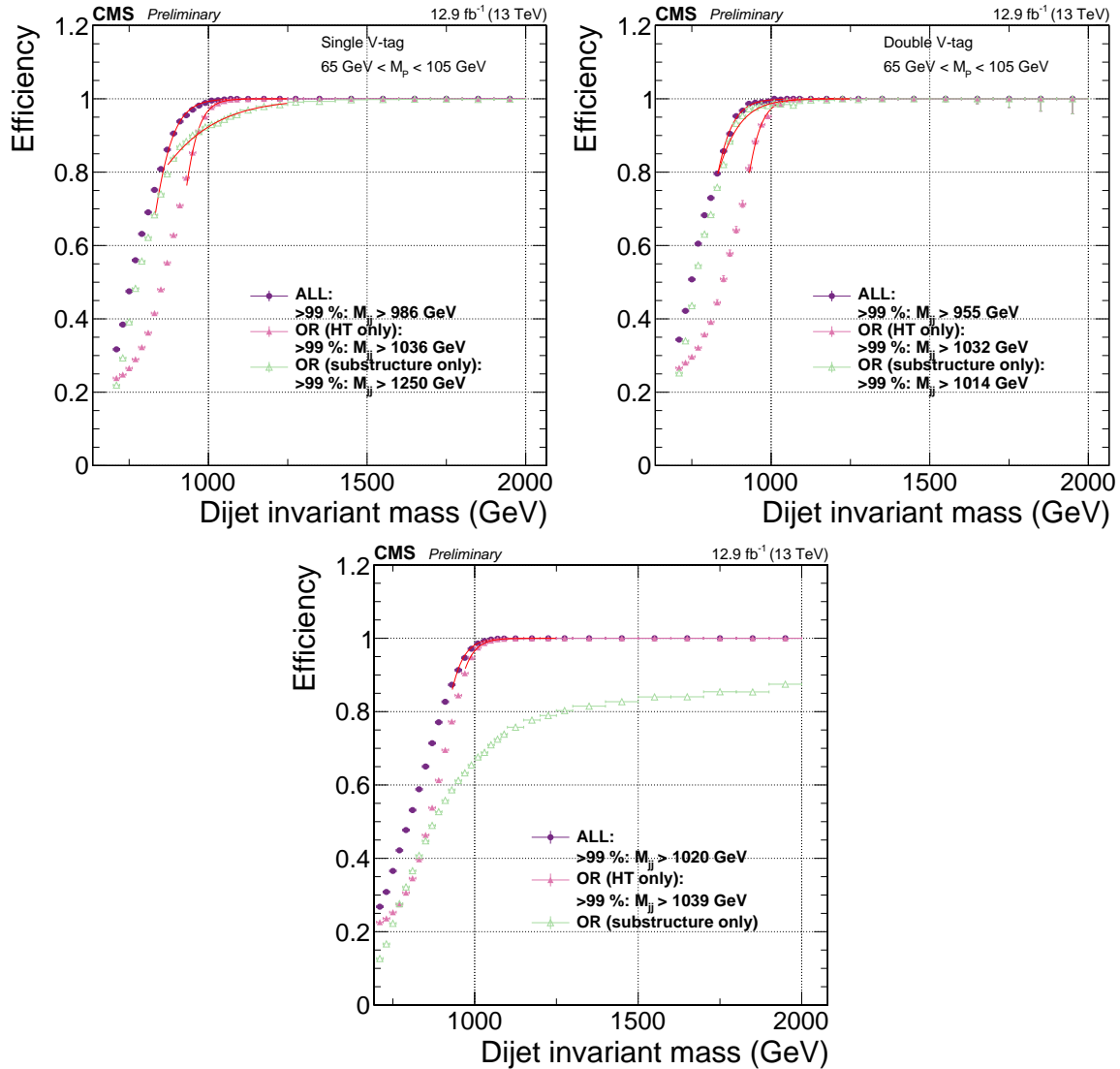


**Figure 5.29:** Comparison of trigger efficiencies for jets passing one of the HT-triggers only (pink), for jets passing one of the grooming-triggers only (green) and for jets passing one of the HT-triggers or one of the grooming triggers (purple). Here as a function of dijet invariant mass for all jet pairs passing loose selections and where one jet has a softdrop mass larger than 65 GeV (top left), both jets have a softdrop mass larger than 65 GeV (top right) and where no mass cut is applied (bottom).

applied. This trigger requires one jet to have a trimmed mass above 30 GeV at HLT level and reaches the trigger plateau for groomed-jet masses around 50 GeV. As reference trigger, the prescaled trigger `HLT_PFTJet320` is used.

## Preselection

The same preselections as in Search I, described in , have been applied: We require two AK R=0.8 jets with CHS applied pre-clustering, required to pass the tight jet ID requirement,  $p_T > 200 \text{ GeV}$  and  $|\eta| < 2.5$ . The same QCD t-channel suppressing cut of  $|\Delta\eta| < 1.3$  is required together with the following trigger thresholds on the dijet invariant mass:  $m_{jj} > 955 \text{ GeV}$  for the double V-tag and  $990 \text{ GeV}$  for the single V-tag analysis. The jet  $p_T$  (top left),  $\eta$  (top right),  $\Delta\eta_{jj}$  and dijet invariant mass (bottom left) for the two leading jets in the

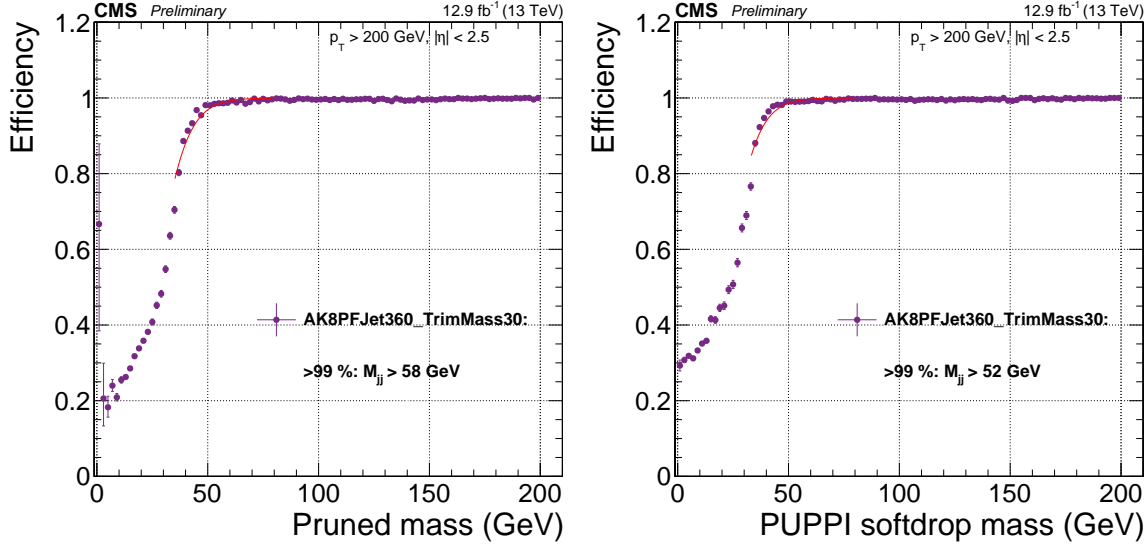


**Figure 5.30:** Efficiency for the HLT\_AK8PFJet360\_TrimMass30 trigger as a function of pruned-jet (left) and softdrop-jet (right) mass for jets with  $p_T > 600$  GeV.

event after loose preselections are applied is shown in Figure 5.31.

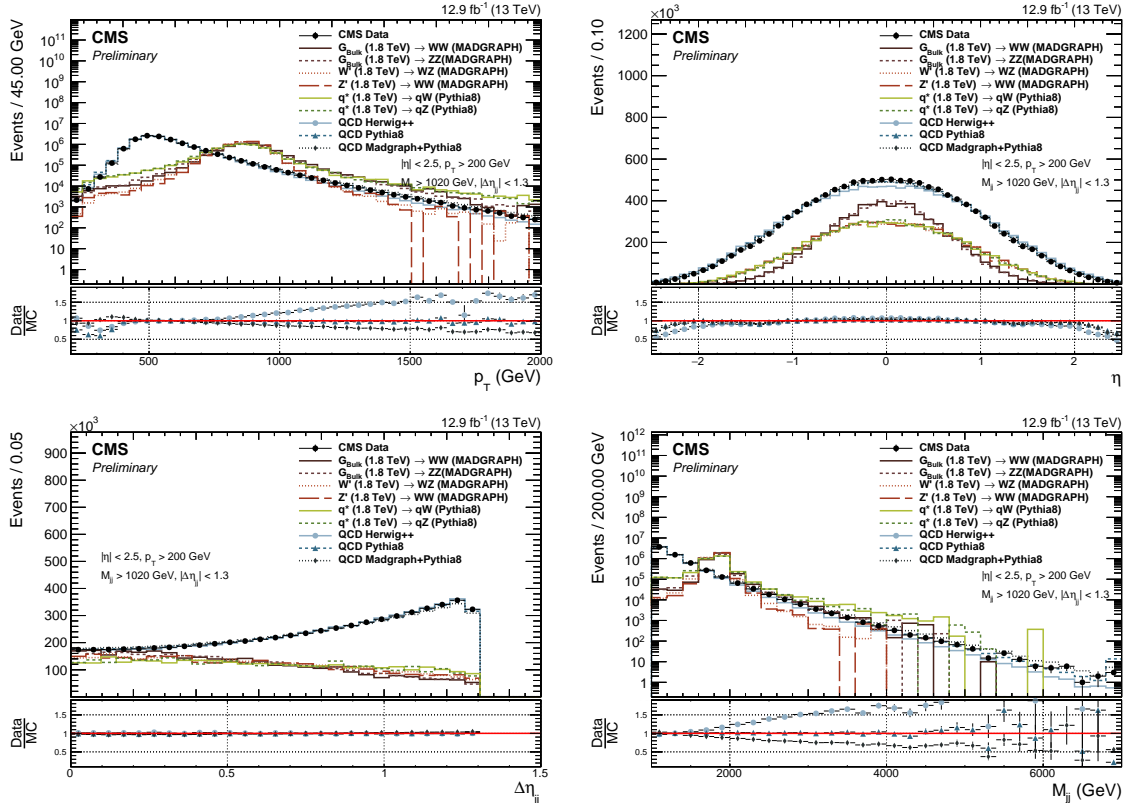


**Figure 5.31:** Jet  $p_T$  (top left),  $\eta$  (top right),  $\Delta\eta_{jj}$  and dijet invariant mass (bottom left) for the two leading jets in the event after loose preselections are applied. The signal is scaled by an arbitrary number.

A large difference in slope in the jet  $p_T$  and dijet invariant mass spectrum depending on

the QCD matrix element or shower generator is observed. Pure PYTHIA QCD MC describes the data best, while HERWIG++ and MADGRAPH5\_AMC@NLO+PYTHIA tend to under- or over-estimate the number of high  $p_T/m_{jj}$  jets, respectively. Pure PYTHIA QCD MC is therefore used for all background checks in this analysis.

### 5.0.13 Developing a new W-tagger

As mentioned in the introduction to this chapter, early studies had shown that the PUPPI pileup subtraction algorithm yielded superior resolution on large-cone jet observables like the jet mass. We therefore wanted to check whether the softdrop jet mass, and its observed sensitivity to the Underlying Event and pileup, would be improved if a better pileup subtraction algorithm was applied pre-clustering.

Two interesting observations were made. Softdrop used together with PUPPI pileup subtraction displayed a much smaller  $p_T$ -dependent shift than CHS+Softdrop, as hoped. Figure 5.32 shows the PUPPI softdrop mass for W-jets from a 1 TeV ( $p_T \sim 500$  GeV) and 4 TeV ( $p_T \sim 2$  TeV) resonance, exhibiting the desired reduced  $p_T$  dependence in jet mass scale.

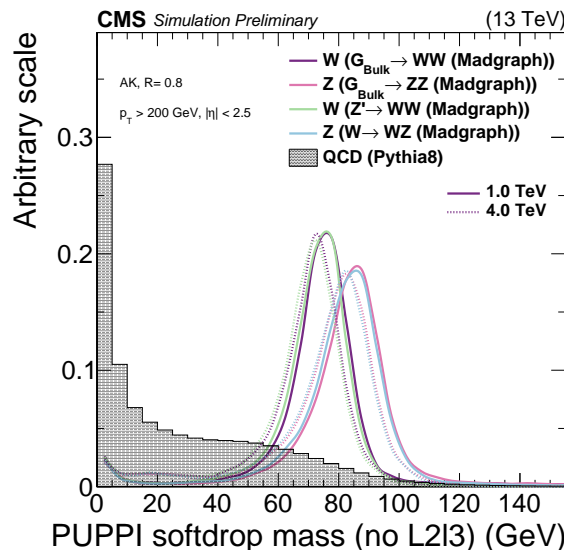


**Figure 5.32:** The PUPPI softdrop jet mass distribution with no jet energy corrections applied

However, when applying centrally provided L2 and L3 jet energy corrections (see Section 4.4.3) to the jet groomed mass, as is recommended, a strong  $p_T$  dependence is re-introduced. This effect is not present for the pruned jet mass. Figure 5.33 show the softdrop (top left) and pruned (top right) jet mass distribution with recommended L2L3 corrections applied. Here, the PUPPI+softdrop jet mass shift is significantly increased with respect to what was observed for the uncorrected mass, while CHS+pruned jet mass is stable. This points to the PUPPI jet energy corrections not being optimal for scalar jet mass variables, while they may be good for correcting jet 4-vectors. The jet energy corrections derived for CHS and PUPPI jets as a function of jet  $p_T$  is shown in the bottom plot in Figure 5.33 . A significant slope in JEC as a function of  $p_T$  is measured for PUPPI, while not present for CHS.

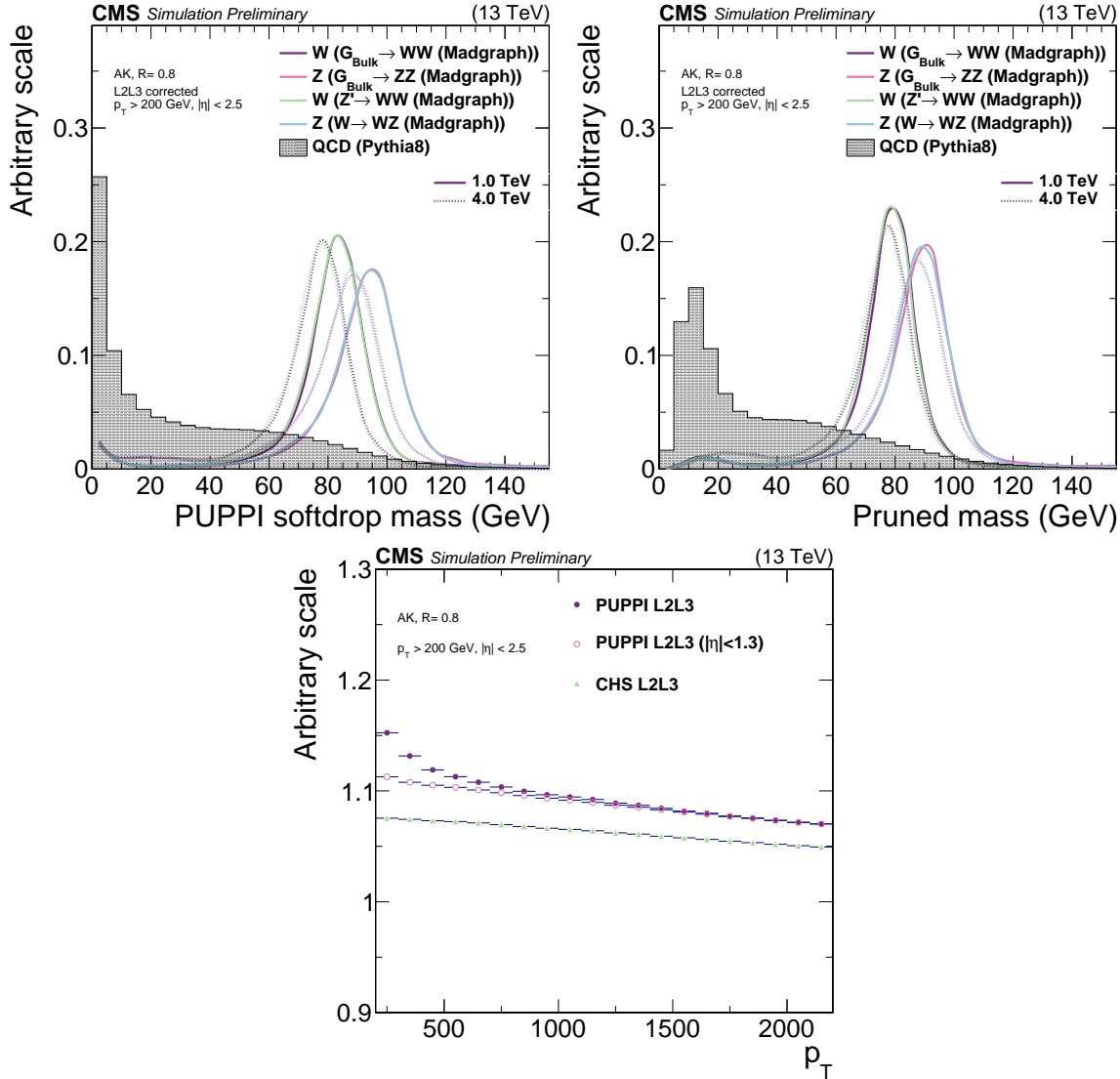


**Figure 5.33:** Top: PUPPI softdrop mass distribution (top left) and pruned jet mass distribution (top right) with L2 and L3 corrections applied. Bottom: The projection of CHS and PUPPI jet energy corrections versus jet  $p_T$ .

### 5.0.14 Dedicated PUPPI+softdrop mass corrections

In order to minimize  $p_T$  dependence in the PUPPI softdrop jet mass, all jet energy corrections to the softdrop jet mass are removed. However, this still leaves a residual  $p_T$  dependence and, in addition, the uncorrected mass does not peak at the correct W-mass of 80.4 GeV. Figure 5.34 shows the mean of a Gaussian fit to the uncorrected PUPPI softdrop mass as a function of jet  $p_T$  in two different  $\eta$  bins (smaller or greater than  $|\eta| = 1.3$ ) for W-jets coming from a Bulk Graviton signal sample. A mass shift both as a function of  $\eta$  and  $p_T$  is observed, together with an average mean significantly lower than the W-mass.

In order to use PUPPI+softdrop for W-tagging, we therefore derive dedicated jet mass corrections to compensate for two factors: A generator level  $p_T$ -dependence, as first observed in , and a reconstruction level  $p_T$ - and  $\eta$ -dependence, most likely caused by UE effects and the growing effective softdrop radius at low jet  $p_T$ . Figure 5.35 shows the mean of the generated softdrop mass (left) and the normalized difference in reconstructed and generated softdrop

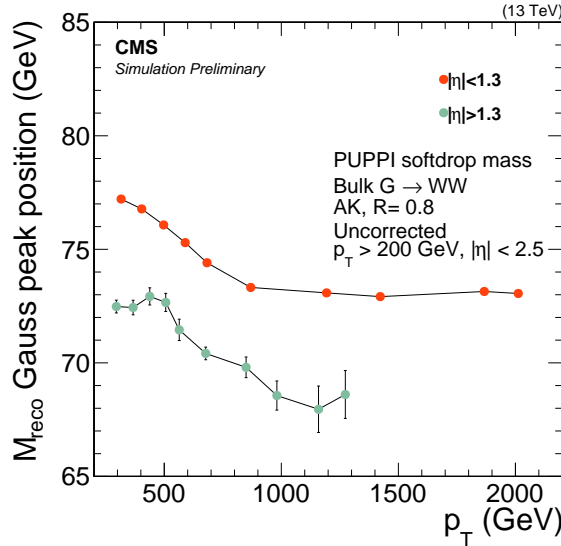


**Figure 5.34:** The mean of a Gaussian fit to the W-jet PUPPI softdrop mass peak as a function of jet  $p_T$  in two different  $\eta$  bins (smaller or greater than  $|\eta| = 1.3$ ). No corrections have been applied to the softdrop mass.

mass (right) as a function of jet  $p_T$ . The shift in generated softdrop mass at lower  $p_T$  is of the order of 2-3% while the difference between reconstructed and generated softdrop mass is a 5-10% effect.

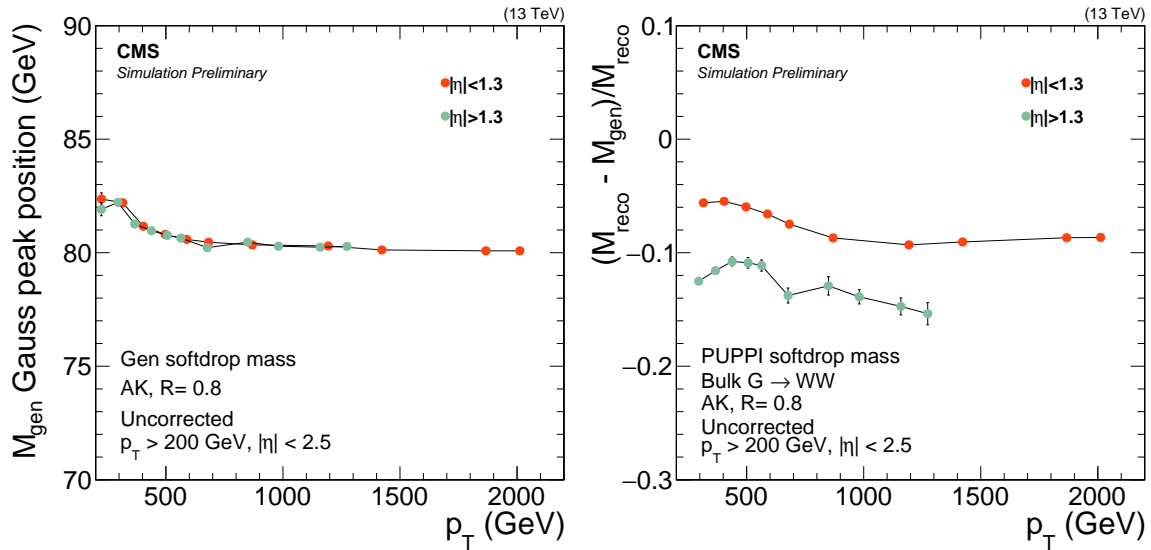


**Figure 5.35:** The mean of the fitted generator level W-jet softdrop mass distribution as a function of jet  $p_T$  (left) and the normalized difference in reconstructed and generated softdrop mass (right).

The mass shift introduced at generator level is corrected by a fit to  $M_{\text{PDG}}/M_{\text{GEN}}$  as a function of jet  $p_T$ , where  $M_{\text{PDG}} = 80.4$  GeV and  $M_{\text{GEN}}$  is the fitted mean of the generator level mass as shown in the left plot in Figure 5.35. To correct for the residual shift between generated and reconstructed softdrop mass, a fit to  $(M_{\text{RECO}} - M_{\text{GEN}})/M_{\text{RECO}}$ , where  $M_{\text{RECO}}$  is the reconstructed mass shown in the right plot in Figure 5.35 and  $M_{\text{GEN}}$  is as defined above, as a function of jet  $p_T$  in two  $\eta$  bins (smaller or greater than  $|\eta| = 1.3$ ) is performed.

Polynomial fit functions of the following forms are used

$$\begin{aligned} w(p_T) &= A + B(x^2)^{-C} && \sim \text{"gen correction"} \\ w(p_T) &= A + Bx + Cx^2 + Dx^3 + Ex^4 + Fx^5 && \sim \text{"reco correction"} \end{aligned}$$

The distribution and corresponding fits for the two weights is shown in Figure 5.36 for the "gen correction" (left) and "reco correction" (right).

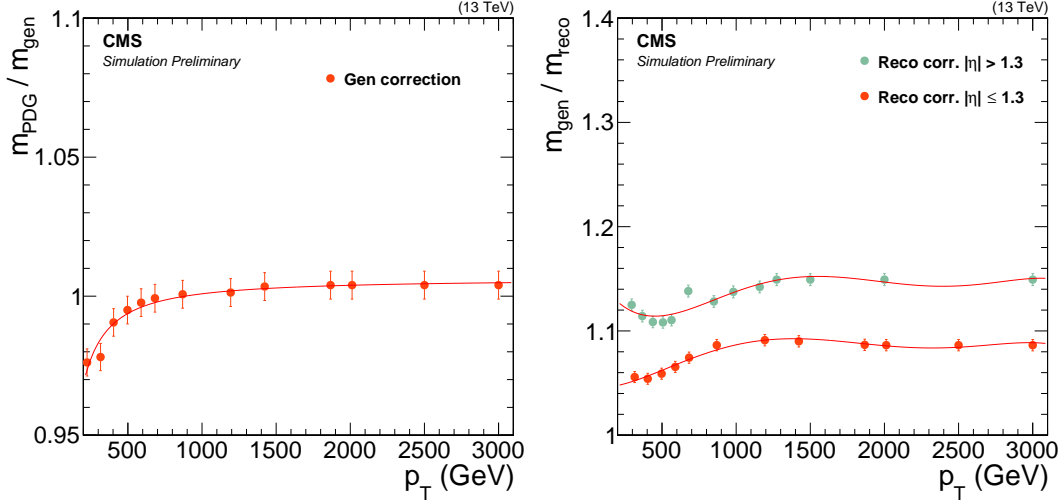


**Figure 5.36:** Fit to  $M_{\text{PDG}}/M_{\text{GEN}}$  as a function of jet  $p_T$  (left), where  $M_{\text{PDG}} = 80.4$  GeV and  $M_{\text{GEN}}$  is the fitted mean of the generator level mass and a fit to  $(M_{\text{RECO}} - M_{\text{GEN}})/M_{\text{RECO}}$  (right), where  $M_{\text{RECO}}$  is the reconstructed softdrop mass, as a function of jet  $p_T$  in two  $\eta$  bins.

The two corrections are then applied to the uncorrected PUPPI softdrop mass both in data and in MC as

$$M_{SD} = M_{SD,\text{uncorr}} \times w_{\text{GEN}} \times w_{\text{RECO}} \quad (5.7)$$

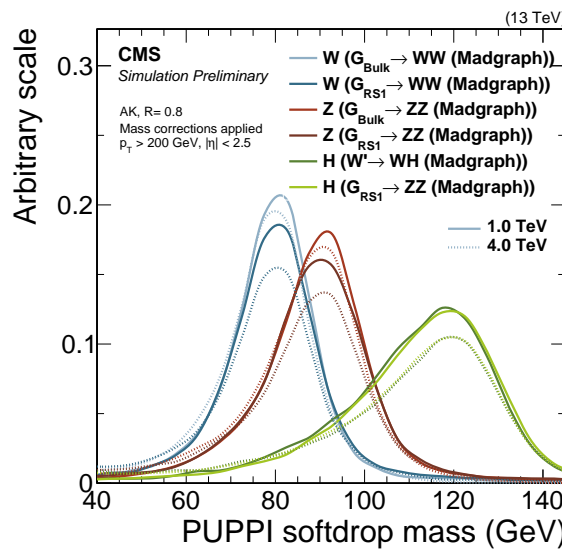
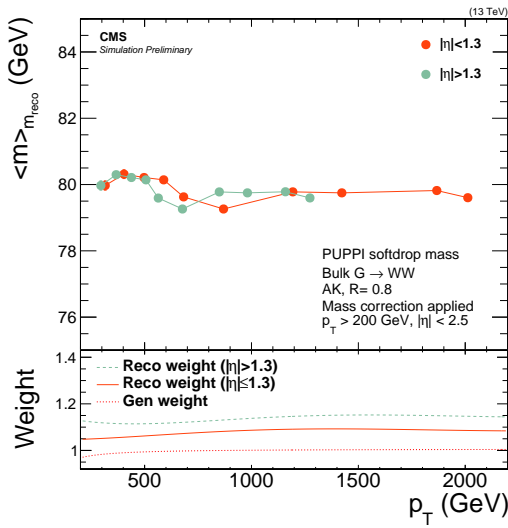
where  $w_{\text{GEN}}$  and  $w_{\text{RECO}}$  correspond to the gen and reco corrections respectively and  $M_{SD,\text{uncorr}}$  is the uncorrected PUPPI softdrop mass.

Finally, a closure test is performed in order to check that the corrected PUPPI+softdrop W-jet mass peaks at 80.4 GeV and is stable with  $p_T$  and  $\eta$ . The fitted mean of the corrected PUPPI softdrop mass peak as a function of jet  $p_T$  in two different  $\eta$  bins is shown in Figure 5.37. Good closure is observed, with the corrected mass peaking around 80 GeV independent of the jet  $p_T$  and  $\eta$ . The PUPPI softdrop jet mass peak for W/Z-jets from different signal samples after jet mass corrections have been applied is shown in Figure 5.38, for resonances with a mass of 1 and 4 TeV. The corrections applied to Z-jets yield a mass stable with  $p_T$ , peaking around the Z mass.

### 5.0.15 W-tagging performance

The new PUPPI+softdrop based W/Z-tagger uses a mass window of  $65 \text{ GeV} < m_{SD} < 105 \text{ GeV}$  in combination with a cut of PUPPI  $\tau_{21} < 0.4$ . We compare its performance to that of the CHS+pruning based tagger used in Search I as well as to that of a "DDT-transformed"  $\tau_{21}$  based tagger [?]. The  $\tau_{21}^{DDT}$  variable is a linear transformation of  $\tau_{21}$  given as

$$\tau_{21}^{DDT} = \tau_{21} + M \times \log \left( \frac{m^2}{p_T \times 1 \text{ GeV}} \right) \quad (5.8)$$



where  $M = -0.063$  is obtained from a fit of  $\tau_{21}$  against the variable  $\rho' = \log(m^2/p_T/\mu)$ , where  $\mu = 1\text{ GeV}$ . The purpose of this is to decorrelate  $\tau_{21}$  from the softdrop mass and  $p_T$ , yielding a mass and dijet invariant mass spectrum minimally sculpted by a cut on the  $\tau_{21}^{DDT}$  tagging variable. This is tagger that will be further explored and explained in detail in the context of Search III, Section 5.1.4.

The background rejection efficiency for QCD light flavor jets as a function of W-jet signal efficiency is shown in Figure 5.39. The efficiency is measured requiring a fixed jet mass window of  $65\text{--}105\text{ GeV}$ , while scanning the cut on  $\tau_2/\tau_1$ .

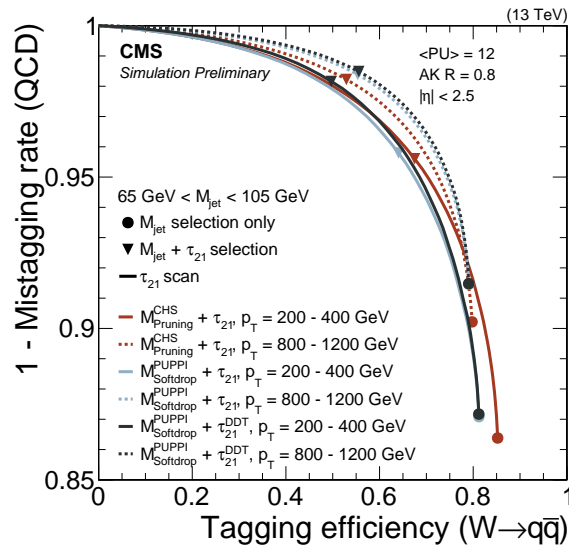


**Figure 5.39:** The background rejection efficiency for QCD light flavor jets as a function of W-jet signal efficiency. A cut on CHS pruned or PUPPI softdrop jet mass of  $65 < m_{\text{jet}} < 105\text{ GeV}$  is applied while scanning the cut on  $\tau_{21}$ . The cuts corresponding to  $\tau_2/\tau_1 < 0.45$  for CHS+pruning, PUPPI  $\tau_2/\tau_1 < 0.4$  for PUPPI+softdrop or  $\tau_{21}^{DDT} < 0.52$  are indicated with triangles, while the solid circles represent the efficiency and mistag rate for a mass cut only.

The general performance of each tagger is very similar, with the PUPPI+softdrop based taggers displaying a slightly higher signal efficiency for a given mistag rate at high  $p_T$  and CHS+pruning slightly better at low  $p_T$ . Two better understand the difference between each tagger, we look at the tagging performance as a function of jet  $p_T$  as well as pileup, shown in Figure 5.40 and 5.41.

Starting with the tagger  $p_T$ -dependence in Figure 5.40, we observe that she signal efficiency of a PUPPI+softdrop of CHS+pruned jet mass cut is flat as a function of  $p_T$ , at around 80%. The QCD mistagging rate drops for both groomers, with a 1-3% lower mistag rate using PUPPI+softdrop than CHS+pruning.

Once applying a  $\tau_{21}$ cut, the signal efficiency as well as the mistag rate for the PUPPI  $\tau_{21}$  and CHS  $\tau_{21}$  taggers drops as a function of  $p_T$ , with an average signal efficiency of around 50% for a  $\sim 2\%$  mistag rate. An interesting behavior is observed for the  $\tau_{21}^{DDT}$  tagger: While the mistag rate is flat as a function of  $p_T$ , as is the purpose of decorrelated taggers, the signal efficiency improves as the  $p_T$  increases, outperforming the other taggers above 1 TeV.

Turning to the tagger pileup dependence, shown in Figure 5.41, the expected benefit from using the PUPPI algorithm is observed: The tagging efficiency for the CHS+pruning (red solid circles) based tagger falls off steeply versus the number of primary vertices in the event, while the PUPPI+softdrop based taggers (light and dark blue solid circles) are insensitive to pileup.

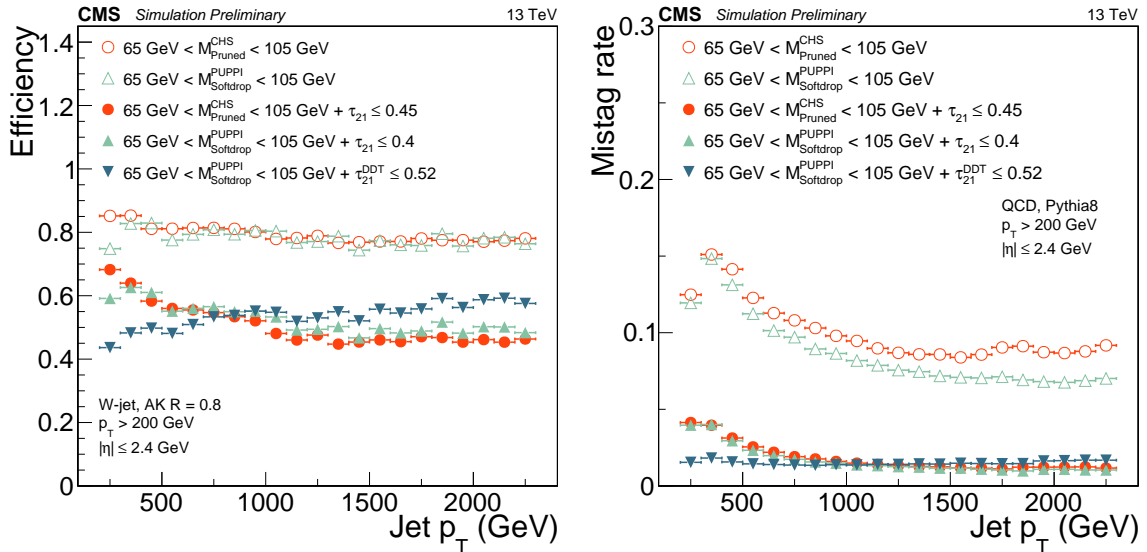


**Figure 5.40:** W-jet efficiency (left) and QCD light jet mistag rate (right) for a PUPPI+softdrop or CHS+pruned jet mass selection only (hollow circles) and the combined  $m_{\text{jet}} + (\text{PUPPI}) \tau_2/\tau_1$  (DDT) selection (solid circles) as a function of jet  $p_T$ .

### 5.0.16 Validation in data

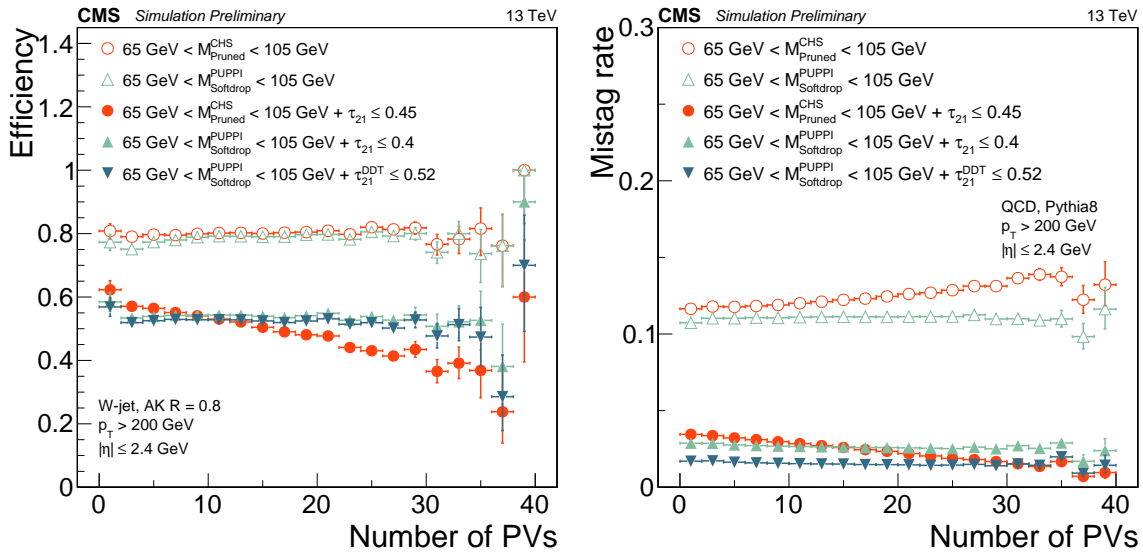
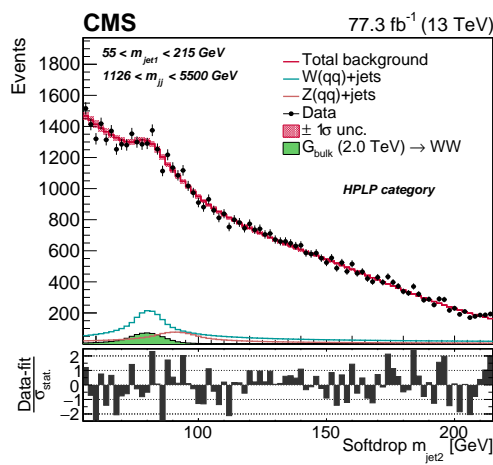


**Figure 5.41:** W-jet efficiency (left) and QCD light jet mistag rate (right) for a PUPPI+softdrop or CHS+pruned jet mass selection only (hollow circles) and the combined  $m_{\text{jet}} + (\text{PUPPI}) \tau_2/\tau_1$  (DDT) selection (solid circles) as a function of jet pileup.

## 5.1 Search III: A novel framework for multi-dimensional searches

After two successful analyses of 13 TeV data, no excess had been observed in the all-hadronic VV channels. The available phase space for New Physics to hide out was shrinking and we saw two ways forward: Either look for deviations from the Standard Model through precision measurements that would allow searching for resonances currently out of LHC reach, or deplete the number of places New Physics could be hiding as efficiently and completely as possible. With a solid background in searches with boosted final states, we decided for the latter. Our idea was the following: What if the small excesses observed in VV final states were due to us catching the tail of another type of boson with a mass slightly different from that of a W or a Z boson? And what if we were seeing cascade decays, where the jets in questions were actually four-prong like rather than two?.....TODO

Completing the Run 2 VV search program is Search III: A novel framework for multi-dimensional searches.



- 5.1.1 Small bumps and tribosons
- 5.1.2 Analysis strategy
- 5.1.3 Event selection
- 5.1.4 A mass and  $p_T$  decorrelated tagger
- 5.1.5 The multidimensional fit

---

---

## CHAPTER 6

---

# LoLa: A novel Machine Learning W-tagger for future analyses

- 6.1 Machine Learning: The future of high-performance, low-latency taggers
- 6.2 LoLa: A Lorentz Invariance Based Deep Neural Network for W-tagging
  - 6.2.1 Inputs
  - 6.2.2 The Combination Layer
  - 6.2.3 The Lorentz Layer
- 6.3 Decorrelating from mass and  $p_T$
- 6.4 Performance

---

## CHAPTER 7

---

### Summary

## APPENDIX A

# Search I: Limits per mass category

The asymptotic limits obtained with  $2.6 \text{ fb}^{-1}$  of 13 TeV CMS data per mass and purity category. The largest significance is found at 2.8-3 TeV in the ZZ high-purity category, where one event at 3 TeV yields a local significance of  $2.8\sigma$ . A 3 parameter fit is the default background fit function for this category, however, a 2 parameter fit could also be used to describe these data. In Figure ?? we compare the limits and p-values obtained using a 2 parameter and a 3 parameter fit to describe the background in this category. The significance at 3 TeV is reduced from  $2.8$  to  $1.5\sigma$  with a 2 parameter fit, reflecting the fact that the fit is poorly constrained in the high mass tail due to low statistics. The fit to data using both a 2 and 3 parameter fit is the ZZHP category is shown in Figure 5.25.

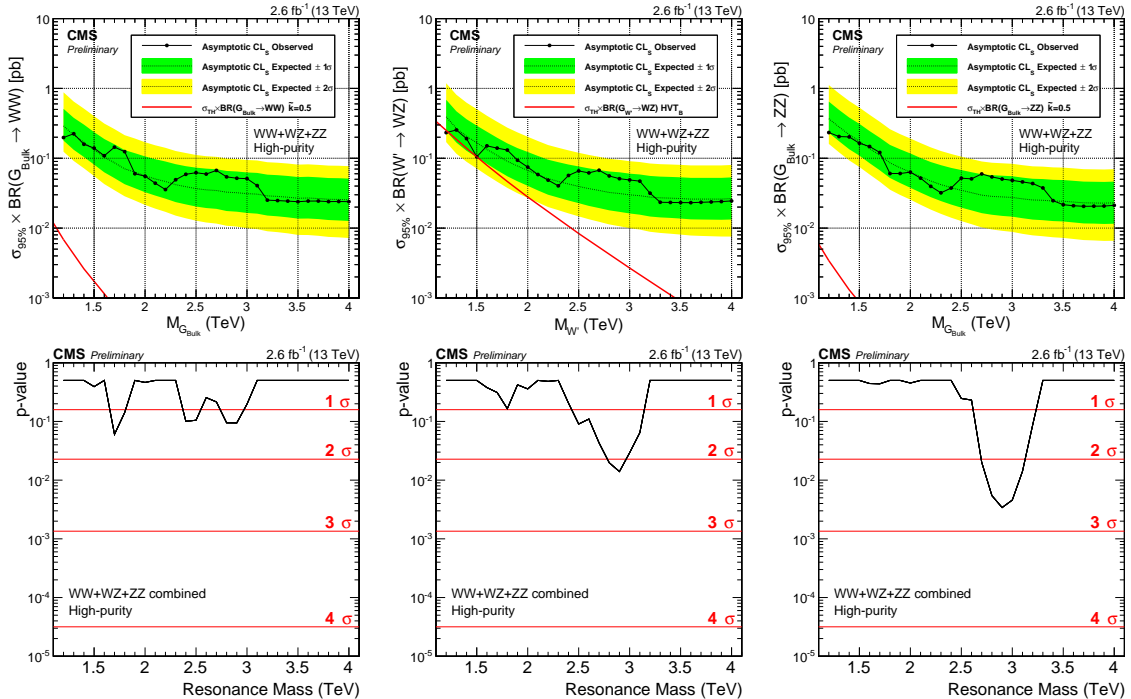


**Figure A.1:** Expected/observed limits and corresponding p-values obtained in the high purity category using  $2.6 \text{ fb}^{-1}$  of CMS data. Here for a Bulk  $G \rightarrow WW$  (left),  $W' \rightarrow WZ$  (middle) and  $G \rightarrow ZZ$  (right) signal.

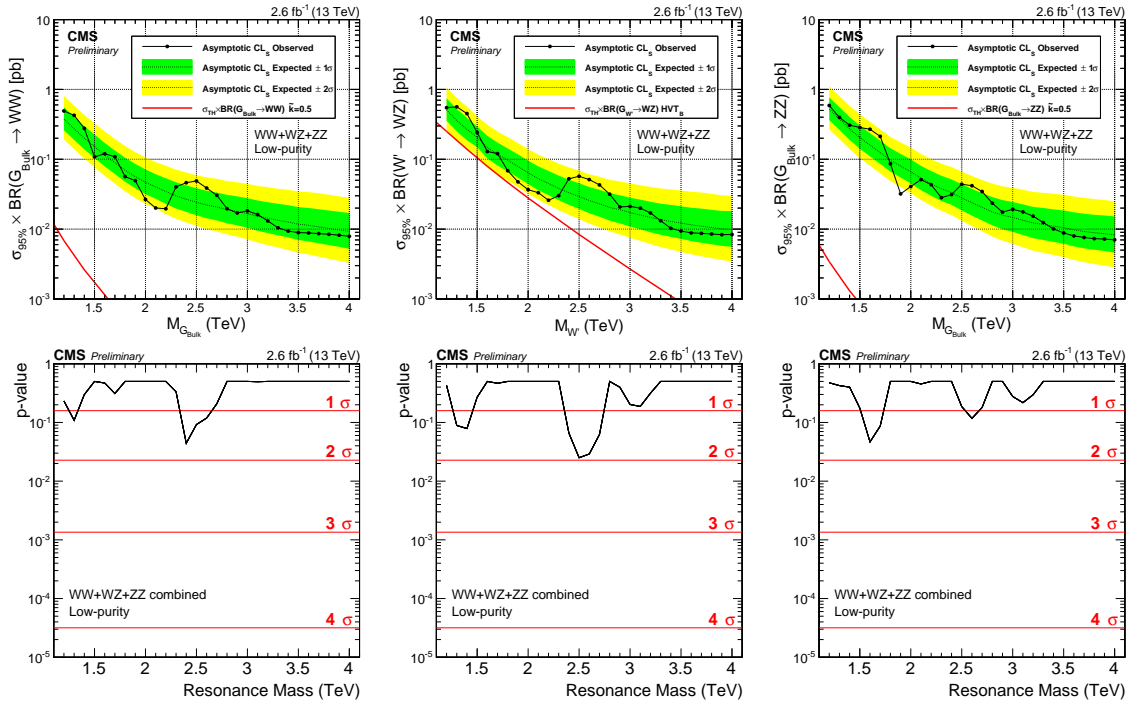


**Figure A.2:** Expected/observed limits and corresponding p-values obtained in the low purity category using  $2.6 \text{ fb}^{-1}$  of CMS data. Here for a Bulk  $G \rightarrow WW$  (left),  $W' \rightarrow WZ$  (middle) and  $G \rightarrow ZZ$  (right) signal.

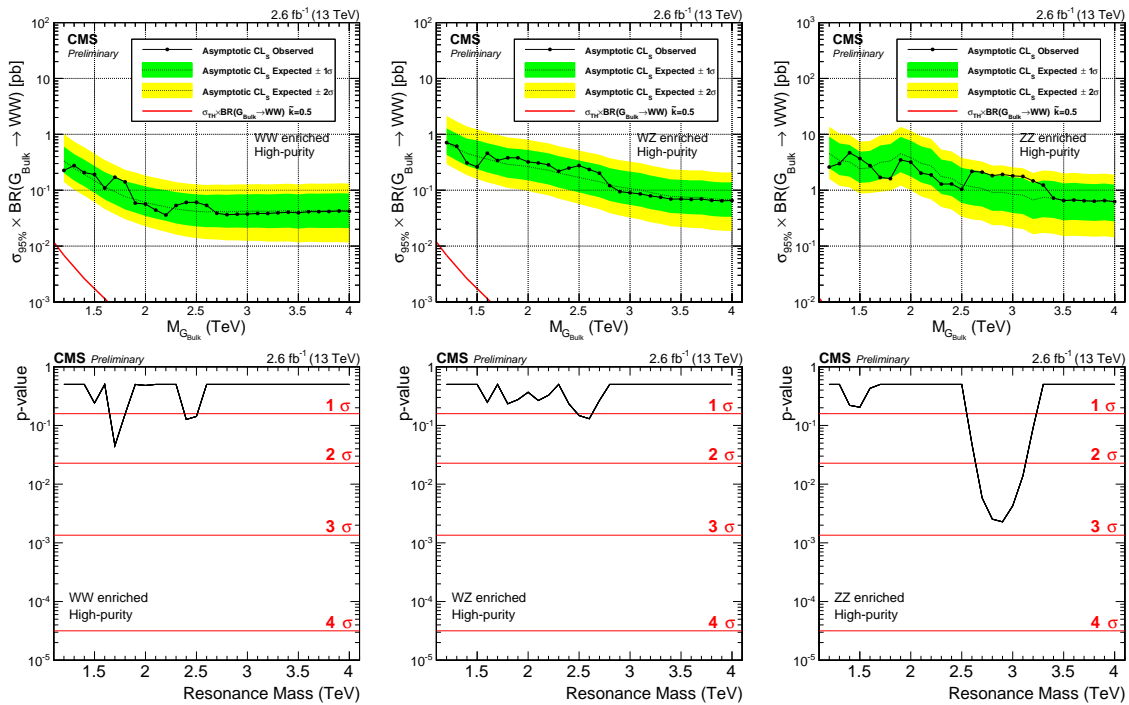


**Figure A.3:** Expected/observed limits and corresponding p-values obtained for the different mass categories using  $2.6 \text{ fb}^{-1}$  of CMS data. Here for a Bulk  $G \rightarrow WW$  signal in the HP category

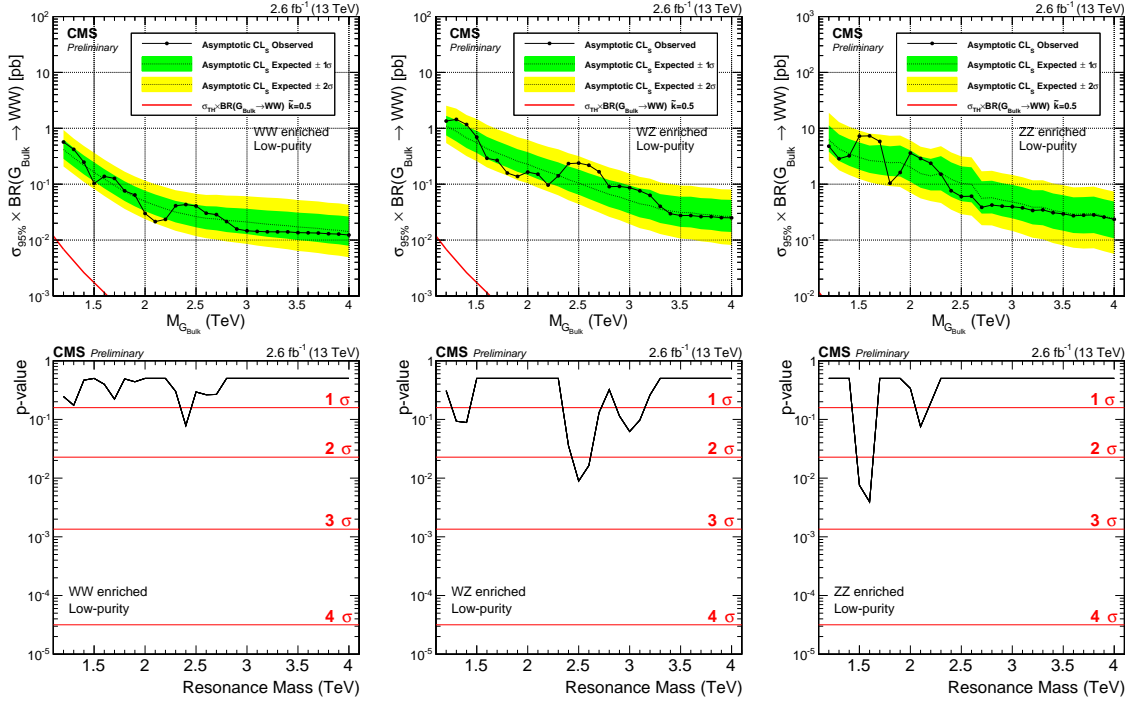


**Figure A.4:** Expected/observed limits and corresponding p-values obtained in the different mass categories using  $2.6 \text{ fb}^{-1}$  of CMS data. Here for a Bulk  $G \rightarrow WW$  signal in the LP category.

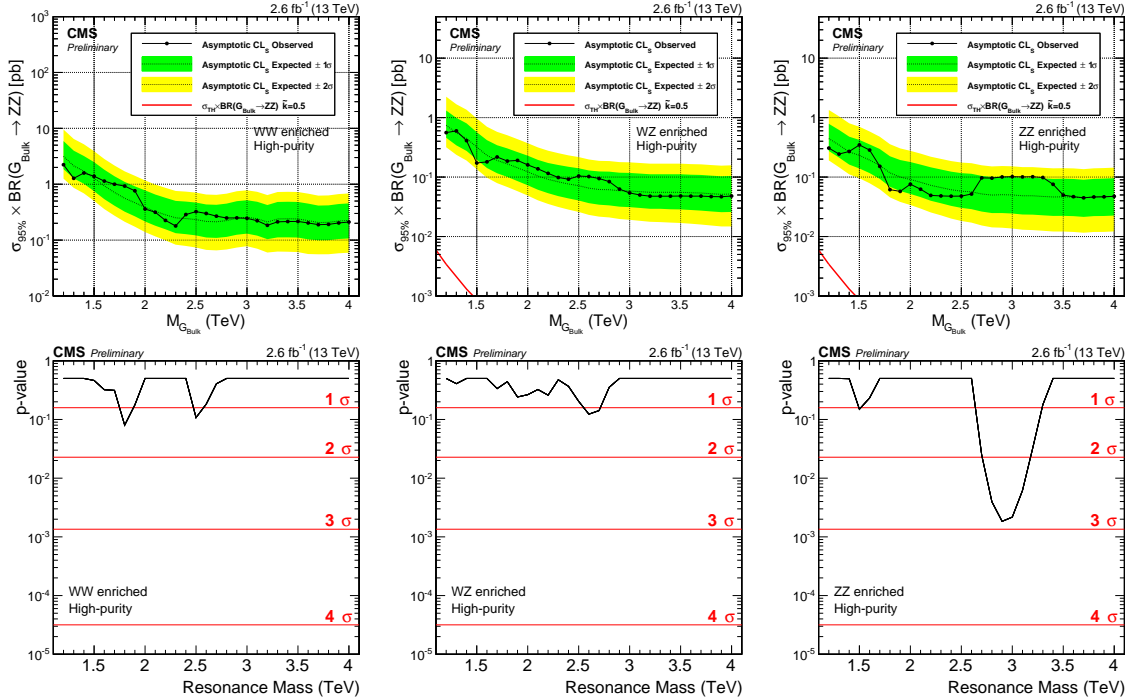


**Figure A.5:** Expected/observed limits and corresponding p-values obtained in the different mass categories. Here for a  $G \rightarrow ZZ$  signal in the HP category.

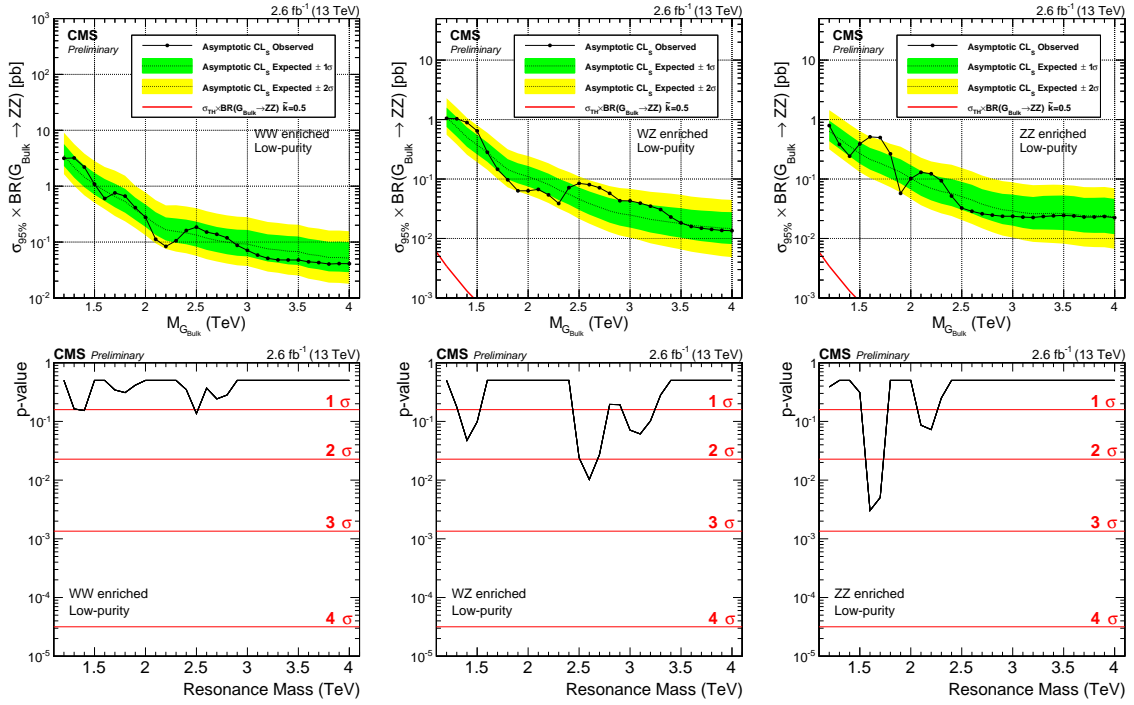


**Figure A.6:** Expected/observed limits and corresponding p-values obtained in the different mass categories. Here for a  $G \rightarrow ZZ$  signal in the LP category.

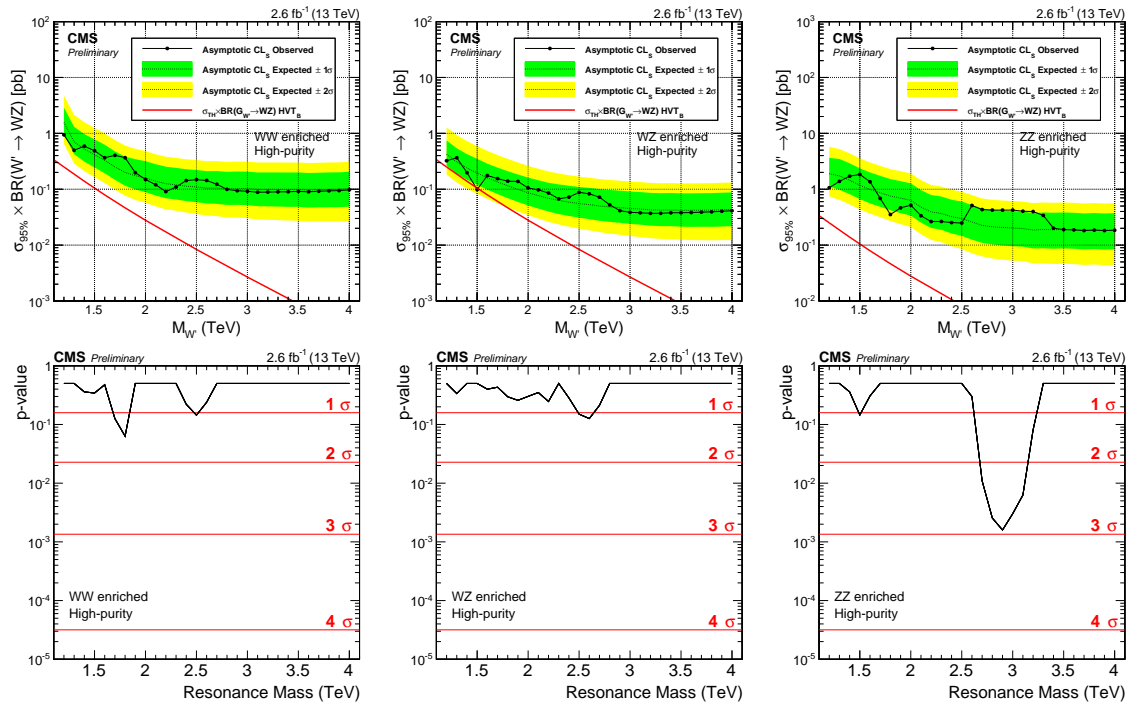


**Figure A.7:** Expected/observed limits and corresponding p-values obtained in the different mass categories. Here for a  $W' \rightarrow WZ$  signal in the high-purity category.

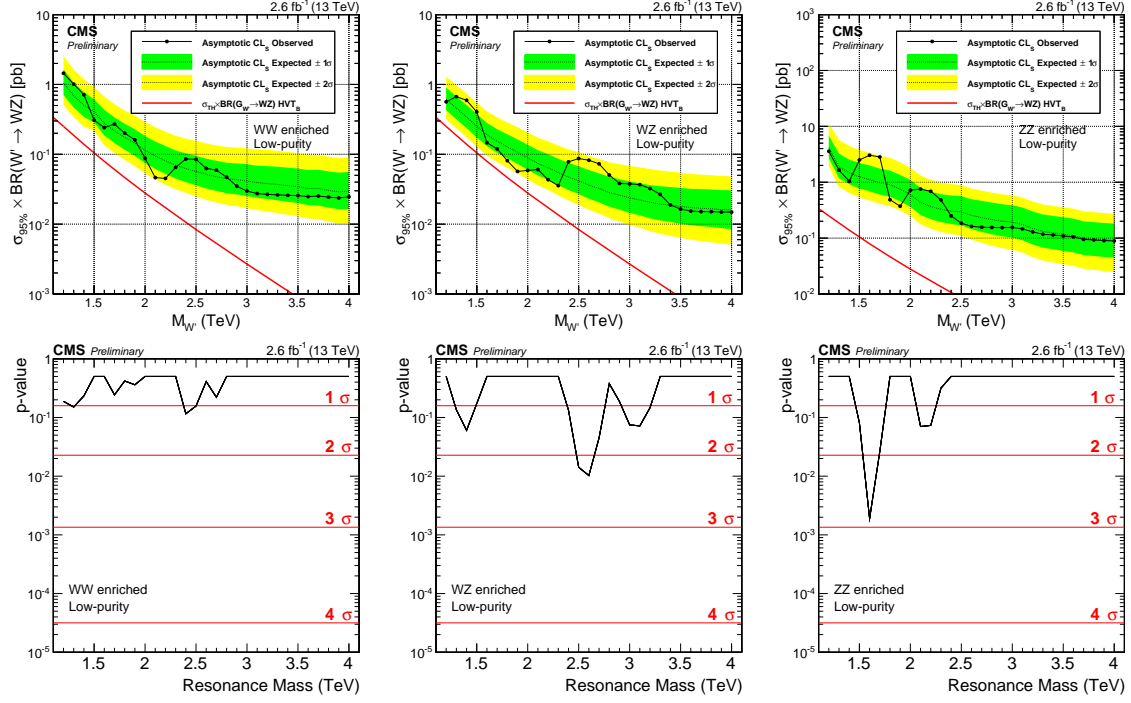


**Figure A.8:** Expected/observed limits and corresponding p-values obtained in the different mass categories. Here for a  $W' \rightarrow WZ$  signal in the low purity category.

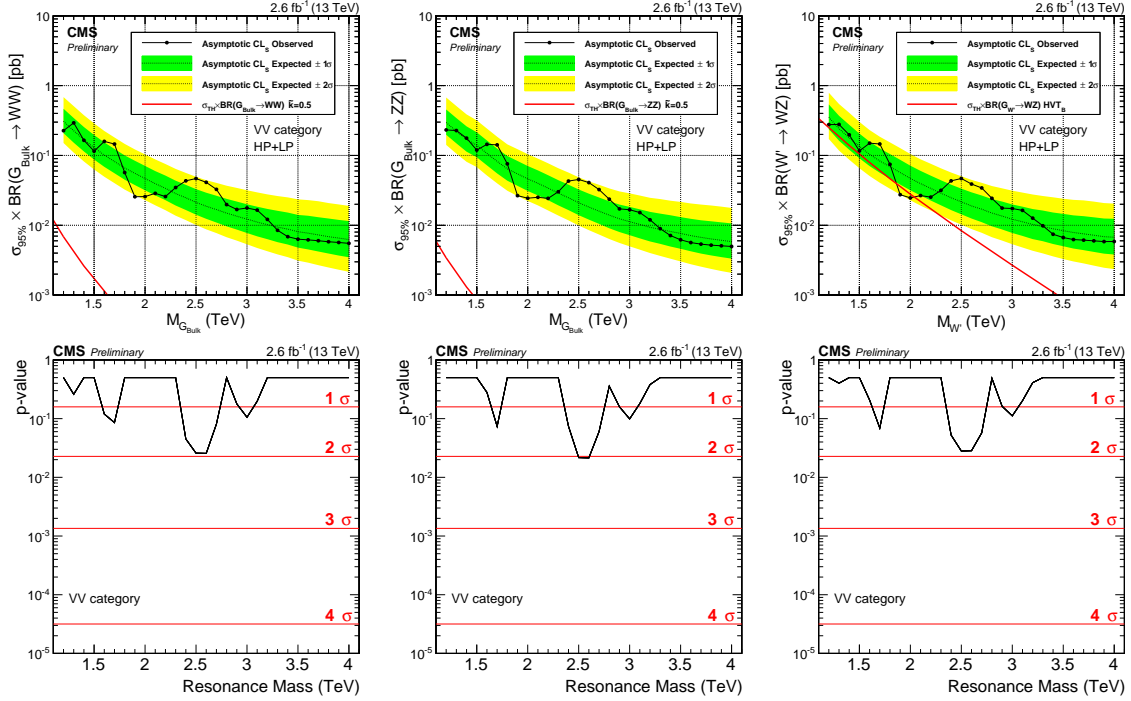


**Figure A.9:** Expected/observed limits and corresponding p-values obtained without splitting into mass categories. This analysis is performed as a cross check analysis and directly compares with the method used in the corresponding Run 1 analysis [?]. Here for a Bulk  $G \rightarrow WW$  (left),  $G \rightarrow ZZ$  (middle) and  $W' \rightarrow WZ$  signal (right).

---

## Bibliography

- [1] CERN, “Accelerators and Schedules”, 2018 (accessed November 12, 2018),  
<https://beams.web.cern.ch/content/accelerators-schedules>.
- [2] CMS, “CMS Detector Design”, 2018 (accessed November 21, 2018),  
<https://cms.cern/news/cms-detector-design>.
- [3] T. Lenzi, “Development and Study of Different Muon Track Reconstruction Algorithms for the Level-1 Trigger for the CMS Muon Upgrade with GEM Detectors”, Master’s thesis, U. Brussels (main), 2013.
- [4] A. Dominguez et al., “CMS Technical Design Report for the Pixel Detector Upgrade”, Technical Report CERN-LHCC-2012-016. CMS-TDR-11, CERN, Sep, 2012.
- [5] CMS Collaboration, “The CMS Experiment at the CERN LHC”, *JINST* **3** (2008) S08004, doi:10.1088/1748-0221/3/08/S08004.
- [6] P. Adzic et al., “Energy resolution of the barrel of the CMS electromagnetic calorimeter”, *JINST* **2** (2007) P04004, doi:10.1088/1748-0221/2/04/P04004.
- [7] C. Biino, “The CMS Electromagnetic Calorimeter: overview, lessons learned during Run 1 and future projections”, *Journal of Physics: Conference Series* **587** (2015), no. 1, 012001.
- [8] L. V. . EP, “Assembly of the 7th wedge. Assemblage du 7eme module”, (Aug, 2000). CMS Collection.
- [9] S. Sharma, “Understanding the performance of CMS calorimeter”, *Pramana* **69** (Dec, 2007) 1069–1074, doi:10.1007/s12043-007-0229-8.
- [10] on behalf of the CMS Collaboration Collaboration, “CMS reconstruction improvement for the muon tracking by the RPC chambers”, *PoS RPC2012* (Sep, 2012) 045. 9 p. Presented by Minsuk Kim at the XI workshop on Resistive Plate Chambers and Related Detectors - RPC2012, INFN Laboratori Nazionali di Frascati Italy, February 5-10, 2012.
- [11] CMS, “CMS Luminosity - public results”, 2018 (accessed December 11, 2018),  
<https://twiki.cern.ch/twiki/bin/view/CMSPublic/LumiPublicResults>.
- [12] P. Billoir, “Progressive track recognition with a Kalman-like fitting procedure”, *Computer Physics Communications* **57** (1989), no. 1, 390 – 394, doi:[https://doi.org/10.1016/0010-4655\(89\)90249-X](https://doi.org/10.1016/0010-4655(89)90249-X).
- [13] A. S. et. Al., “Particle-flow reconstruction and global event description with the CMS detector”, *Journal of Instrumentation* **12** (2017), no. 10, P10003.

- [14] W. Adam, R. Frühwirth, A. Strandlie, and T. Todorov, “Reconstruction of electrons with the Gaussian-sum filter in the CMS tracker at the LHC”, *Journal of Physics G: Nuclear and Particle Physics* **31** (2005), no. 9, N9.
- [15] T. C. collaboration, “Performance of CMS muon reconstruction in pp collision events at  $s = 7$  TeV”, *Journal of Instrumentation* **7** (2012), no. 10, P10002.
- [16] D. Bertolini, P. Harris, M. Low, and N. Tran, “Pileup per particle identification”, *Journal of High Energy Physics* **2014** (2014), no. 10, doi:10.1007/JHEP10(2014)059.
- [17] Y. L. Dokshitzer, G. D. Leder, S. Moretti, and B. R. Webber, “Better jet clustering algorithms”, *JHEP* **08** (1997) 001, doi:10.1088/1126-6708/1997/08/001, arXiv:hep-ph/9707323.
- [18] S. D. Ellis and D. E. Soper, “Successive combination jet algorithm for hadron collisions”, *Phys. Rev.* **D48** (1993) 3160–3166, doi:10.1103/PhysRevD.48.3160, arXiv:hep-ph/9305266.
- [19] M. Cacciari, G. P. Salam, and G. Soyez, “The anti- $k_t$  jet clustering algorithm”, *JHEP* **04** (2008) 063, doi:10.1088/1126-6708/2008/04/063, arXiv:0802.1189.
- [20] D. Krohn, J. Thaler, and L.-T. Wang, “Jet Trimming”, *JHEP* **02** (2010) 084, doi:10.1007/JHEP02(2010)084, arXiv:0912.1342.
- [21] CMS Collaboration Collaboration, “Pileup Removal Algorithms”, Technical Report CMS-PAS-JME-14-001, CERN, Geneva, 2014.
- [22] M. Dasgupta, A. Fregoso, S. Marzani, and G. P. Salam, “Towards an understanding of jet substructure”, *JHEP* **09** (2013) 029, doi:10.1007/JHEP09(2013)029, arXiv:1307.0007.
- [23] J. M. Butterworth, A. R. Davison, M. Rubin, and G. P. Salam, “Jet substructure as a new Higgs search channel at the LHC”, *Phys. Rev. Lett.* **100** (2008) 242001, doi:10.1103/PhysRevLett.100.242001, arXiv:0802.2470.
- [24] A. J. Larkoski, S. Marzani, G. Soyez, and J. Thaler, “Soft Drop”, *JHEP* **05** (2014) 146, doi:10.1007/JHEP05(2014)146, arXiv:1402.2657.
- [25] J. Thaler and K. Van Tilburg, “Identifying Boosted Objects with N-subjettiness”, *JHEP* **03** (2011) 015, doi:10.1007/JHEP03(2011)015, arXiv:1011.2268.
- [26] J. Thaler and K. Van Tilburg, “Maximizing boosted top identification by minimizing N-subjettiness”, *Journal of High Energy Physics* **2012** (Feb, 2012) 93, doi:10.1007/JHEP02(2012)093.
- [27] S. Bolognesi et al., “Spin and parity of a single-produced resonance at the LHC”, *Phys. Rev. D* **86** (Nov, 2012) 095031, doi:10.1103/PhysRevD.86.095031.
- [28] CMS Collaboration, “Identification techniques for highly boosted W bosons that decay into hadrons”, *JHEP* **12** (2014) 017, doi:10.1007/JHEP12(2014)017, arXiv:1410.4227.
- [29] M. Bahr et al., “Herwig++ Physics and Manual”, *Eur. Phys. J. C* **58** (2008) 639–707, doi:10.1140/epjc/s10052-008-0798-9, arXiv:0803.0883.

- [30] T. Sjöstrand et al., “An Introduction to PYTHIA 8.2”, *Comput. Phys. Commun.* **191** (2015) 159–177, doi:10.1016/j.cpc.2015.01.024, arXiv:1410.3012.
- [31] The ATLAS collaboration, “Search for high-mass diboson resonances with boson-tagged jets in proton-proton collisions at  $s=8$  TeV with the ATLAS detector”, *Journal of High Energy Physics* **2015** (Dec, 2015) 1–39, doi:10.1007/JHEP12(2015)055.
- [32] S. Frixione and B. R. Webber, “Matching NLO QCD computations and parton shower simulations”, *JHEP* **06** (2002) 029, doi:10.1088/1126-6708/2002/06/029, arXiv:hep-ph/0204244.
- [33] S. Frixione, P. Nason, and B. R. Webber, “Matching NLO QCD and parton showers in heavy flavor production”, *JHEP* **08** (2003) 007, doi:10.1088/1126-6708/2003/08/007, arXiv:hep-ph/0305252.
- [34] S. Frixione, P. Nason, and C. Oleari, “Matching NLO QCD computations with Parton Shower simulations: the POWHEG method”, *JHEP* **11** (2007) 070, doi:10.1088/1126-6708/2007/11/070, arXiv:0709.2092.
- [35] S. A. et. al., “Geant4—a simulation toolkit”, *Nuclear Instruments and Methods in Physics Research Section A: Accelerators, Spectrometers, Detectors and Associated Equipment* **506** (2003), no. 3, 250 – 303, doi:[https://doi.org/10.1016/S0168-9002\(03\)01368-8](https://doi.org/10.1016/S0168-9002(03)01368-8).
- [36] CMS Collaboration, “Event generator tunes obtained from underlying event and multiparton scattering measurements”, *Eur. Phys. J. C* **76** (2016) 155, doi:10.1140/epjc/s10052-016-3988-x, arXiv:1512.00815.
- [37] CMS Collaboration Collaboration, “Search for massive resonances in dijet systems containing jets tagged as W or Z boson decays in pp collisions at  $\sqrt{s}=8$  TeV”, *JHEP* **08** (May, 2014) 173. 37 p. Comments: Replaced with published version. Added journal reference and DOI.
- [38] F. Dias et al., “Combination of Run-1 Exotic Searches in Diboson Final States at the LHC”, *JHEP* **04** (2016) 155, doi:10.1007/JHEP04(2016)155, arXiv:1512.03371.
- [39] J. Alwall et al., “The automated computation of tree-level and next-to-leading order differential cross sections, and their matching to parton shower simulations”, *JHEP* **07** (2014) 079, doi:10.1007/JHEP07(2014)079, arXiv:1405.0301.
- [40] T. Sjöstrand, S. Mrenna, and P. Z. Skands, “A brief introduction to PYTHIA 8.1”, *Comput. Phys. Commun.* **178** (2008) 852, doi:10.1016/j.cpc.2008.01.036, arXiv:0710.3820.
- [41] J. POG, “Jet Identification: Recommendations for 13TeV data analysis”, 2018 (accessed December 18, 2018), <https://twiki.cern.ch/twiki/bin/viewauth/CMS/JetID>.
- [42] CMS Collaboration, “Determination of Jet Energy Calibration and Transverse Momentum Resolution in CMS”, *JINST* **6** (2011) P11002, doi:10.1088/1748-0221/6/11/P11002, arXiv:1107.4277.
- [43] G. Punzi, “Sensitivity of searches for new signals and its optimization”, *eConf C030908* (2003) MODT002, arXiv:physics/0308063. [,79(2003)].

- [44] CMS Collaboration, “Search for heavy resonances in the W/Z-tagged dijet mass spectrum in pp collisions at 7 TeV”, *Phys. Lett.* **B723** (2013) 280–301, doi:10.1016/j.physletb.2013.05.040, arXiv:1212.1910.
- [45] CMS Collaboration Collaboration, “Search for Narrow Resonances using the Dijet Mass Spectrum with 19.6fb-1 of pp Collisions at  $\text{sqrt}s=8$  TeV”, Technical Report CMS-PAS-EXO-12-059, CERN, Geneva, 2013.
- [46] D. J. Hand, “Statistical Concepts: A Second Course, Fourth Edition by Richard G. Lomax, Debbie L. Hahs-Vaughn”, *International Statistical Review* **80** (2012), no. 3, 491–491.
- [47] M. Dasgupta, A. Powling, and A. Siodmok, “On jet substructure methods for signal jets”, *JHEP* **08** (2015) 079, doi:10.1007/JHEP08(2015)079, arXiv:1503.01088.
- [48] U. Baur, I. Hinchliffe, and D. Zeppenfeld, “Excited quark production at hadron colliders”, *Int. J. Mod. Phys. A* **2** (1987) 1285, doi:10.1142/S0217751X87000661.
- [49] U. Baur, M. Spira, and P. M. Zerwas, “Excited-quark and -lepton production at hadron colliders”, *Phys. Rev. D* **42** (1990) 815, doi:10.1103/PhysRevD.42.815.
- [50] CMS Collaboration Collaboration, “Search for massive resonances decaying into WW, WZ, ZZ, qW and qZ in the dijet final state at  $\sqrt{s} = 13$  TeV using 2016 data”, Technical Report CMS-PAS-B2G-16-021, CERN, Geneva, 2016.
- [51] CMS Collaboration Collaboration, “Search for massive resonances decaying into WW, WZ, ZZ, qW, and qZ with dijet final states at  $\sqrt{s} = 13$  TeV”, *Phys. Rev. D* **97** (Apr, 2018) 072006, doi:10.1103/PhysRevD.97.072006.
- [52] CMS Collaboration Collaboration, “Jet algorithms performance in 13 TeV data”, Technical Report CMS-PAS-JME-16-003, CERN, Geneva, 2017.
- [53] J. Alwall et al., “Comparative study of various algorithms for the merging of parton showers and matrix elements in hadronic collisions”, *Eur. Phys. J.* **C53** (2008) 473–500, doi:10.1140/epjc/s10052-007-0490-5, arXiv:0706.2569.